Developing a QA Procedure for Gated VMAT SABR Treatments Using 10 MV Beam in Flattening-Filter Free Mode

by

Shadi Chitsazzadeh
B.Sc., Shahid Beheshti University, 2005
M.Sc., University of Western Ontario, 2009
Ph.D., University of Victoria, 2014

A Thesis Submitted in Partial Fulfillment of the
Requirements for the Degree of

MASTER OF SCIENCE

in the Department of Physics and Astronomy

Developing a QA Procedure for Gated VMAT SABR Treatments Using 10 MV Beam in Flattening-Filter Free Mode

by

Shadi Chitsazzadeh
B.Sc., Shahid Beheshti University, 2005
M.Sc., University of Western Ontario, 2009
Ph.D., University of Victoria, 2014

Supervisory Committee

Dr. Ante Mestrovic, Co-Supervisor
(Department of Physics and Astronomy)

Dr. Magdalena Bazalova-Carter, Co-Supervisor
(Department of Physics and Astronomy)

Dr. Derek M. Wells, Departmental Member
(Department of Physics and Astronomy)

ABSTRACT

Respiratory gating limits the radiation to a specific part of the breathing cycle and reduces the size of the Planning Target Volume (PTV). This thesis describes a novel quality assurance method for amplitude gating of Stereotactic ABlative Radiotherapy (SABR) treatments of liver delivered using Volumetric Modulated Arc Therapy (VMAT) using a 10 MV beam in Flattening Filter Free (FFF) mode. This method takes advantage of the high dose gradient region of SABR treatments to detect any inaccuracies in the performance of the Varian Real-time Position Management (RPM) gating system. This study involves the design and construction of an interface that connects the translation stage of the Quasar respiratory motion phantom to an ion chamber insert. This insert can hold and drive a pinpoint ion chamber inside the ArcCheck diode array based on the breathing pattern imported into the Quasar phantom.

The pinpoint ion chamber dose measurements were acquired at the isocentre and along the penumbra using synthetic breathing traces. Our results show that the changes in PTV size and exhale duration do not influence the dose measured by the pinpoint ion chamber. Changes in gate width and baseline drift, however, affect the detector residual motion, which results in variation in the level of dose-blurring and interplay effects. A new parameter, Average Residual Detector Displacement (ARDD), is introduced in this thesis and is used to take into account the effect of dose-blurring. For gate widths smaller than 8 mm and baseline drift levels smaller than 4 mm, if the effect of dose-blurring is taken into account, the pinpoint ion chamber dose measurements are mostly within 2σ positional uncertainty from the Eclipse dose profile. As the gate width and baseline drift increases, accounting for the dose-blurring effect is no longer sufficient to explain the discrepancy between measured and calculated doses.

This thesis also includes dose measurements for radiation deliveries that are gated using six real breathing traces with gate widths of 2 mm, 2.8 mm, and 4 mm. Once the parameter ARDD is used to account for dose-blurring, the dose measurements are mostly within 2σ positional uncertainty from Eclipse calculated doses. These results demonstrate the reliability and accuracy of the RPM gating system at British Columbia Cancer Agency - Vancouver Island Cancer Centre (BCCA - VICC). Lastly, the overall dose distribution was monitored using the ArcCheck diode array measurements under various gating schemes and was compared to the Eclipse calculated dose map using a 2D Gamma analysis. The Gamma pass rates for 2mm/2% criteria show that the beam interruptions during the treatment do not degrade the fidelity of the radiation delivery in a gated treatment.

Contents

List of Tables

List of Figures

ACKNOWLEDGEMENTS

To Tony, Derek, and Magdalena, thank you for your guidance and support throughout this project. It was a pleasure working with you and learning from all of you. This project would not have been possible without your help.

To Richard, thank you for your helpful comments that improved the quality of this manuscript.

To Magdalena and all of the physicists at BCCA, thank you for being great mentors and helping me with this huge transition in my life.

To Steve, thank you for designing and building the interface, answering all of my questions, and being so generous with your time.

To Dave, thank you for teaching me about the Eclipse and answering all of my questions with so much enthusiasm and positivity.

To Jennifer, thank you for answering all of my questions about the Quasar phantom.

To Derek, Magdalena, Steve, Mark, and Tom, thank you for lending your breathing traces to this project.

To Sam, Mark, and Connor, thank you for all your help and for answering my questions so patiently.

To Marla & Fernando, I wish I could have met friends like in all of my classes. Meeting you has been one of the best things that happened to me in the past two years.

To Shima, thank you for being the best “Best Friend” anybody can ever hope for. You have helped me through everything in my life!

To Maman & Baba, how can I ever thank you enough? I love you!

DEDICATION

To Pedar.

Chapter 1

Introduction

Quality Assurance (QA) is a crucial aspect of any medical treatment. Thorough QA procedures are essential to reduce the probability of accidents and errors at various stages of any given medical treatment. The goal of this study is to develop a QA procedure for gated radiotherapy treatments that involve Volumetric-Modulated Arc Therapy (VMAT) and Stereotactic Ablative Radiation Therapy (SABR) techniques, and are delivered using the 10 MV photon beam in the Flattening-Filter Free (FFF) mode. This project involves the design and construction of an interface that connects the translation stage of the Quasar respiratory motion phantom (Modus Medical) to an ion chamber insert. This insert can hold and move a pinpoint ion chamber inside the ArcCheck diode array (Sun Nuclear Corporation) based on the breathing pattern imported into the Quasar phantom.

1.1 Radiation Therapy

1.1.1 Role of Radiotherapy in Cancer Treatment

Surgery and radiotherapy are the two main modalities of cancer treatment. Although surgery remains the primary form of treatment for early non-metastatic tumours, radiotherapy has proven to accomplish tumour control in several anatomical sites (e.g., head, neck, lung, liver, prostate, and skin). More than half of the cancer patients are estimated to undergo radiotherapy at some point during their treatment for either curative or palliation purposes (Tobias 1996; Delaney et al. 2005). Chemotherapy and targeted agents are the other forms of cancer treatment and are mostly used in conjunction with surgery and radiotherapy.

Radiotherapy involves the use of ionizing radiation to damage tumour cells. Ionizing radiation consists of a beam of particles or electromagnetic wave that has sufficient energy to ionize matter upon collision. This process can occur directly due to the collision between the beam of particles (e.g., electron beam) with the atoms and molecules in the media or indirectly due to the production of charged particles (e.g. photon beam) (Khan 2010). Ejected electrons due to the ionization processes create ionization cascades and leave behind clusters of ionized molecules in the tissue. Ionized molecules are highly reactive and experience rapid chemical changes that leave them with broken chemical bonds and broken molecules, a.k.a. "free radicals". These processes can destroy the structure of macromolecules such as Deoxyribonucleic acid (DNA). The large size of the DNA molecule makes it the biggest target for the damaging properties of ionizing radiation. In addition, DNA's limited turnover, low number of copies (only two), and its crucial role in all cellular functions lead to the serious (and lethal) consequences of damage to the DNA (Joiner and van der Kogel 2009 and references therein). If the damage to the DNA is not rectified by the DNA repair pathways, cell death will occur. This process is the basis of radiation therapy to eliminate tumour cells. The definition of cell death in the context of radiobiology includes not only the processes that lead to destruction of the cell (e.g., apoptosis and auotphagy), but also any process that leads to permanent loss of proliferation (e.g., senescence). The biological response of both tumour and normal cells to radiation and the type of cell death that might occur are determined by the pathways of DNA Damage Response (DDR). The DDR is an intricate system of "sensors" that constantly monitor the genome to detect any damage and "effector pathways" that determine the outcome of the cell damage (death, repair, or permanent or temporary delays in cell cycle progression). DNA repair pathways within DDR focus on rejoining the DNA strand breaks. This rejoining, however, can leave a genetic defect in the cell and the genetic function might not be completely restored. This is often referred to as "mutation". Mutated cells can become malignant later on.

Radiotherapy treatments are based upon delivering enough dose to the malignant cells to prevent their regrowth within patient's lifetime and achieve local control, while allowing the surrounding healthy tissues to recover from the inevitable radiation exposure during the treatment. The side effects of radiation therapy can be categorized into three groups. The early effects appear within the first three months after a course of radiation therapy and are prevalent in tissues that are highly proliferative, such as bone marrow and skin. The late effects appear after the three month period and anytime within the patient's lifetime. These effects can be found in all organs, as well as the connective and vascular tissues. The last side effect of radiation therapy is the induction of secondary cancers. The same mechanism that enables radiation therapy to kill malignant cells can damage the DNA molecules of the surrounding healthy tissues and can increase the risk of secondary cancers later on during the patient's lifetime.

Generally, radiation therapy treatment consists of the following steps. First, a computed tomography (CT) scanner is used to obtain a 3D or 4D image of the patient in the treatment setup position. To achieve a better understanding, the CT images are sometimes supplemented by additional anatomical information by acquiring Magnetic Resonance Imaging (MRI) scans of the patient. Moreover, Positron Emission Tomography (PET) scans of the patient are sometimes obtained to observe tissue metabolic activity and probe the possibility of malignant cells spreading to other organs (a.k.a. metastasis). These images are then used by the oncology and medical physics team to plan an individualized treatment based on patient's anatomy and location and size of the target volume. The treatment is delivered in several fractions. The total dose, dose per fraction, and number of fractions depend on the tumour and treatment type. Daily images of the patient are also acquired before delivering each treatment fraction to ensure the accuracy and reproducibility of the setup position and treatment delivery.

1.1.2 Structure of Medical Linear Accelerator

A modern medical linear accelerator (linac) is an apparatus most commonly used for external beam radiotherapy. It consists of a gantry isocentrically mounted on the gantry stand. The gantry rotates around the treatment couch. This configuration allows for the radiation treatment to be delivered from various angles. The geometry and the material used in the construction of the treatment room are specifically designed to shield the outside areas from the radiation. Finally, the control console is located outside of the treatment room to shield the radiotherapists who deliver the treatments. Figure 1.1 shows the basic component of a medical linac, in this case a TrueBeam Radiotherapy System from Varian Medical Systems.

Medical linacs produce photon beams by accelerating electrons to relativistic speeds in waveguides using microwave radiation. The collision of these high energy electrons ($6 - 18$ MeV) with a heavy metal target produces high energy X-rays

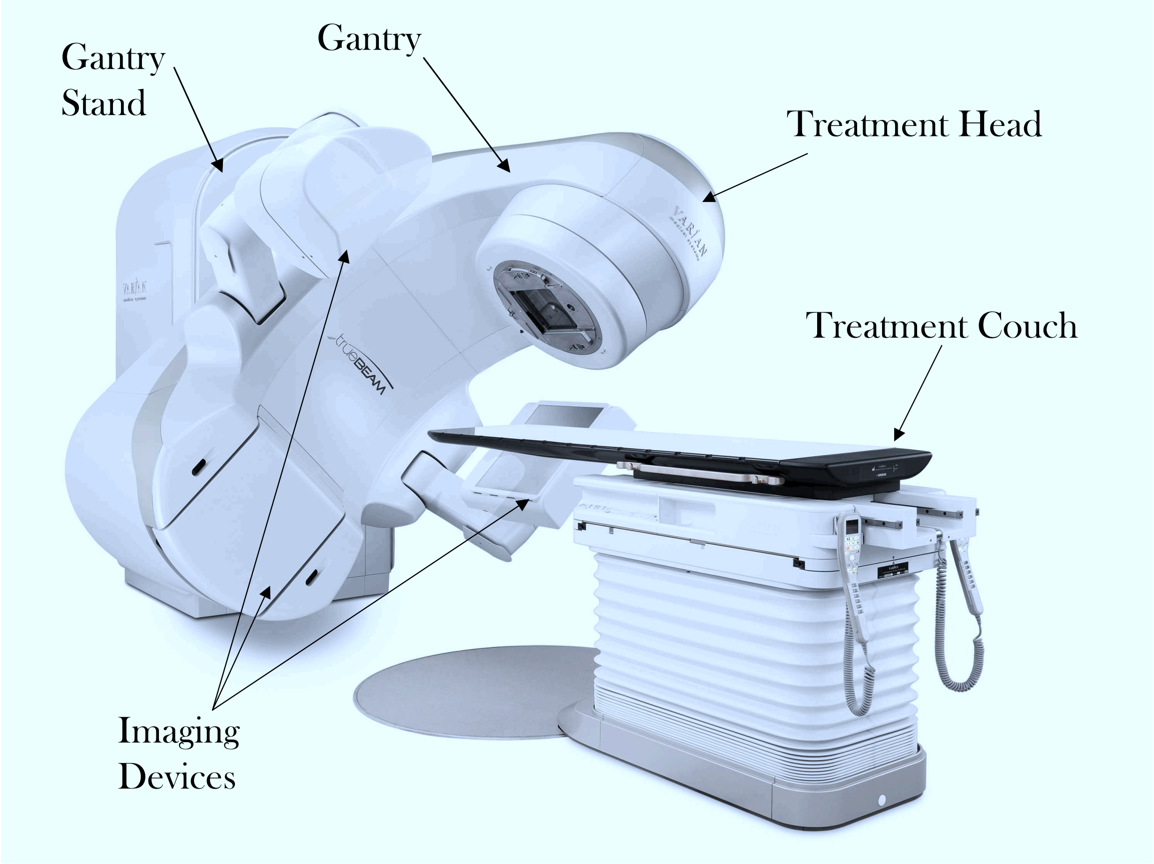

Figure 1.1: Basic components of a medical linac. TrueBeam Radiotherapy System from Varian Medical Systems.

as a result of the bremsstrahlung process. The X-ray beam is then shaped using the collimation and flattening devices of the linac: The highly attenuating material in the conical **primary collimator** absorb the scattered radiation from the target. The beam then passes through a cone-shaped **flattening filter** that attenuates the forward-peaked high intensity part of the photon beam more than the beam edges ensuring the beam uniformity across the treatment field. Two sets of independent **monitor ion chambers** continuously measure the beam output in arbitrary units called monitor units (MU)[1] and inspect the beam flatness and symmetry. The jaws of the **secondary collimator** define a rectangular field (size of up to 40 cm × 40 cm at isocentre). Finally, the movement of the **multi-leaf collimator (MLC)** allows for customized irregular field shaping. Figure 1.2 shows the components of a standard medical linac head in the photon mode.

---

[1] Linacs are generally calibrated so that 1 MU corresponds to 1 cGy at the depth of d_{max} in a water phantom for a 10 cm ×10 cm radiation field and source-to-axis distance of 100 cm.

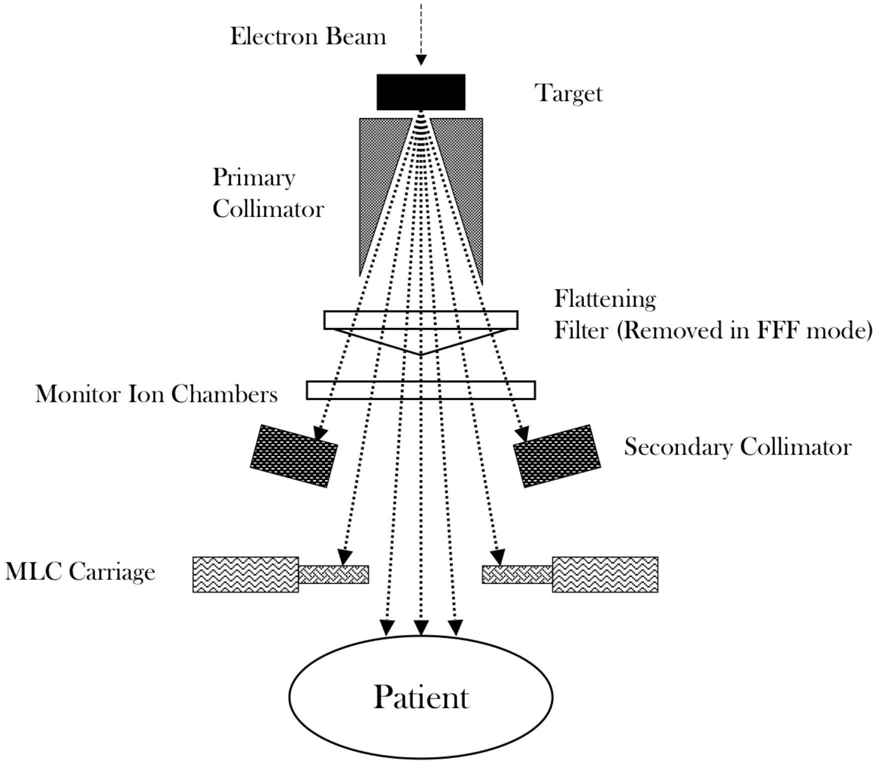

Figure 1.2: Basic components of a medical linac head.

1.1.3 Modern Treatment Techniques

During the past 15 years several new and sophisticated radiation therapy techniques have been developed. These techniques take advantage of beam intensity modulation and variation in gantry angle to improve the conformity of dose distribution to the target volume.

First developed in 1995 by Ling et al. (1996), Intensity Modulated Radiation Therapy (IMRT) uses the linac MLC to selectively modulate the fluence at certain beam angles. Such nonuniform fluence in the treatment beam allows us to achieve highly conformal dose distributions. Conventional treatment techniques are developed using forward planning, which adds the radiation fields to the plan and compares the resulting dose distribution with the dose constraint by trial and error. IMRT plans, however, are developed using inverse planning, in which a computer software optimizes a fluence map to match the dose constraints. The corresponding MLC leaf positions are determined accordingly.

Volumetric Modulated Arc Therapy (VMAT), developed by Otto (2008), uses the modulated beams of IMRT in conjunction with gantry rotation. The variable

MLC leaf position, gantry speed and dose rate of VMAT yield highly conformal dose distributions while decreasing the treatment times. The VMAT treatment planning begins with modelling the continuous gantry motion using a coarse sampling of static gantry positions. An instantaneous MLC aperture shape is defined for each sample of the gantry position. After a few iterations of MLC and MU weight changes, a gantry position sample is added to the existing pool of samples and the corresponding MLC aperture shape is found by linear interpolation from the aperture shapes of the adjacent samples. The MU weight of the newly added sample is calculated using the MU weight of the adjacent samples. In the same manner, the gantry and MLC position samplings are progressively increased during the optimization to generate a highly conformal treatment plan.

Stereotactic ABlative Radiotherapy (SABR) involves the delivery of high doses of radiation to the target volume in a small number of fractions (hypofractionation) using highly focused megavoltage photon beams. Due to the high doses of radiation involved in this type of treatment, small margins are imperative to minimize normal tissue toxicity. Based on the successful clinical trials of SABR in the past decade, this type of treatment has now become a common procedure for small tumours in the lung and liver (e.g., Nagata et al. 2005; Timmerman et al. 2007; Rusthoven et al. 2009). Currently, at British Columbia Cancer Agency (BCCA), VMAT SABR treatment is used to treat Non-Small Cell Lung Cancer (NSCLC) and Hepatocellular Cancer (HCC). Generally, NSCLC is treated by delivering a total dose of 48 Gy in four fractions. HCC, however, is treated with a total dose of 45 Gy in three fractions (or five fractions if the dose constraints are not met using 15 Gy per fraction). One disadvantage of SABR treatments is the increase in treatment times per fraction due to the delivery of high radiation dosage. Extended treatment times can increase intra-fraction error, especially for patients that are immobilized in uncomfortable setup positions, and can lead to increase in normal tissue toxicity. Long treatment fractions are also clinically inefficient.

1.1.4 Flattening Filter Free Beams

Medical linacs produce photon beams through bremsstrahlung process by directing a beam of high energy electrons to a metal target. The resulting photon beam has a continuous spectrum of energy with the maximum energy equal to that of the initial electron beam. The angular distribution of the produced photons depends on the initial kinetic energy of the electron beam, with the higher electron kinetic energy producing more forward peaked photon beams, meaning that the maximum photon intensity is along the central axis of the beam. In the past, treatment planning calculations were done manually and therefore flat photon beams were necessary to simplify the treatment planning calculations. With the advancement of treatment planning and delivery systems, it is now possible to use inverse planning to construct treatment plans using non-uniform photon beams. Therefore, flattening filters are no longer necessary in the beam line of medical linacs. By maintaining the central axis high intensity bremsstrahlung peak of the photon beam in the Flattening Filter Free (FFF) mode, the radiation can be delivered at a much higher dose rate. For instance, the Varian TrueBeam (Varian Medical Systems, Palo Alto, CA), one of the first commercially available medical linacs that offers FFF beams, produces flattened photon beams at a dose rate of 600 MU/minute. Removing this filter, however, can increase the dose rate to 2400 MU/min and reduce the treatment time by more than 50% (Cashmore 2008; Vassiliev et al. 2009). Therefore, delivering VMAT SABR treatments using FFF beams can offset the long treatment times of SABR technique, while maintaining dosimetric quality and accuracy equivalent to that of flattened beams (e.g., Scorsetti et al. 2011; Nicolini et al. 2012). Another advantage of FFF beams is their significantly reduced out-of-field (a.k.a., peripheral) radiation dose as a result of the decrease in head scatter (Dalaryd et al. 2010) and MLC leakage radiation (Kragl et al. 2009).

1.2 Motion Management

The goal of radiotherapy is to kill tumour cells by delivering radiation and simultaneously minimizing the damage to the surrounding healthy tissue. Modern techniques, such as IMRT and VMAT are able to sculpt the radiation beam to match the shape of the tumour, allowing us to achieve a more effective treatment by increasing the dose to the target volume and reducing the dose delivered to the surrounding normal tissue. The effectiveness of such complex techniques, however, depends strongly on accurate knowledge of the target location during the planning stage, and more importantly during the treatment delivery. In the thorax and abdomen, intra-fraction movement due to respiration not only changes the location of the tumour during the breathing cycle but also distorts its volume and results in large safety margins. Such significant uncertainties can lead to an increase in healthy tissue irradiation. The simplest and most common method to account for respiratory motion in radiotherapy is to choose a large enough target volume to encompass the entire tumour motion during the breathing cycle and ensure that the target receives the prescribed dose. More sophisticated methods have also been employed to account for respiratory motion, such as abdominal compression, breath-hold, respiration gating, and real-time tumour-tracking. These methods will be described in further detail in Chapter 2.

Amplitude gating has been implemented at BCCA Vancouver Cancer Centre (VCC) for VMAT SABR treatments of liver HCC using 10 MV FFF beam. The corresponding gating procedure was developed by Viel et al. (2015) using the Quasar respiratory motion phantom (Modus Medical Devices Inc., London, ON, Canada), a Farmer-type ion chamber, and Gafchromic EBT3 film (International Specialty Products, Wayne, NJ, USA).

Gated VMAT SABR treatments of liver have not yet been implemented at BCCA Vancouver Island Cancer Centre (VICC). The goal of this project is to develop a gating QA procedure for implementation of Gated VMAT SABR treatments of liver at VICC. Our QA procedure involves the use of a custom made interface that connects the translation stage of the Quasar phantom to an ion chamber insert, which can hold a pinpoint ion chamber and move it inside the ArcCheck diode array (Sun Nuclear Corporation) based on the imported breathing pattern. In this method, the overall dose distribution accuracy is tested using ArcCheck measurements. The accuracy of the gating system to deliver the dose in the correct part of the breathing cycle, however, is probed using the pinpoint ion chamber measurements in the penumbra. Due to the sharp dose gradient of the penumbra, the pinpoint chamber measurements are highly dependent on the position of the active volume of the chamber and therefore are excellent probes of the accuracy of the gating system. One of the advantages of this setup is allowing the user to acquire both diode and ion chamber measurements simultaneously by delivering the treatment plan only once. In addition, this method does not involve the labour intensive and time consuming process of film dosimetry and analysis.

1.3 Thesis Overview

The goal of this thesis is to develop a QA procedure for gated VMAT SABR treatments of liver using the 10 MV FFF beam on the Varian TrueBeam (Varian Medical Systems, Palo Alto, CA). We have designed and constructed an interface that connects the translation stage of the Quasar respiratory motion phantom (Modus Medical Devices Inc., London, ON, Canada) to an ion chamber insert. This insert can hold and move a pinpoint ion chamber inside the ArcCheck diode array (Sun Nuclear Corporation) according to the breathing pattern read by the Quasar phantom. To investigate the reliability of gated VMAT SABR treatments and to explore the effects of various breathing traces and gate sizes on the quality of gating technique, we have used this setup to take dose measurements along the penumbra region for three liver VMAT SABR plans using various synthetic and real breathing traces.

Chapter 2 covers the background information relevant to this study. An overview of various motion management techniques in radiotherapy are described. Furthermore, the quality assurance procedures corresponding to medical linacs and various radiotherapy techniques are discussed. Finally, the motivation behind the use of gated VMAT SABR techniques for treating HCC is explained.

Chapter 3 outlines the materials and methods used in this project. The main components of the Quasar respiratory motion phantom and ArcCheck diode array and their corresponding softwares are described. We also discuss our method of measurements using each device.

We present and discuss the results of our measurements using the synthesized and real breathing traces in Chapters 4 and 5, respectively. Finally, Chapter 6 will present the thesis conclusion and suggestions for future work.

Chapter 2

Background

This chapter will cover the background information required for this project, including an overview of various methods that are employed for motion management in radiotherapy, a description of different types of QA procedures required in external beam radiotherapy, and the background knowledge regarding HCC.

2.1 Motion Management

2.1.1 Accounting for Motion in the Planning Target Volume

To ensure the consistency and clarity of radiation therapy treatment planning and dosimetry, the International Commission on Radiation Units and Measurements (ICRU) defines the following volumes. The Gross Tumour Volume (GTV) encompasses the visible extent of the tumour in the CT scans. The Clinical Target Volume (CTV) includes the GTV in addition to the subclinical microscopic malignant disease that has to be eliminated. To account for tumour motion, Internal Target Volume (ITV) includes the CTV and a (usually) asymmetric margin encompassing the CTV. Finally, the Planning Target Volume (PTV) is created by adding the set-up margin around the ITV. Figure 2.1 shows a schematic of the different volumes used in treatment planning.

The boundaries of the ITV are determined by acquiring a four-dimensional CT (4DCT) scan using a device that can monitor the patient's breathing pattern. At BCCA-VICC, all six TrueBeam linacs and both of the CT scanners are equipped with the Real-time Position Management (RPM) system (Varian Medical Systems), which is capable of recording patient's breathing pattern. The RPM system is comprised

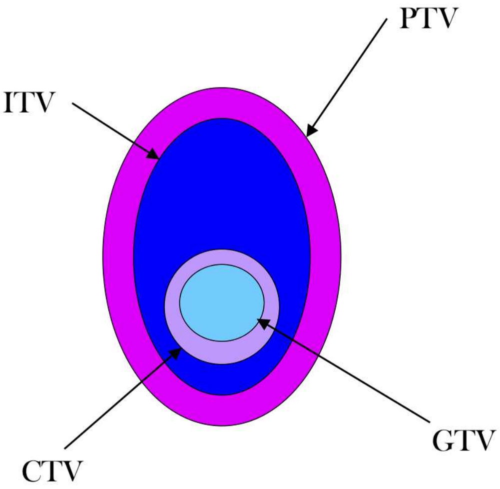

Figure 2.1: Illustration of various target volumes used in treatment planning.

of a tracking camera that emits infrared light. The patient lies on the CT couch and a six dot marker block is placed on the patient (usually between the umbilicus and the xiphoid) within the field of view of the camera. The infrared radiation from the camera bounces off of the six reflective dots on the marker block, the camera captures this signal and uses it to analyze and record the motion of the marker block and patient's abdomen in three vertical, longitudinal, and lateral dimensions. The CT slices are then binned according to the phases of the breathing cycle to yield the 4DCT dataset. This dataset can be used to produce a Maximum Intensity Projection (MIP; i.e., an overlay of the maximum intensity of each voxel during the breathing cycle). The MIP can then be used to accurately determine the extent of the ITV.

Although this method ensures a complete dose coverage of the tumour, it exposes the surrounding normal tissue to higher levels of radiation dose and therefore might increase the probability of secondary cancer. This effect is especially a concern in SABR treatments due to the high amount of dose delivered in each fraction, the steep dose gradient, and the small PTV margins.

2.1.2 Abdominal Compression

Abdominal compression is an efficient technique to reduce the amplitude of respiratory tumour motion and is widely used for patients undergoing lung SABR treatments. This technique involves placing a pressure plate on the patient below the xiphoid. The plate is then firmly attached to the treatment couch or the stereotactic body frame using a graduated screw, which is tightened to decrease the motion amplitude.

There are, indeed, some disadvantages associated with abdominal compression. This method can be difficult to tolerate for some patients. Also, reproducing the compression effect during the course of the treatment has proven to be challenging due to the changes in patient's anatomy and respiratory pattern (Heinzerling et al. 2008). Moreover, some studies have suggested that abdominal compression can increase the variation in tumour motion (Bissonnette et al. 2009; Mampuya et al. 2013).

2.1.3 Breath-hold

Breath-hold techniques can help minimize the tumour motion due to respiration and therefore reduce treatment planning margins. Breath-holds are either performed voluntarily or using an Active Breath-hold Control (ABC) system (i.e., Active Breathing Coordinator; Elekta, Crawley, England).

A voluntarily performed Deep Inspiration Breath-Hold (DIBH) involves instructing the patient to breathe to a specific threshold and then maintaining that level of inspiration during every delivered radiation therapy field. The patient can recover with normal breathing in between breath-holds. The breathing pattern of the patient is continually monitored throughout the treatment using the RPM system (described in section 2.1.1). The DIBH technique is most commonly used in left breast treatments to lower the dose delivered to the heart and has consistently shown to be an effective method (Hayden et al. 2012; Rochet et al. 2015; Latty et al. 2015). Optimum coaching and visualization methods (such as computer monitor or display goggles) that help patient see the breathing trace can improve the outcome of treatments that involve the DIBH technique.

An ABC system consists of a digital spirometer attached to a balloon valve. A clip is placed on patient's nose to prevent them from nasal respiration. As the patient breathes through a mouthpiece connected to the ABC apparatus, their breathing trace is shown on a monitor, and inspiration is held at a specific lung volume (see e.g., Wong et al. 1999; Gagel et al. 2007). This technique provides a significant and reproducible reduction in diaphragm motion, enabling reduction of treatment planning margins. Similar to the abdominal compression, the feasibility of both DIBH and ABC techniques depends heavily on patient's compliance.

2.1.4 Respiratory Gating

Respiratory gating was first introduced by Ohara et al. (1989). This technique involves the continuos monitoring of the patient's breathing pattern during the treatment and delivering the radiation only during a specific part of the patient's breathing pattern. Various devices have been employed to record the patient's breathing trace using external surrogate markers. For instance, the Varian RPM system uses the infrared radiation reflected from a six-dot marker block to record the breathing trace (described in section 2.1.1) and the Anzai belt (Anzai Medical, Tokyo, Japan) uses a strain gauge that is attached directly to the patient to detect the abdominal movements by measuring pressure variations. The signal is then sent to the imaging device or to the linac. The corresponding software analyzes the patients breathing trace and controls the beam accordingly. The strong correlation between diaphragm motion and the motion of tumours in the liver and lower lobe of the lungs lends credibility to using external surrogate markers as probes of the tumour motion (Vedam et al. 2001; Bortfeld et al. 2005; Yang et al. 2014). It is still crucial, however, to continually validate this correlation throughout each fraction and the entire course of the treatment by placing internal fiducial markers near the tumour site and imaging them using the kV imaging capabilities of the linac.

Respiratory gating is categorized into phase and amplitude gating based on the method of determining the gating window. As the name suggests, **phase gating** restricts the treatment delivery to a specific phase of the breathing pattern. This method is appropriate if the breathing pattern is regular and periodic, as the gating system would not be able to accurately estimate the period of the breathing trace for irregular breathing patterns. Furthermore, for breathing traces with irregular amplitudes and baseline drifts, phase gating can result in the beam being turned on when the target is not necessarily within the positional window of interest, which can lead to inaccuracy in dose delivery to the target. On the other hand, **amplitude gating** only turns the beam on when the position of the surrogate marker is within the pre-designated upper and lower thresholds. Although inefficient when the breathing trace shows high degrees of baseline drift, amplitude gating ensures that the dose is delivered to the target only when it is within the pre-designated positional boundaries, and therefore is dosimetrically more accurate. Therefore, amplitude gating at exhale, which is the most stable portion of the breathing cycle, is our method of choice.

Gated treatments can be inefficient and lengthy due to multiple beam interruptions during each treatment fraction. This issue can be solved to some degree by coaching the patients through audio-visual feedback to maintain the exhale for a longer time and within the gating window.

2.1.5 Real-time Tumour-Tracking

The most sophisticated and complex method proposed for motion management is to track the tumour in real-time. The efforts to achieve tumour tracking can be categorized into finding the tumour position in real-time and adapting the beam (Giraud and Garcia 2010).

Various methods have been proposed for localizing the tumour in real-time. Implanting high-Z fiducial markers is one of the common ways of tumour localization (see e.g., Schweikard et al. 2000; Shirato et al. 2000; Chen et al. 2001). The procedure can be done either endoscopically or percutaneously, although the latter is undesirable in case of lung tumours due to the risk of pneumothorax (Bhagat et al. 2010). Usually three or four markers are implanted to allow the monitoring of marker migration as well as tumour rotation (Murphy 2004). Another method of choice is to use non-radiographic techniques such as implanting small radiofrequency transponders that can be detected magnetically in 3D. The transponder tracking technology has been proposed by many groups (see e.g., Seiler et al. 2000). The Calypso system (Varian Medical Systems Inc., Palo Alto, California, USA) is the first clinically available system that uses the transponder tracking technology (Mate et al. 2004). This system uses three implanted transponders (a.k.a, beacons) with resonance frequencies of 300, 400, and 500 kHz. The beacons are excited by an external magnetic field created by the source coils included in the tracking system and emit a signal that is then measured by a sensor array. Based on the sensor data, a tracking algorithm determines the position of the beacon. The beacons are excited and localized sequentially. Another alternative is the real-time tumour-tracking using 3D ultrasound (Meeks et al. 2003). Lastly, for small well-defined lung tumours, the density difference between the tumour and the normal tissue might be large enough to make the tumour mass directly detectable on radiographic images. Therefore, early stage lung cancer patients may in some cases benefit from fluoroscopic tumour tracking (Berbeco et al. 2005).

Once the tumour location is acquired in real-time, the radiotherapy system can adapt and respond in four different ways (Murphy 2004): (1) move the patient by remotely moving the couch, (2) move a charged particle beam using electromagnetic fields, (3) move the beam by using a linear accelerator that is mounted as a robotic arm, or (4) adapt the beam by using dynamic MLC. The non-rigidity of human anatomy makes the first option dosimetrically inaccurate. This method is also undesirable due to the constant movement of patient's body. The third method is implemented clinically as the CyberKnife Robotic Radiosurgery System, which consists of a small 6 MV linac mounted as a robotic arm. Finally, beam adaptation using dynamic MLC and adaptive treatment planning is an active area of research and has been explored by many groups (see e.g., Keall et al. 2001; Neicu et al. 2003; Keall et al. 2005; Papiez et al. 2005; Mestrovic et al. 2009).

2.2 Patient Positioning & Immobilization

Patient setup and immobilization play crucial roles in minimizing the radiation exposure to healthy tissues. This is especially true when it comes to SABR treatments, as a result of their high dose per fraction and small margins. At VICC, patient positioning and immobilization for lung SABR VMAT treatments is done using the Freedom system designed for SRS/SBRT treatments by CDR systems (Calgary, Canada). The Freedom system indexes directly to the treatment couch and is equipped with head rest, arm rest, leg rest, and foot rest pieces. Furthermore, Vac-Lok bags can be used together with this system to assist with patient immobilization and reproducible patient positioning. For lung tumors located closer to head and neck, the patient is asked to rest their arms downward and a head and neck shell is used for stability and reproducibility of the setup. For tumors that are located in the lower regions of the lungs, the patient rests their arms upward to reduce the radiation exposure to the arms. To ensure the reproducibility of patient positioning, the locations of lasers on the patient's body are marked with tatoo in the middle and on the sides.

To verify the setup, the patient is first imaged with a half-arc cone beam CT (CBCT). The image registration to soft tissue or bony anatomy is then performed with a large field of view to detect gross positional uncertainties and to manually correct any possible displacement (greater than 1cm) or rotation (greater than $3^{\circ}-4^{\circ}$) corrections in patient positioning. The image registration is then performed with a smaller field of view to the tumor and its vicinity (the region within 2 cm around the tumor). Currently at VICC, couches with three degrees of freedom are used for VMAT SABR treatments and therefore only displacement corrections in lateral, longitudinal, and vertical directions are applied at this stage. Using a treatment couch with six degrees of freedom, would allow us to apply further rotation corrections using the couch.

For liver VMAT SABR treatments, the verification of patient setup will be done by imaging the patients using 4D-CBCT, such that the image used for verification is gated to the same part of the patient breathing cycle as was used for treatment planning. Internal fiducial markers will be placed close to the tumor and will be used for image registration.

2.3 Quality Assurance

Development and performance of QA procedures are essential to validating the accuracy of a device or a technique. In the field of medical physics, QA checks are performed regularly (daily, weekly, monthly, and annually), and necessary corrective actions are taken according to the QA results.

2.3.1 Linac QA

The American Association of Physicists in Medicine (AAPM) Task Group report 142 (TG142; Klein et al. 2009) summarizes the recommendations on the regular linac QA checks, tolerance levels, and the appropriate action levels. The daily and weekly tests focus on parameters that can affect the radiation delivered to the patient dosimetrically or geometrically. Beam output constancy checks, mechanical checks such as laser localization and collimator size, and safety checks on certain features such as door interlock and audiovisual monitor are a few examples of tests that are performed on a daily or weekly basis. The monthly QA procedure consists of most of the daily and weekly tests in addition to extra checks that include but are not limited to photon and electron beam profile constancy and light/radiation field coincidence for jaw and MLC defined fields. Lastly, the annual checks include tests on photon and electron beam symmetry flatness, and quality, and rotation of collimator, gantry, and couch.

QA checks on the performance of respiratory gating system should be included in both monthly and annual QA protocols. At BCCA−VICC, the monthly QA of the RPM system is done using a motion phantom provided by Varian Medical Systems that simulates a pattern similar to a typical breathing pattern. The RPM marker block is placed on the phantom platform and its motion is tracked by the RPM camera. The motion amplitude and the gated residual motion are tested with a tolerance level of ±2 mm. The cycle period and the total beam-on time are also tested with ±0.2 s and ±0.02 min tolerance levels, respectively.

2.3.2 SABR QA

The QA procedures described in section 2.3.1 apply to the linacs that are intended for SABR treatments, with the lower tolerance level being the major difference. For instance, the recommended tolerance level for mechanical tests such as laser localization and collimator size indicator is ±2 mm for general daily linac QA and ±1 mm for linacs that are intended for SABR treatments.

2.3.3 VMAT & IMRT QA

Specific checks are required to ensure the performance accuracy of the MLC, for instance checking the leaf positional accuracy and transmission values. At BCCA-VICC, these tests are performed using the Electronic Portal Imaging Devices (EPID) on the linac. The most common test is referred to as the "picket fence", which tests the stability of the MLC and the reproducibility of the gap between the leaves. These tests consists of sequential leaf movements of a rectangular field spaced at equal intervals. The picket fence test is performed at four different gantry angles (0°, 90°, 180°, and 270°) as well as throughout a complete gantry arc to check the effect of gravity and gantry rotation on the alignment and position of the leaves. Furthermore, the dose constancy for various VMAT and IMRT leaf sequences are checked against the dose output of a 6 MV beam for a 10 cm × 10 cm open field using a Farmer-type ion chamber placed in solid water. In addition, size of the MLC junction peaks are compared with and without carriage movements at gantry angle of 0°. Lastly, for all leaf pairs all junction peaks are compared to an average value.

2.3.4 Patient-specific QA for VMAT SABR treatments

Patient-specific QA consists of validating a patient treatment plan by delivering it to a phantom and verifying the dose accuracy by measuring the dose using a dosimeter. At BCCA−VIC, lung treatments are performed using VMAT and SABR techniques utilizing the 10 MV beam in FFF mode. For each treatment plan, patient-specific QA is performed using the ArcCheck diode array (Sun Nuclear Corporation; described in section 3.1.2) and a pinpoint ion chamber (described in section 3.1.3). In order to perform the patient-specific QA, a verification plan is created in the Eclipse treatment planning system (Varian Medical Systems) using an artificial CT dataset of the ArcCheck. The verification plan is then delivered to the actual ArcCheck with the pinpoint ion chamber placed inside the ArcCheck so that the active volume of the chamber is at the isocentre. The dose measurement map from the diodes is compared with the map calculated by the Eclipse using the SNC Patient software (Sun Nuclear Corporation). A 2D Gamma analysis is performed to ensure that a high percentage of data points meet the pre-designated criteria for the Gamma test (2 mm/2%). This analysis is done for diodes with measured doses greater than 10% and 40% of the maximum dose. A Gamma pass rate greater than 90% is considered acceptable for these measurements. The dose measured using the pinpoint ion chamber is also compared to the Eclipse predicted dose to a cylindrical structure with dimensions comparable to those of the active volume of the ion chamber and contoured at the centre of the ArcCheck CT dataset. A 3% tolerance level is used for this comparison. In the near future, Monte Carlo methods will be used to validate patient specific dosimetry for VMAT SABR treatments at VICC.

2.3.5 Gating QA for VMAT

Coupling gated treatments with fast delivery techniques such as VMAT (especially in FFF mode) allows us to offset the inefficiency of gated treatments and deliver high dose per fraction of SABR treatments while maintaining reasonable treatment times. Validating the quality of gated VMAT treatments is a challenging task, however, due to the variation in MLC leaf position, gantry angle, and dose rate during the treatment. The first study that investigated the feasibility and dose fidelity of VMAT treatments in conjunction with gating was presented by Nicolini et al. (2010). This study was carried out in a pre-clinical framework using six patient treatment plans constructed using single arcs and prescribed doses of 2, 5, and 15 Gy. The treatment deliveries were gated with various gating window sizes. Measurements were taken using PTW-729 2D array combined with the stationary Octavius phantom (PTW, Freiburg) and compared with the treatment planning system calculated doses. The results confirmed that gated VMAT treatments are reliable and dosimetrically accurate. Qian et al. (2011) developed a dose reconstruction technique based on the linac log files and compared the dose calculations of gated VMAT deliveries with dose measurements acquired with the stationary Seven29 (i.e., a 27 × 27 ion chamber array; PTW, Freiburg, Germany). The measurements were performed for three plans with prescribed doses of 450 cGy, 500 cGy, and 1250 cGy using three regular simulated respiratory patterns with periods of 3 s, 4.5 s, and 6 s. The results further validated dosimetrical fidelity of the gated VMAT technique. Both of the studies mentioned above used stationary phantoms to obtain measurements and therefore did not explore the effect of the detector residual motion within the gating window.

Li et al. (2012) evaluated the geometric accuracy of gated VMAT treatment using intra-fraction kV images and CIRS dynamic thorax phantom. The amplitude gated VMAT treatment was delivered by a TrueBeam linac. An RPM block was placed on the phantom platform to generate the gating signal for the RPM system. In order to investigate the effects of the phase difference between the target and surrogate motions, the treatment was delivered while introducing phase shifts of 0%, 5% and 10% of the entire breathing cycle between these two motions. For both simulated and real breathing traces, Li et al. (2012) found high geometric accuracy when the surrogate and the target are in phase (average error: 0.8 mm in the SI direction). However, higher levels of geometric error occur for non-zero phase differences. They carried out similar measurements on real patients and achieved an average intra-fraction positioning errors of 0.8, 0.9, and 1.4 mm in the LR, AP, and SI directions, respectively.

Viel et al. (2015) explored the effect of amplitude gating on VMAT SABR treatments of liver using 10 MV FFF beams on ten patients. The dose measurement was done using Gafchromic film and a Farmer-type ion chamber. For each patient, the measurements were taken using both their free and coached breathing patterns (with extended exhale). The gated deliveries were in good agreement with the non-gated deliveries and the Eclipse dose prediction. The results of this study strongly suggest that a coached breathing pattern in conjunction with a 5 mm gating window results in high dose fidelity and reasonable gated delivery times.

2.4 Hepatocellular Carcinoma

Hepatocellular Carcinoma (HCC) is the most common type of liver cancer. It ranks as the third most deadly and sixth most common type of cancer (Jemal et al. 2011; Forner et al. 2012). Globally, more than 700,000 cases of HCC were diagnosed in 2008.

Inspiration involves contraction of the diaphragm, which causes it to move downward, resulting in pulmonary expansion. During the expiration, the internal intercostal muscles contract and pull the rib cage downward increasing abdominal pressure which forces the diaphragm up. Many organs are influenced by the respiratory motion such as, lungs, liver, kidney, and pancreas, with the liver being the most mobile (Suramo et al. 1984). Liver is located below the diaphragm and therefore is heavily affected by respiratory motion (Weiss et al. 1972; Harauz and Bronskill 1979; Suramo et al. 1984; Davies et al. 1994). Many studies have reported measurements on the amplitude of liver tumour motion. For instance, Kitamura et al. (2003) measured the liver tumour motion of 20 patients using 2 mm gold fiducial markers and fluoroscopy. The average amplitudes of liver tumour motion in three directions were found to be: $4{\pm}4$ mm (range: $1{-}12$ mm) in the right-left (RL) direction, 5 ± 3 mm (range: $2{-}12$ mm) in the anterior-posterior (AP) direction, and $9{\pm}5$ mm (range: $2{-}19$ mm) in the superior-inferior (SI) direction. Another example is the study done by Wagman et al. (2003), where fluoroscopy was used to measure the average displacement of liver tumours in three directions: $1.92{\pm}1.52$ mm (LR), $6.14{\pm}3.65$ mm (AP), $12.15{\pm}5.59$ mm (SI). Such deviations in the position of the tumour can be clinically significant and potentially degrade the effect of the radiotherapy techniques, especially for SABR treatments that require smaller margins. As a result, only a small number of liver patients (with very small tumours) have been eligible for liver SABR treatments. Gated SABR treatments of liver are desirable because they restrict the treatment delivery to a limited part of the breathing cycle and reduce the risk of normal tissue toxicity. The combination of gating and SABR techniques will hopefully make liver treatments beneficial for a larger number of patients.

Chapter 3

Materials and Methods

3.1 Materials

This chapter will cover an overview of the devices and the setup used in this project. The strategy for treatment planning and measurements are also described in this chapter. Finally, this chapter includes the definitions of the quantities and parameters used in our analysis and a description of the sources of error involved in gated radiation deliveries.

3.1.1 Quasar Respiratory Motion Phantom

The Quasar respiratory motion phantom (Modus Medical, London, ON, Canada) is a programmable breathing simulator. It consists of a programmable drive unit held in place by a body oval. The unit contains a stepper motor that drives the translation stage in the SI direction and rotates two cams that move the chest wall platform in the AP direction. Various types of moving inserts are available that can be inserted into the body oval and attached to the translation stage to be driven in the SI direction. Note that none of the moving inserts were utilized in this project. The chest wall platform is used to hold the RPM block. Figure 3.1 shows the main components of the Quasar phantom.

The Quasar phantom operates in the three following modes:

(1) Rotation Mode: This mode yields a sinusoidal motion profile. The speed can be controlled either using the control knob (manually) or through the Quasar software. The maximum peak-to-peak amplitudes of the translation stage and the chest wall platform are 40 mm and 10 mm, respectively.

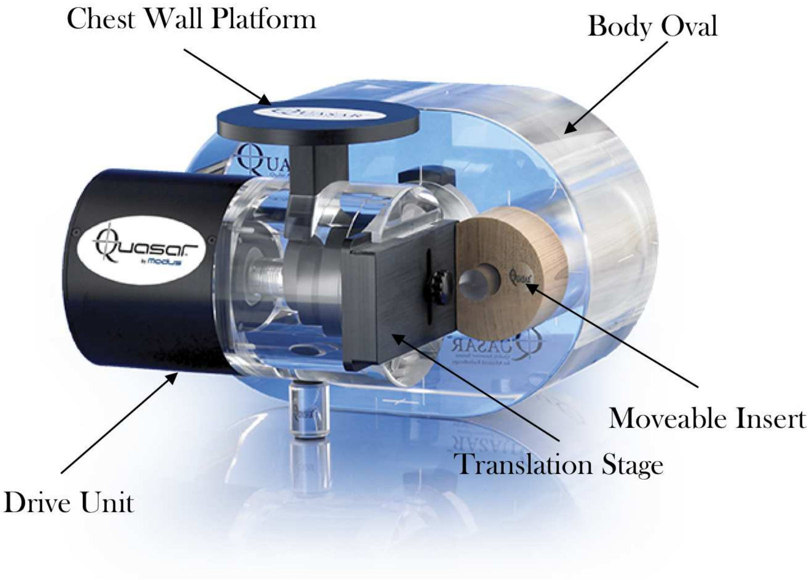

Figure 3.1: The main components of the Quasar respiratory motion phantom (Image courtesy of Modus Medical).

(2) Position Mode: This mode is used to set the position of the translation stage and the chest wall platform. This mode can be accessed both manually and using the Quasar software. Similar to the rotation mode, the maximum peak-to-peak amplitudes of the translation stage and the chest wall platform are 40 mm and 10 mm, respectively.
(3) Oscillation Mode: This mode is only accessible through the Quasar software. It can be used to feed real breathing traces to the phantom or create and edit simulated breathing patterns. In this mode, the maximum peak-to-peak amplitudes of the translation stage and the chest wall platform are 30 mm and 7.5 mm, respectively.

For the majority of this project, we used the Quasar phantom in the oscillation mode. We have used six real breathing traces as well as simulated breathing traces created using the Quasar software.

The Quasar software consists of the two following modules:
Phantom Control: This module allows for importing real and simulated breathing patterns and accessing all three operation modes (explained above). The "Waveform" tab of the control module displays the imported trace (i.e., the expected motion) as well as the the actual motion of the translation stage. The "Motor" tab shows the

animated view of the motor motion.

Wave Editor: This module can be used to create and edit real and simulated breathing traces.

3.1.2 ArcCheck Diode Array

The ArcCheck Diode Array (Sun Nuclear Corporation) is a 3D diode array with 1386 diode detectors placed on a cylindrical structure. The size of the diode detectors is 0.8×0.8 mm^2. The hollow cylindrical structure is 21 cm in length and 21 cm in diameter. The cavity can be used to plug in various types of dosimeter inserts such as, ion chamber or Gafchromic film. Figure 3.2 shows the main components of the ArcCheck diode array.

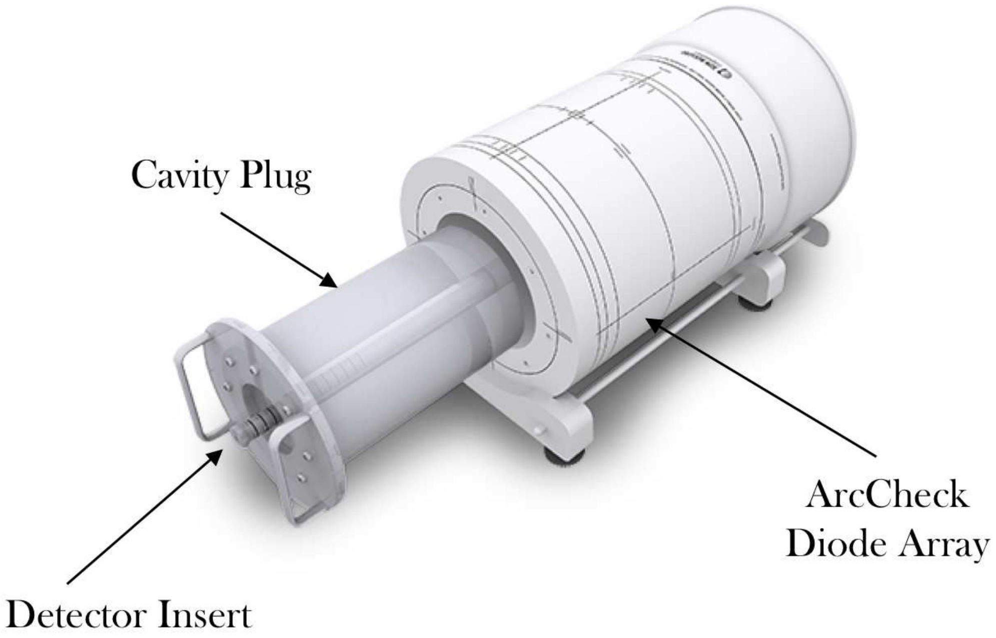

Figure 3.2: The main components of the ArcCheck diode array (Image courtesy of Sun Nuclear Corporation).

The SNC Patient software is the ArcCheck's computer interface. DICOM dose maps of a verification plan can be imported into the software. Subsequently, a dose grid corresponding to diode locations is constructed for comparison to the measured dose map during the QA. The comparison can be done using Gamma analysis with user specified parameters and thresholds.

3.1.3 Pinpoint Ion Chamber

In this study, we have used the pinpoint ion chamber PTW 31014 (PTW, Freiburg, Germany). The ion chamber has a cylindrical shape with vented sensitive volume of 0.015 cm^3 (2 mm in diameter and 4.8 mm in height). The wall material is graphite and the central electrode is made of Aluminum. Figure 3.3A shows the pinpoint ion chamber used in this project. Figure 3.3B is an image of the ion chamber taken using the kV imager of a TrueBeam linac.

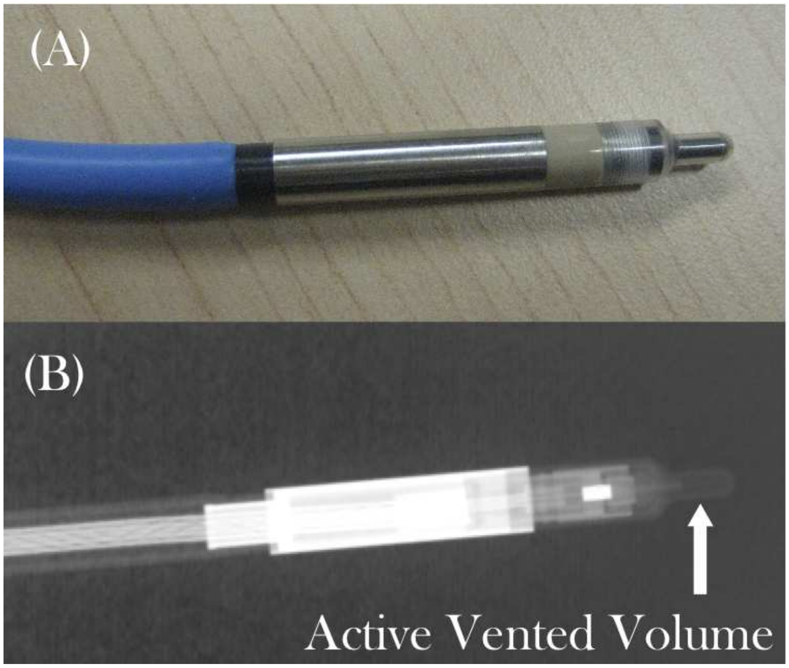

Figure 3.3: *(A)* Pinpoint ion chamber. *(B)* An image of the pinpoint ion chamber acquired with the kV imager.

3.1.4 Setup Design

At BCCA-VICC, the QA procedure of lung SABR VMAT treatments are carried out using the ArcCheck diode array (see section 2.3.4 for details). Although the characteristics and geometry of the ArcCheck diode array makes it an excellent QA device for treatment techniques such as IMRT, SABR, and VMAT, the static nature of ArcCheck does not allow for confirmation of whether the radiation was delivered in the correct part of the breathing cycle. A motion phantom capable of simulating human breathing traces is an ideal tool to ensure that the beam is turned on during the correct part of the breathing cycle. Such a device also allows for investigation of the effect of detector residual motion, which is inevitable in a gated treatment, on the dose measurements for intensity modulated techniques such as VMAT. In order to combine the capabilities of ArcCheck with the ability of the Quasar phantom to drive a detector based on real breathing patterns, we designed and constructed an interface that connects the translation stage of the Quasar phantom to a pinpoint ion chamber insert and drives the ion chamber within the cavity of the ArcCheck in the SI direction (see Figure 3.4). Figure 3.5 shows how the devices used in this setup are positioned with respect to the gantry.

This custom-made interface consists of an assembly that connects to the translation stage of the Quasar phantom. This assembly also holds a nylon thread rod, which connects to the pinpoint ion chamber insert and drives it with the same motion as that of the translation stage. In addition, a custom-made platform for the Quasar phantom allows the user to adjust the vertical and horizontal position of the phantom with respect to the ArcCheck. This setup allows us to assess the accuracy of the overall treatment delivery and ensure that the overall dose distribution is not adversely affected by beam interruptions *and* confirm that the beam is turned on during the correct portion of the breathing cycle.

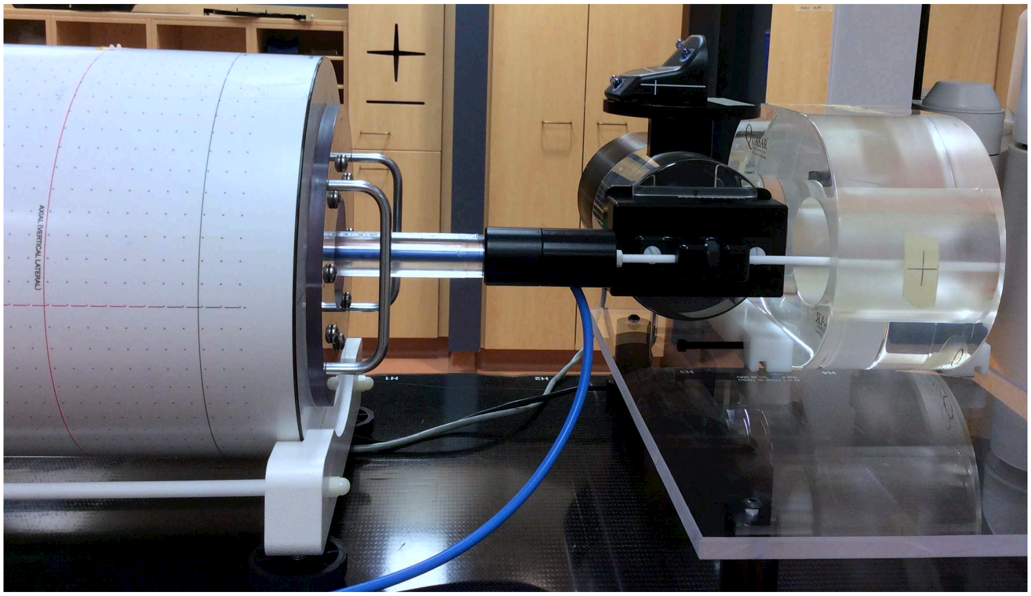

Figure 3.4: The translation stage of the phantom is connected to a pinpoint ion chamber insert and drives the insert within the cavity of the ArcCheck in the SI direction

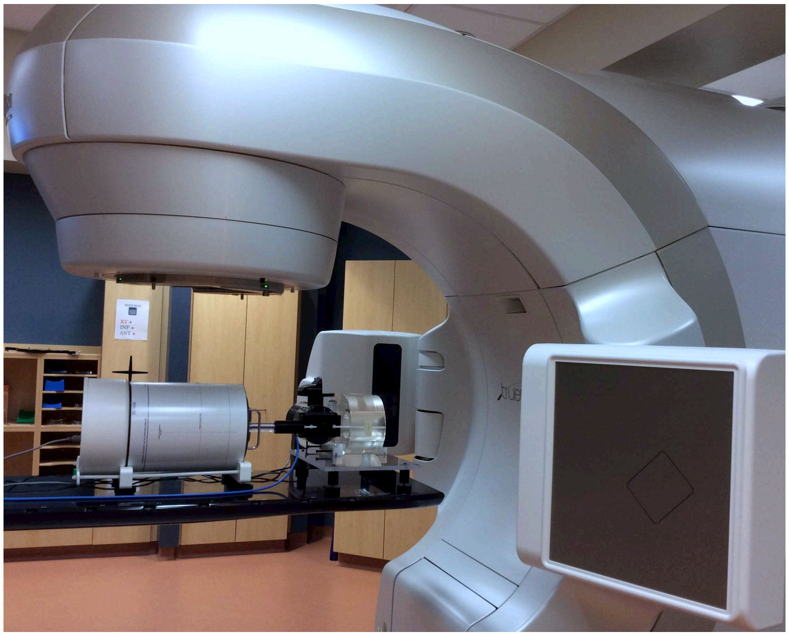

Figure 3.5: This figure shows how the entire setup is positioned with respect to the gantry

3.2 Method

3.2.1 Treatment Planning Using the Eclipse

The Eclipse treatment planning system was used to create three VMAT SABR liver treatments on the CT dataset of an anonymous patient according to the dose constraints described in the BCCA Provincial Protocol Guidelines for SABR treatments of HCC tumours. The prescribed dose was 4500 cGy in three fractions (i.e., 1500 cGy per fraction). The plans were created using two arcs between 180° and 60° gantry angles with collimator angles of 45° and 315°. The normalization was such that 100% of dose covers 95% of target volume. The Organs At Risk (OARs) include spinal canal, esophagus, heart, great vessels, lungs, skin, chest wall, stomach, duodenum, small bowel, large bowel, and kidneys. The dose constraints for OARs were achieved based on the provincial liver SABR protocol. The beam energy of 10 MV FFF and the option for "Gating" were chosen for the creation of these plans. The Eclipse Anisotropic Analytical Algorithm (AAA) was used for dose calculation. The verification plans were created on the artificial CT dataset of the ArcCheck. The slice width of this dataset is 2 mm. The dose to the pinpoint chamber was predicted by contouring cylindrical structures with volumes (0.0141 cm^3) comparable to that of the pinpoint chamber (0.015 cm^3). The diameter and width of the cylindrical structures are 6 mm and 1.9 mm, respectively.

The three created plans mainly differ in their PTV size, which are approximately 3 cm, 7 cm, and 12 cm in diameter (hereafter will be referred to as PTV1, PTV2, and PTV3). Figure 3.6 shows the Eclipse calculated dose profile along the Z axis (i.e., SI direction) for all three plans. The dose gradients in the penumbra are 961 cGy/cm, 1068 cGy/cm, 909 cGy/mm for PTV1, PTV2, and PTV3, respectively.

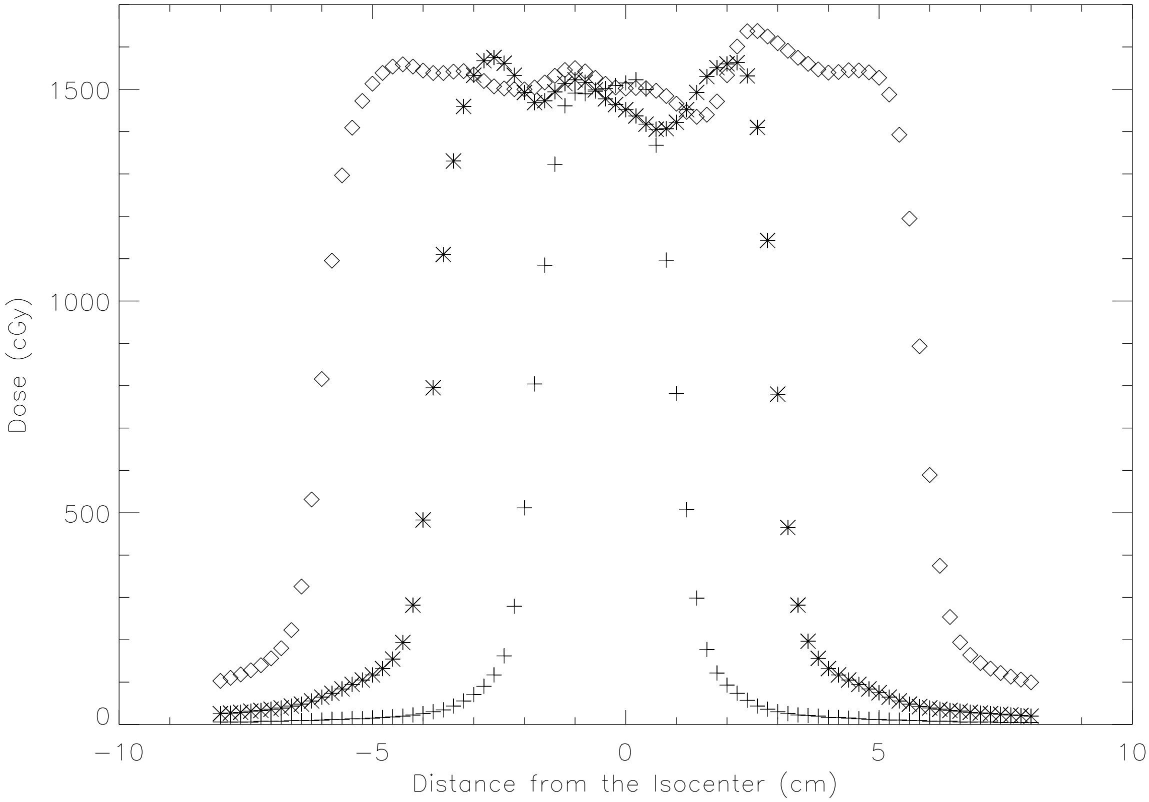

Figure 3.6: Eclipse calculated dose profile along the SI direction for all three plans.

3.2.2 Measurements: Pinpoint Ion Chamber

One of the main characteristics of SABR technique is the high dose gradient at the field edges. In this study, we are taking advantage of this characteristic to validate the ability of the RPM system to restrict the treatment delivery to the correct part of the breathing cycle. The dose measurement in the low dose gradient central region of a SABR plan is not sensitive to the positional accuracy of the detector (in this case the pinpoint ion chamber) during the beam-on time and therefore cannot confirm the accuracy of the gating system. Dose measurements in the penumbra region, however, are heavily dependent on the position of the detector when the radiation is being delivered and therefore are excellent probes of reliability of the gating system. The positional sensitivity of the dose measurements in the penumbra also offer us a chance to investigate the effect of detector residual motion within the gating window.

In order to fully understand the results of this study, it is important to describe our measurement setup in more detail. The black curve in both panels of Figure 3.7 shows the Eclipse calculated dose profile of the middle size PTV (diameter = 7 cm). Let us assume that the user intends to measure the dose at point A, which is in the middle of the penumbra region and has the maximum dose gradient. Our setup allows for the active volume of the pinpoint chamber to be at point A during the exhale portion of the breathing trace, when the beam is turned on. Once the breathing trace enters the inhale portion, the beam is turned off and the pinpoint chamber moves away from the measurement point (towards the lower dose regions).

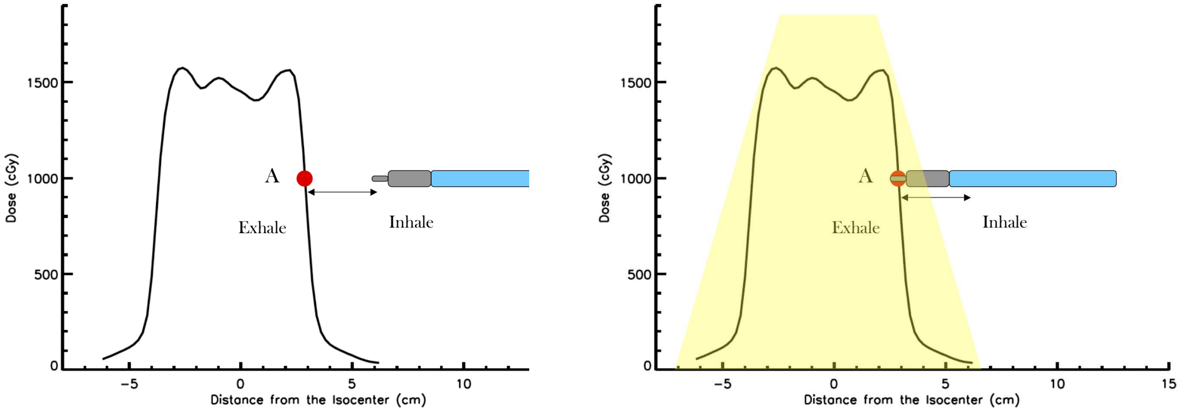

Figure 3.7: The black curve in both panels shows the Eclipse calculated dose profile of the middle size PTV (diameter = 7 cm). (*Left*) During the inhale the beam is off. (*Right*) Once the breathing trace enters the exhale portion, the beam comes on and the active volume of the pinpoint chamber reaches point A to measure the dose.

In this study, for each set of measurement, we have taken dose measurements at the isocentre and along the Z axis (central axis along the SI direction) in the penumbra region of each PTV. The location of the data points match the CT slices of the ArcCheck and therefore are 2 mm apart. It is important to note that to take the measurement for each data point along the penumbra, the treatment couch was moved towards the gantry with a shift equal to the distance of the point of interest from the isocenter on the Z axis (see Figure 3.6). Although our designed interface is capable of adjusting the position of the ion chamber insert, and therefore shifting the couch is not an absolute necessity, we decided that applying the couch shift is a more accurate and consistent method for acquiring our measurements.

For these measurements, the pinpoint ion chamber is first warmed up using a radiation delivery of 200 MU in a 10 cm × 10 cm field. Subsequently, the calibration factor for the pinpoint ion chamber measurements is determined by delivering 3000 MU in a 10 cm × 10 cm field using a full arc gantry rotation.

3.2.3 Measurements: ArcCheck Diode Array

In order to ensure that the overall dose accuracy is not degraded due to the beam interruptions of the gated delivery, we also obtained dose measurements using the ArcCheck diode array at the isocentre and in the middle of the penumbra. Subsequently, the measured and Eclipse calculated dose maps were compared utilizing the Gamma analysis feature on the SNC Patient software with 2mm/2% criteria.

3.3 Definitions

This section covers the definitions and calculation methods of some of the quantities that will be used in Chapters 4 and 5 to present the results of this study.

3.3.1 Duty Cycle

Duty cycle is an indication of the efficiency of the delivery method and is defined as the ratio of the beam-on time to the treatment time (Keall et al. 2006). It is important to note that the tumour (and the detector) still move within the gate. This motion is referred to as the “residual motion”. The balance between the amount of residual motion and duty cycle depends on the gate width.

Figure 3.8 shows an example of a synthesized breathing trace created using the Quasar software. The data points in Quasar data files (.QRM files) are evenly spaced in 10 ms increments. In order to calculate the duty cycle, the number of data points within the pre-designated amplitude gate (i.e., between lower and upper thresholds) are counted and divided by the total number of data points in the breathing trace.

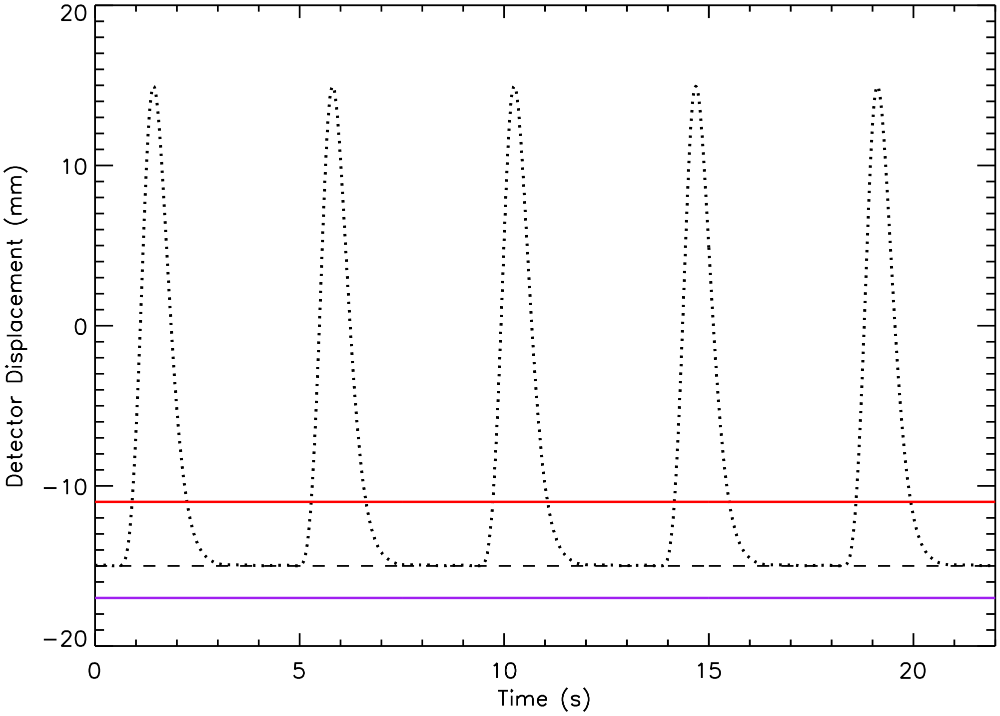

Figure 3.8: The dotted curve shows a synthesized breathing trace created using the Quasar software. The data points are in 10 ms increments. The dashed line shows the baseline. The lower and upper thresholds for amplitude gating are delineated with the purple and red solid lines, respectively.

3.3.2 Average Residual Detector Displacement (ARDD)

We define the ARDD as the average detector distance from the baseline of the breathing trace within the gate. This parameter is a measure of "dose-smearing" effect (described in section 3.4.1), especially for small gate widths, to estimate the expected dose delivered to the pinpoint ion chamber. To calculate the ARDD, we take the average of the positions of the ion chamber at the data points within the gate and find the distance between this average position and the baseline. Taking the breathing trace displayed in Figure 3.8 as an example, the ARDD is 0.436 mm. Such low value of ARDD shows that the detector spends a considerable amount of time near or at the baseline, which is confirmed by the relatively long exhale duration and the lack of baseline drift in this breathing trace.

3.4 Sources of Uncertainty in Dose Measurements Using Pinpoint Ion Chamber

3.4.1 Positional/Setup Uncertainty

In order to evaluate the uncertainty in setup and positioning of the pinpoint ion chamber, the entire setup was done ten times (on different days and on different linacs). To ensure that the active volume of the pinpoint ion chamber was properly aligned with the isocentre, the position of the isocentre in the Z direction was marked using two BB stickers on the outside surface of the ArcCheck. The position of the pinpoint ion chamber with respect to the BBs (and hence the isocentre) was measured by acquiring kV images of the region after the completion of each setup. The standard deviation of the location of the active volume of the pinpoint ion chamber in the Z direction was measured to be 0.5 mm. To evaluate the dose uncertainty due to setup errors, dose measurements of the isocentre and penumbra were taken for the middle size PTV. In all measurements, the treatment was delivered without gating and the pinpoint ion chamber was left stationary. Figure 3.9 shows the results of the ten sets of measurements. The average of the measured doses (i.e., blue diamonds) are in excellent agreement with the Eclipse calculated doses (i.e., black asterisks). The blue error bars show the standard deviation of the measured doses for each data point. As expected, the dose measurements in the lower dose gradient region of the dose profile is not significantly sensitive to positional uncertainty and therefore the corresponding error bars are smaller compared to those in the penumbra, where the error bars appear to be larger. Note that the error bars are only evaluated for PTV2, due to the lengthy nature of these measurements and the fact that most of the measurements in this study are taken using the treatment plan for PTV2.

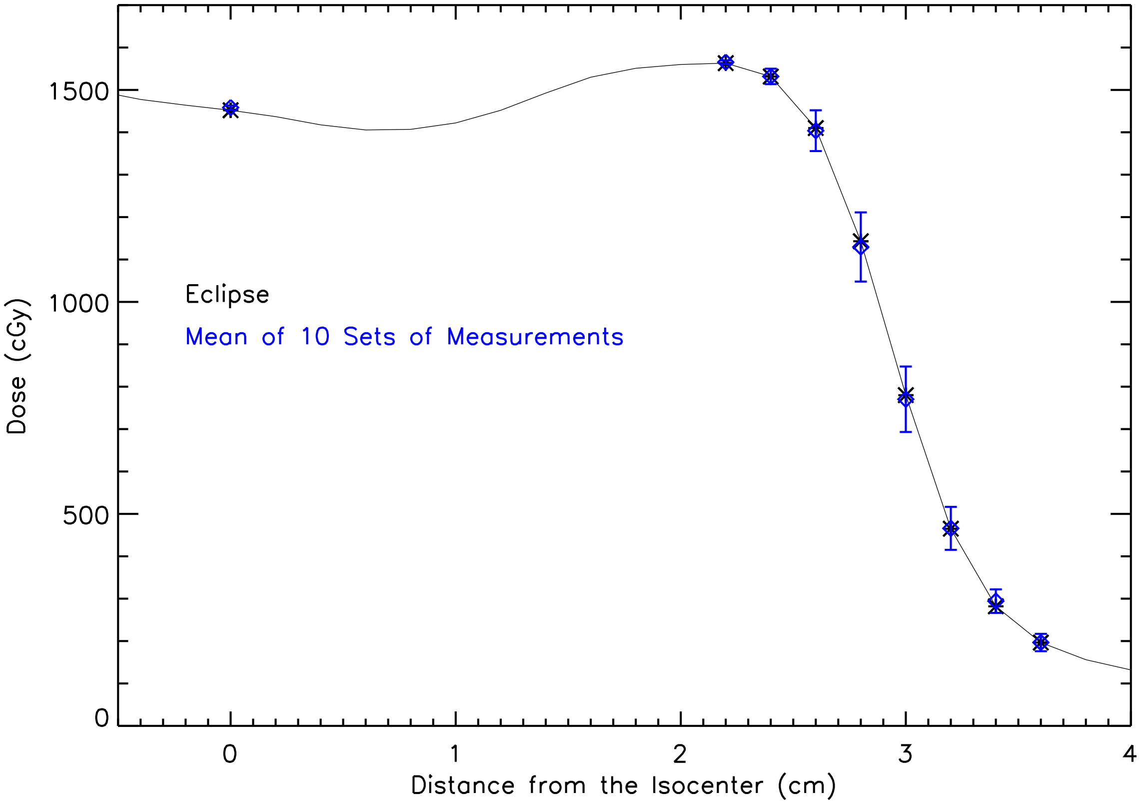

Figure 3.9: The black asterisks show Eclipse calculated doses at the locations where measurements were acquired (i.e., isocentre and penumbra) for the middle size PTV. The black solid curve shows the interpolation of all of the Eclipse calculated doses. The blue diamonds are the mean values of nine sets of measurements for each data point. Blue error bars show the standard deviation of the dose measurements at each data point.

3.4.2 Uncertainty Due to Beam Interruption

Gated treatments often involve multiple beam interruptions during the radiation delivery. To explore the effect of multiple beam interruptions on the overall dose fidelity, we measured the dose delivered to isocentre using the pinpoint ion chamber by delivering PTV2 treatment plan. The pinpoint ion chamber was left stationary inside the ArcCheck with the active volume at the isocentre. A motion phantom provided by Varian Medical Systems was used to generate a gating signal resembling a regular human breathing pattern with an amplitude of 16 mm and without any baseline drift. The measurements were taken with gating using various sizes of gate width (0.5 mm, 0.7 mm, 1 mm, 2 mm, 3 mm, 5 mm, and 7 mm with duty cycles of 27%, 30%, 33%, 39%, 47%, 50%, and 58% respectively) as well as without any gating. Note that for each specific gate width size, the dose measurement was acquired three times.

Although measurements varied slightly from each measurement to the next, the variation was not significant and no specific trends were detected. The Eclipse calculated dose at isocentre for PTV2 is equal to 1452 cGy. We measured the dose delivered to the pinpoint ion chamber without any gating to be 1462 cGy (% Difference = 0.7%). Under gating conditions, the average dose delivered to pinpoint ion chamber was 1462 cGy with a standard deviation of 2 cGy. These results demonstrate that beam interruptions are not a significant source of uncertainty in the amount of dose delivered to the target.

To further demonstrate that the overall dose accuracy is not adversely affected by beam interruptions, we have also monitored the dose delivered to the ArcCheck diode array for each of the measurement sets presented in Chapters 4 and 5 of this manuscript. The ArcCheck diode array measurements are taken both when our setup is centred at isocentre and at the middle of the penumbra. Subsequently, the measurement maps were compared to Eclipse calculated dose maps using Gamma analysis with 2mm/2% criteria using diodes with measured doses higher than 10% and 40% of the maximum dose. The results of the Gamma pass rates are reported in Chapters 4 and 5 for each set of measurement.

3.4.3 Uncertainty Due to Intra-Fractional Motion

Intra-fractional organ (or detector) motion can result in two types of dosimetric effects (Ceberg et al. 2013): The first one is referred to as the dose-blurring effect, where the dose delivered to a point in patient's body (or detector) is smeared as a result of the motion of this point in the radiation field. The second one is referred to as the interplay effect, where the relative motion between the MLC leaves and the treatment region may lead to a more complicated dosimetric effect and may cause hot and cold spots inside or outside of the target (Berbeco et al. 2006).

The dose-blurring effect depends on the amplitude of the intra-fractional motion (i.e., the respiration amplitude or the gate width for a gated delivery) and the degree of intensity modulation. Blurring always results in dose-reduction to the penumbra region (Kang et al. 2010). The Interplay effect also increases with intra-fractional motion amplitude, and depends on the breathing phase at the start of each beam on and the breathing period (Kang et al. 2010). In addition, the dose variation due to target intra-fractional motion increases with dose rate (Jiang et al. 2003). This is because at higher dose rates, the MLC leaf speed approaches the tumour speed, resulting in an increase in the dose variation.

The delivered dose distribution depends mostly on the dose-blurring with statistical variation as a result of the interplay effect. Previous studies (e.g., see Bortfeld et al. 2002; Chui et al. 2003; Jiang et al. 2003) suggest that the interplay effect reduces in treatments with number of fractions higher than ten. For instance, Jiang et al. (2003) investigated the influence of interplay effect in conventional 5-field lung IMRT treatments and found up to 18% dose variation for a single fraction. The dose, variation, however, reduced to 1%−2% after 30 fractions. Kang et al. (2010) explored the effect of interplay on hypo-fractionated IMRT plans (20 Gy per 3 fractions) using numerical simulations for a maximum amplitude of 1.26 cm and found minimal changes in target coverage but suggested that the effect can be more pronounced for larger motion amplitude or faster radiation delivery, higher levels of intensity modulation, and smaller field margins. Li et al. (2013) investigated the interplay effect in VMAT lung SABR treatments delivered using 6 MV beam in FFF mode. The results suggest that a considerable reduction occurs in the PTV coverage, especially with increased motion amplitude. However, the coverage (V100 and D90) of the GTV and GTV + 5mm remain unchanged or increase up to 1.2%. Therefore, Li et al. (2013) came to the conclusion that with suitable choice of margin, interplay effect does not introduce considerable dose variation in VMAT SABR treatments using FFF beams.

3.4.4 Time Delay in Beam On/Off

Another type of inaccuracy arising in gated treatments is due to time delays in turning the beam on when the surrogate marker (e.g., the RPM block in this project) enters the gate window *and* in turning the beam off when the marker leaves the gate window. Several groups have measured the time delays corresponding to various gating systems and imaging/therapy devices. It is important to note that there are two components contributing to the beam latency: the gating system predictive filter and the linac or imaging device beam delay. Therefore, it is possible that different linacs using the same gating system might have different beam latencies (Smith and Becker (2009)).

Jin and Yin (2005) measured the time delay of the BrainLAB Gating system (Heimstetten, Germany) on a Novalis radiosurgery unit (BrainLAB, Heimstetten, Germany) to be 170 ± 30 ms using a motion phantom with sinusoidal trace. Tenn et al. (2005) also used the BrainLAB Gating and found a time delay of 60 ± 20 ms. For the Calypso system (described in section 2.1.5) and Varian Trilogy linac, Smith et al. (2009) measured beam delays of 75.0 ± 12.7 ms and 65.1 ± 12.9 ms for beam on and beam off, respectively. Smith and Becker (2009) measured the time delays for the RPM gating system on three fluoroscopy systems and three linacs using regular higher order sinusoidal functions as the breathing trace. For amplitude gating, they found the beam on and beam off of the fluoroscopy systems to be early by 40 ± 50 ms and 180 ± 80, respectively. For phase gating, the beam on and beam off were early by 110 ± 40 ms and 150 ± 40 ms, respectively. For linacs, the beam on and beam off were late by 90 ± 20 ms and 80 ± 20 ms for amplitude gating, respectively. For treatment deliveries using phase gating the beam on and off delay times were measured to be 100 ± 30 ms and 70 ± 20 ms, respectively. Guana (2006) measured the scanning delay of 750 ms for RPM gated axial 4DCT using AcQSim CT scanner (Philips Medical Systems, Cleveland, OH). The scanning delay consists of half of the scan time (1 s in this case) in addition to the CT triggering delay, which is equal to 250 ms. Goharian and Khan (2010) measured the beam latency of the Philips Brilliance BigBore (Philips Medical Systems, Madison, WI) CT scanner that is used in conjunction with the RPM gating system to be 367 ± 40 ms using regular breathing patterns. Chugh et al. (2014) measured the beam delays of RPM gated treatments delivered using TrueBeam linac using sinusoidal and realistic breathing traces by comparing the expected and measured lengths of film streaks of radiation exposure. They found the sinusoidal traces, regular realistic traces, and traces with slightly irregular amplitude variations result in beam latency less than 100 ms. Small variations in the breathing trace period, however, can result in beam delay larger than 1 s, if used in conjunction with phase gating.

We have explored the effect of time delay in our measurements. The results are presented in section 5.3.

Chapter 4

Results and Discussion: Gated Dose Measurements Using Synthesized Breathing Traces

This chapter presents the results of our measurements using the synthesized breathing patterns created with the Quasar software. Our goal is to investigate how PTV size, duration of exhale, baseline drift, and gate width influence gated treatments. Therefore, we have measured the dose at isocentre and along the penumbra while introducing systematic changes to the four mentioned parameters. The results of these measurements are presented and discussed below.

4.1 PTV Size

As explained in section 3.2.1, we created three treatment plans for three PTVs that are 3 cm, 7 cm, and 12 cm in diameter. The Eclipse calculated dose profiles of all three plans along the SI direction is shown in Figure 3.6.

Our measurements were taken using the synthetic breathing pattern shown in Figure 4.1 with an upper threshold of 4 mm, which corresponds to ARDD of 0.436 mm and duty cycle of 70%. Figure 4.2 shows the results of our measurements, focusing only on the isocentre and penumbra region of each plan. The error bars corresponding to PTV1 and PTV3 measurements are determined by interpolating Eclipse calculated doses and assuming 2σ setup uncertainty of (= ±1 mm; see section 3.4.1 for details). The error bars corresponding to PTV2 measurements are determined directly by repeating the measurement of the dose delivered to the pinpoint ion chamber at the isocentre and along the penumbra ten different times and again assuming 2σ uncertainty (see section 3.4.1 for details). For each plan, our measurements are well within the setup uncertainties and in excellent agreement with Eclipse calculated doses. As expected, our results demonstrate that the quality of an amplitude gated treatment does not depend on the size of the PTV. In addition, the measurements confirm that dose variations due to the dose-blurring and interplay effects are not significant when gate width and ARDD are small.

To ensure that beam interruptions during gated treatments are not degrading the overall dose distribution accuracy of the treatments, The ArcCheck diode measurements were monitored with the ArcCheck centred at isocentre and in the middle of the penumbra region. Subsequently, the measured dose maps were compared with Eclipse calculated dose maps using Gamma analysis with 2mm/2% criteria. Our Gamma analysis was limited to diodes with measured doses higher than 10% and 40% of the maximum dose. Tables 4.1 and 4.2 show the Gamma pass rates when the treatment plans were delivered without and with gating. Although some variation is seen in the Gamma pass rates for different PTV sizes and for deliveries with and without gating, the pass rates are well above 90% in all cases and no specific trends are detected.

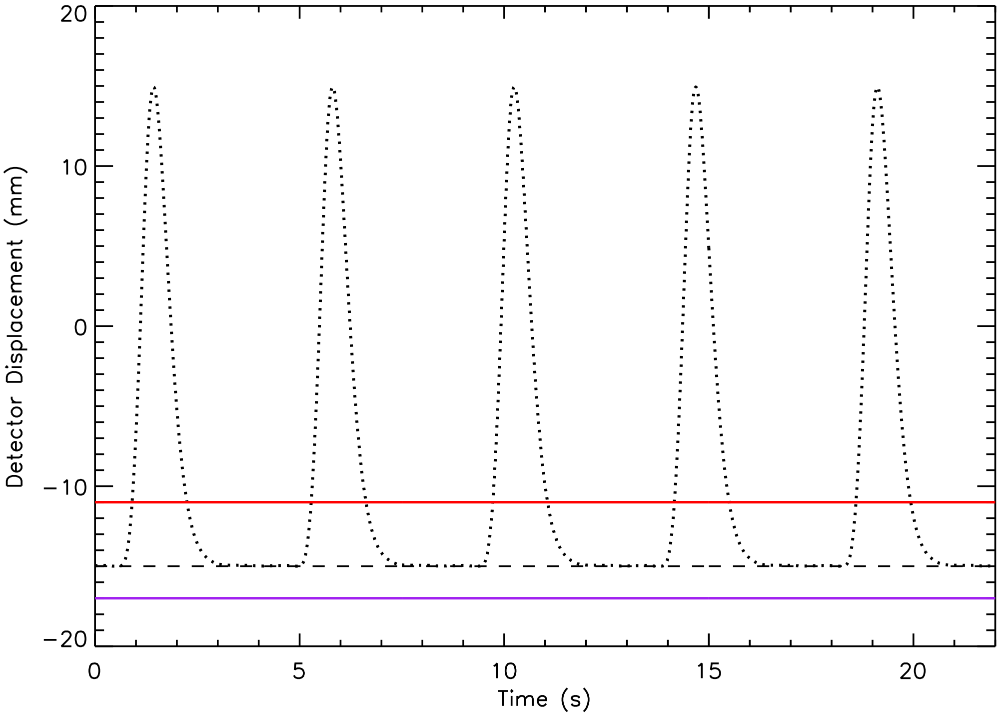

Figure 4.1: The dotted curve shows the synthesized breathing trace that was used to obtain the measurements for three different PTV sizes (see Figure 4.2). The data points are in 10 ms increments. The dashed line shows the baseline. The lower and upper thresholds for amplitude gating are delineated with the purple and red solid lines, respectively. Note that the breathing trace is inverted with respect to the direction displayed on the Quasar software.

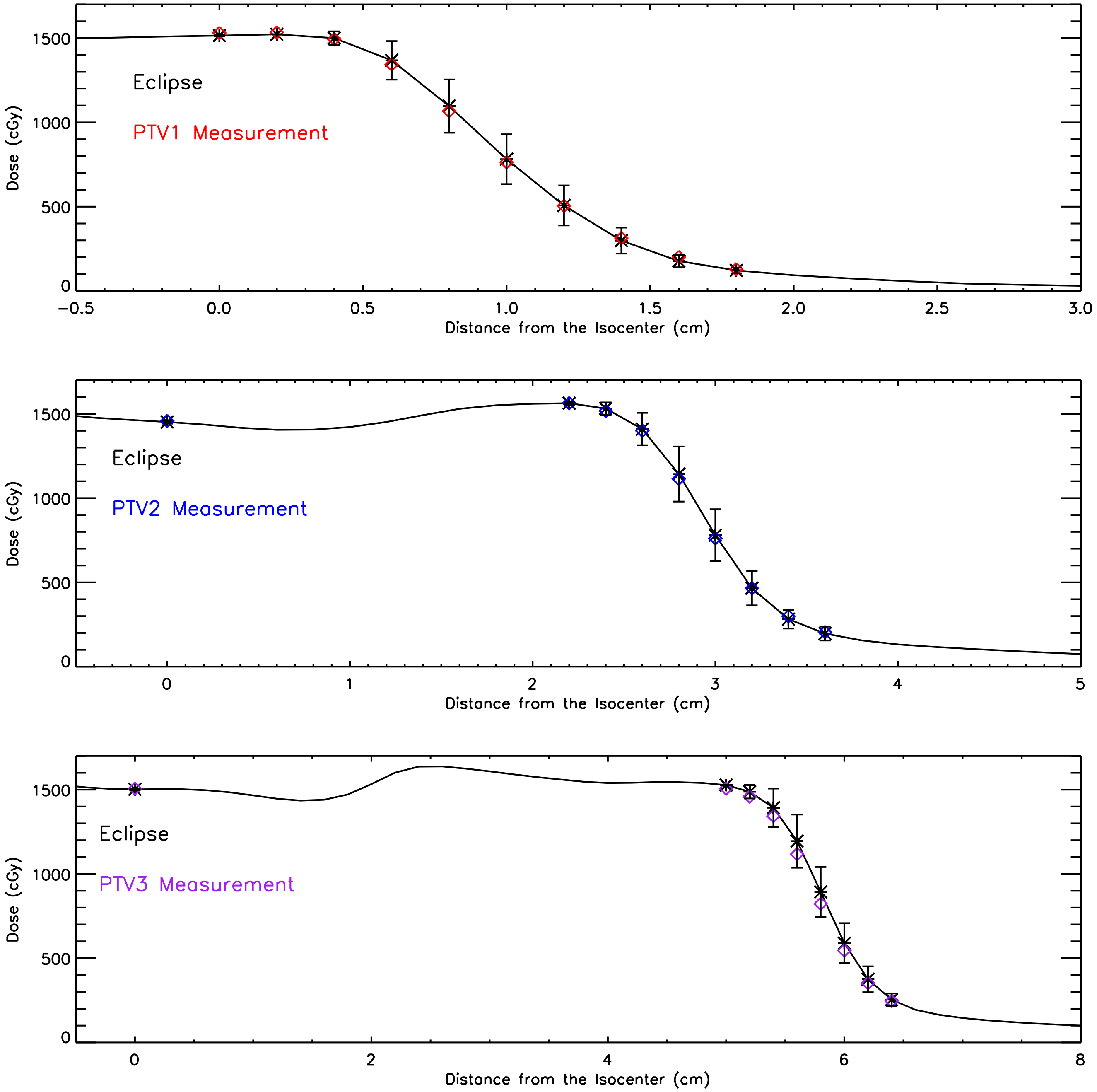

Figure 4.2: For each plan, the black asterisks show Eclipse calculated doses at the locations, where measurements were acquired (i.e., isocentre and penumbra). The black solid curve shows the interpolation of all of the Eclipse calculated doses. The red, blue, and purple diamonds show the pinpoint ion chamber dose measurements using the synthesized breathing trace in Figure 4.1. Note that the horizontal axis scale is different for each plot.

Table 4.1: Gamma pass rates (2mm/2%) for ArcCheck measurements without gating for three PTV sizes at isocentre and in the middle of penumbra.

	Isocentre		Penumbra	
Plan	10% Threshold	40% Threshold	10% Threshold	40% Threshold
PTV1	96.7%	94%	96.5%	94%
PTV2	98.1%	96.7%	97.7%	95.8%
PTV3	99.1%	98.7%	95.1%	93.8%

Table 4.2: Gamma pass rates (2mm/2%) for ArcCheck measurements with gating for three PTV sizes at isocentre and in the middle of penumbra.

	Isocentre		Penumbra	
Plan	10% Threshold	40% Threshold	10% Threshold	40% Threshold
PTV1	97.2%	94.8%	97.4%	95.7%
PTV2	98.1%	96.7%	97.7%	95.8%
PTV3	99.1%	98.7%	95.8%	94.7%

4.2 Duration of Exhale

As mentioned in section 2.1.4, for this project, we have restricted the treatment delivery to the exhale, which is the most stable part of the breathing cycle. To explore how increasing the duration of exhale influences the fidelity of a gated treatment, four synthetic breathing traces were created using the Quasar software. All four traces are similar in shape to the trace shown in Figure 4.1. Their exhale durations, however, were increased from 2 s, to 3 s, 4 s, and 5 s (see Figure 4.3). An upper threshold of 2 mm was used for all measurements in this section. The duty cycle and ARDD for each trace is listed in Table 4.3. The treatment plan for PTV2 was delivered using the described traces. The pinpoint ion chamber measurements are displayed in Figure 4.4.

It is evident from Table 4.3 that for a constant gate width, the ARDD decreases with increasing exhale duration, as the detector is spending more and more time at the baseline during the exhale. In all four cases, however, the ARDD and gate width are relatively small and therefore we do not expect to see a significant change in dose measurements due to dose-blurring and interplay effect. This is indeed confirmed by the results displayed in Figure 4.4. It should also be noted that by increasing the exhale duration, our method of delivery is approaching the static case, where dose-blurring and interplay effects no longer exist.

Table 4.4 shows the Gamma pass rates of the ArcCheck measurements corresponding to the measurements described in this section. Comparing these results with the pass rates listed in Table 4.1 for PTV2 shows that changing the duration of exhale in gated treatments (and therefore changing the number of beam interruptions) does not reduce the accuracy of overall dose distribution delivered by the treatment.

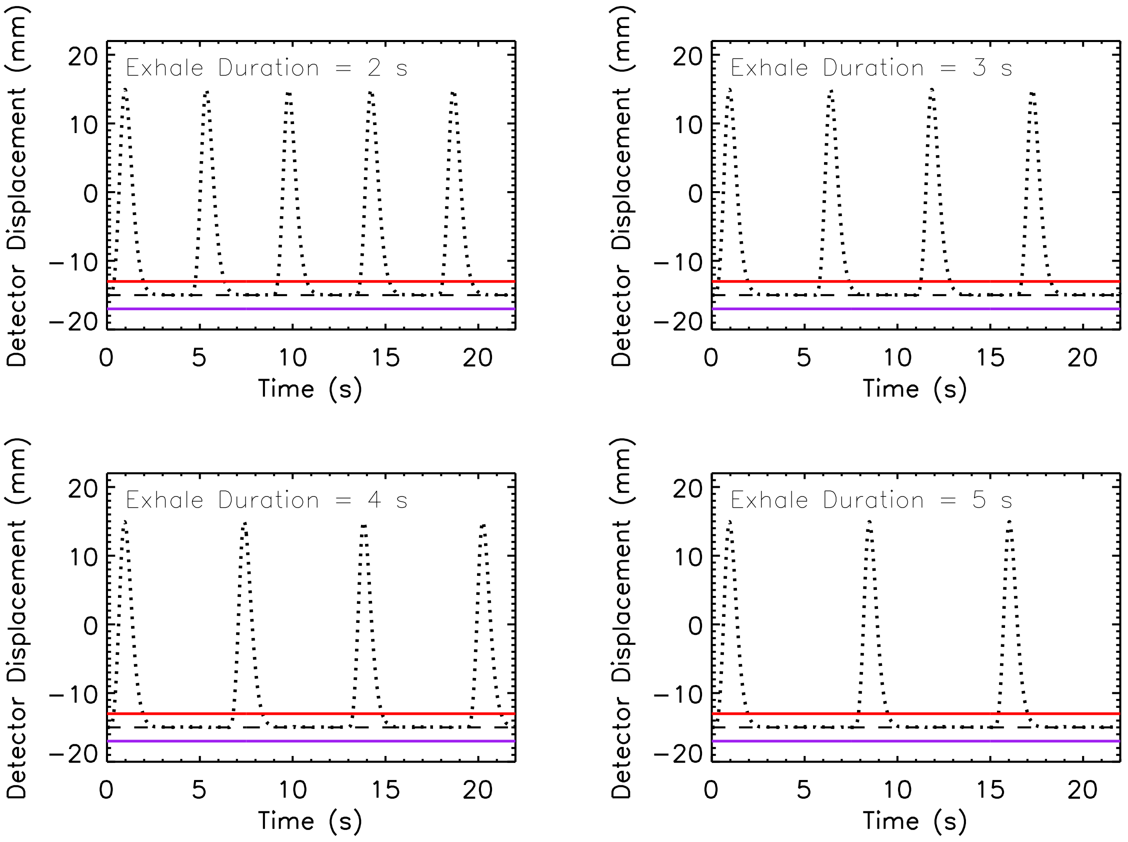

Figure 4.3: In all four plots, the dotted curves show the synthesized breathing traces that were used to obtain the measurements shown in Figure 4.4. The duration of exhale varies from 2 s to 3 s, 4 s, and 5 s. The data points are in 10 ms increments. The dashed line shows the baseline. The lower and upper thresholds for amplitude gating are delineated with the purple and red solid lines, respectively.

Table 4.3: Duty cycles & ARDD for synthesized breathing traces.

Exhale Duration (s)	Upper Threshold (mm)	ARDD (mm)	Duty Cycle
2	2	0.2246	64%
3	2	0.1831	71%
4	2	0.1568	76%
5	2	0.1377	79%

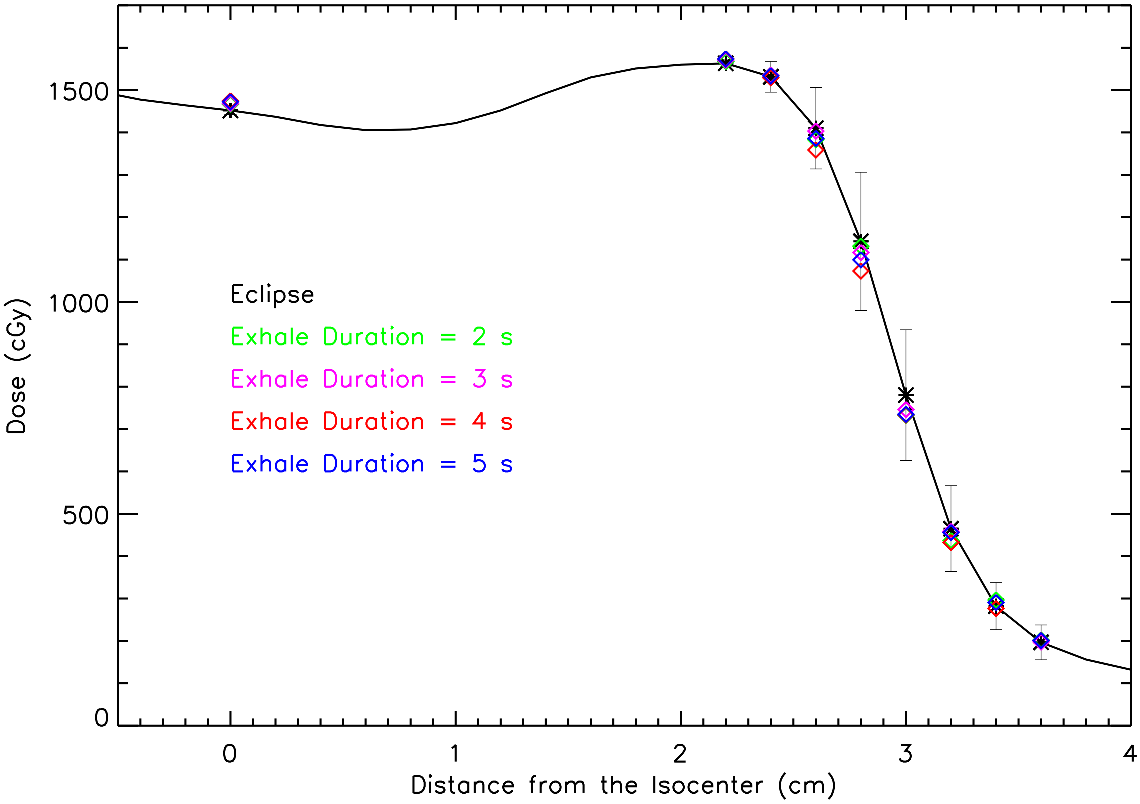

Figure 4.4: The black asterisks show Eclipse calculated doses at the locations where measurements were acquired (i.e., isocentre and penumbra) for PTV2. The black solid curve shows the interpolation of all of the Eclipse calculated doses. The green, pink, red, and blue diamonds show the pinpoint ion chamber dose measurements using the synthesized breathing traces in Figure 4.3. The error bars correspond to 2σ setup uncertainty (see section 3.4.1).

Table 4.4: Gamma pass rates (2mm/2%) for ArcCheck measurements of PTV2 with gating at isocentre and in the middle of penumbra using various durations of exhale.

	Isocentre		Penumbra	
Exhale Duration (s)	10% Threshold	40% Threshold	10% Threshold	40% Threshold
2	99.6%	99.2%	99.2%	98.3%
3	99.6%	99.2%	99.2%	98.3%
4	99.6%	99.2%	99.4%	98.7%
5	99.6%	99.6%	99.2%	98.3%

4.3 Gate Width

To investigate how increasing the gate width affects the dose delivered to a moving ion chamber, we used a sinusoidal breathing trace (period = 4 s and peak-to-peak amplitude = 40 mm) to deliver the treatment plan PTV2 with amplitude gating. Upper thresholds of 2 mm, 4 mm, 8 mm, 12 mm, 16 mm, and 20 mm were utilized in these measurements (see Figure 4.5). Note that all gate widths mentioned in this study correspond to the movement of the detector, and the gate widths utilized at the linac console for the RPM reflector block were chosen appropriately to achieve the correct gate limits for the detector. The corresponding data for ARDD and duty cycles are listed in Table 4.5. Figure 4.6 shows the results of dose measurements using the pinpoint ion chamber. As the size of the gate window is increased, the detector spends more and more time in lower dose regions. Thus, we expect to measure lower doses for larger gate windows. This is indeed the dose-blurring effect described in section 3.4.3. This is in agreement with the results displayed in Figure 4.6. In fact, the ARDD is the key parameter in estimating the dose delivered to the pinpoint ion chamber when the dose-blurring effect is taken into account. Figure 4.7 shows the dose measurements for each gate width. For this plot, however, the dose measurements are shifted to the right (toward the lower dose regions) by the ARDD to reflect the dose-smearing effect. The dashed curves show the 95% confidence interval (This is achieved using 2σ positional uncertainty = ±1 mm). It is evident that the measurements obtained using upper thresholds of 2 mm and 4 mm are in excellent agreement with the Eclipse calculated doses, when the ARDD is taken into account. As the gate window sizes increases, however, the measured doses start to deviate from the Eclipse predictions and fall outside of the 95% confidence interval. As explained in section 3.4.3, by increasing the size of the gate width the amplitude of the residual motion within the gate may increase, which can lead to higher levels of interplay effect. Therefore, in such cases accounting for the beam-smearing effect is no longer enough to achieve good agreement between the measured doses and the Eclipse predictions.

Table 4.6 shows the Gamma pass rates for ArcCheck measurements. It is clear that the overall dose distribution is not affected by the changes in the gate width.

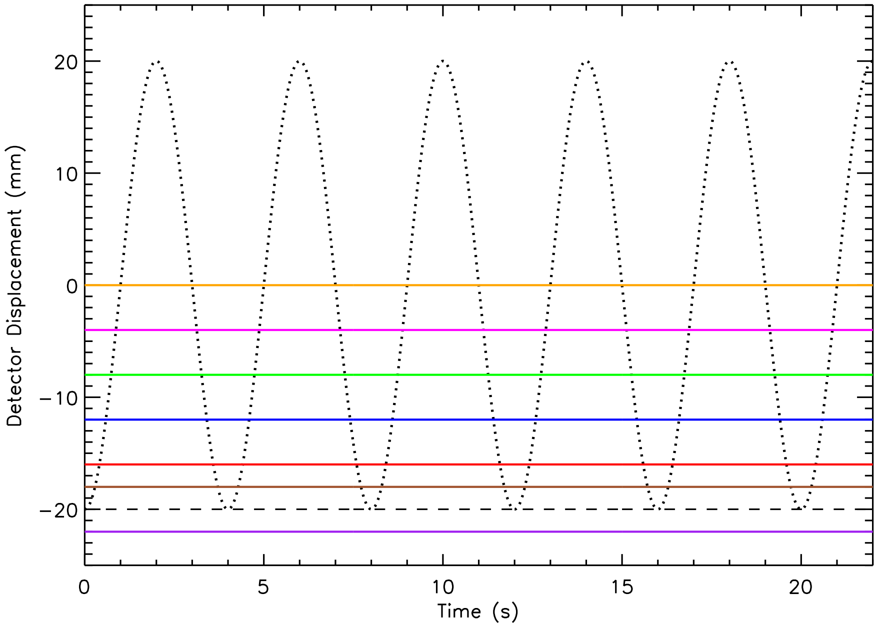

Figure 4.5: The dotted curve shows the sinusoidal breathing trace that was used to obtain the measurements shown in Figure 4.6. The data points are in 10 ms increments. The dashed line shows the baseline. The lower threshold for amplitude gating is delineated with the purple solid line. The size of gate window was increased from 2 s to 4 s, 8 s, 12 s, 16 s, and 20 s. The corresponding upper threshold is shown using brown, red, blue, green, pink, and orange solid lines, respectively.

Table 4.5: Duty cycle & ARDD for sinusoidal breathing trace for different gate window sizes.

Upper Threshold (mm)	ARDD (mm)	Duty Cycle
2	0.6610	14%
4	1.3216	20%
8	2.7866	30%
12	4.1556	37%
16	5.7276	44%
20	7.2662	50%

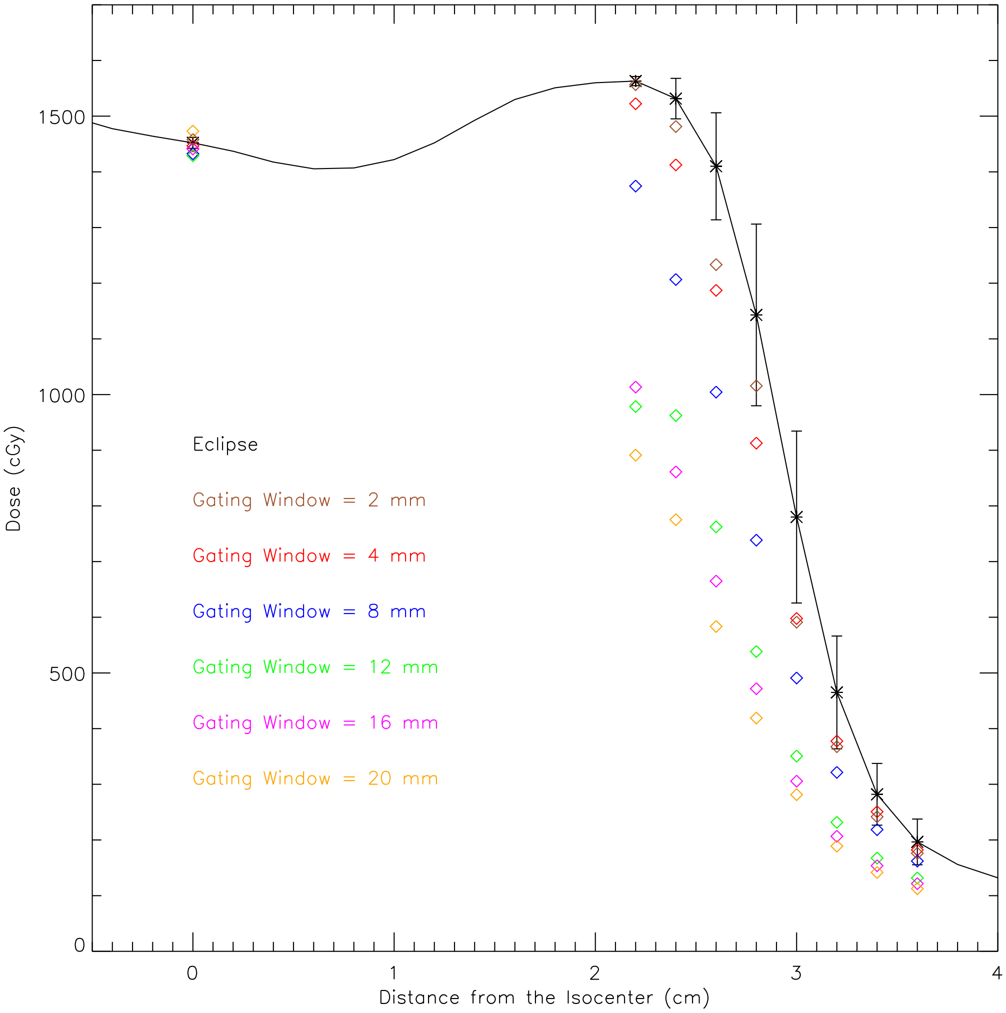

Figure 4.6: The black asterisks show Eclipse calculated doses at the locations, where measurements were acquired (i.e., isocentre and penumbra) for PTV2. The black solid curve shows the interpolation of all of the Eclipse calculated doses. The coloured diamonds show the pinpoint ion chamber dose measurements using the sinusoidal breathing trace and different gate window sizes. The error bars correspond to 2σ setup uncertainty (see section 3.4.1).

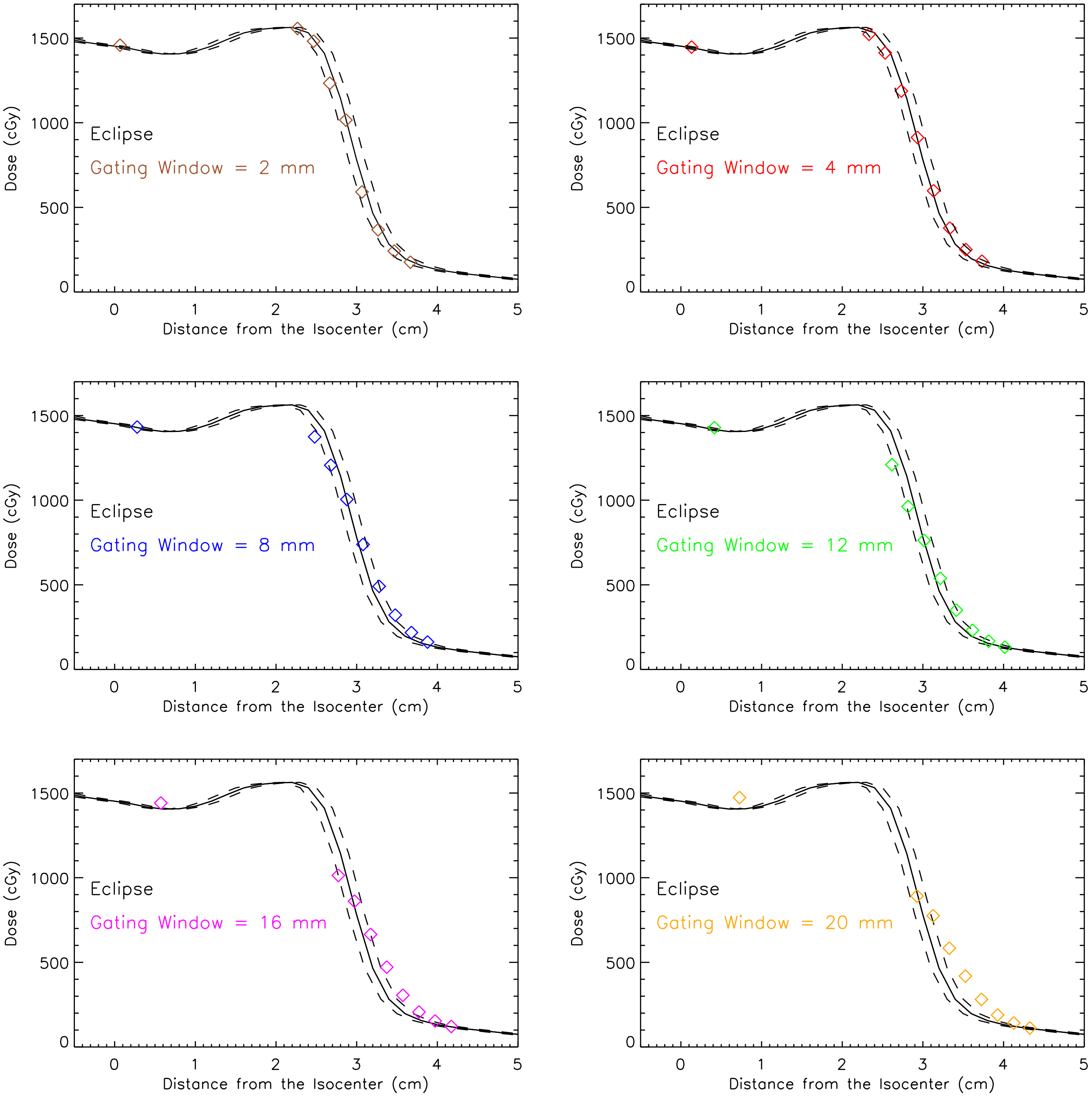

Figure 4.7: In each plot, the black solid curve shows the interpolation of all of the Eclipse calculated doses. The dashed curves show the 95% confidence interval. The coloured diamonds show the pinpoint ion chamber dose measurements using the sinusoidal breathing trace and different gate window sizes. Note that in this plot the dose measurements are shifted by the corresponding ARDD values.

Table 4.6: Gamma pass rates (2mm/2%) for ArcCheck measurements of PTV2 with gating at isocentre and in the middle of penumbra using various gate widths.

	Isocentre		Penumbra	
Upper Threshold (mm)	10% Threshold	40% Threshold	10% Threshold	40% Threshold
2	99.0%	99.2%	99.0%	97.9%
4	99.0%	99.2%	98.8%	97.5%
8	99.0%	98.3%	98.1%	96.7%
12	99.6%	99.2%	97.7%	95.8%
16	99.0%	98.3%	97.3%	95%
20	98.3%	98.7%	97.7%	95.8%

4.4 Baseline Drift

Baseline drift is usually present in real breathing patterns. Therefore, it is important to explore the effect of baseline drift on dose measurements for gated treatments. The Quasar software was used to create synthesized breathing patterns with four levels of gradual baseline drift (2 mm, 4 mm, 8 mm, 12 mm; see Figure 4.8). The gating upper threshold was maintained at 12 mm throughout these measurements. Table 4.7 lists the corresponding ARDD and duty cycle values. The resulting dose measurements are shown in Figure 4.9. As the level of baseline drift increases, the detector is spending more and more time away from the baseline, resulting in higher values of ARDD, which leads to lower doses delivered to the ion chamber. This is indeed in agreement with the results displayed in Figure 4.9. Following the same method mentioned in section 4.3, Figure 4.10 shows the shifted pinpoint ion chamber dose measurements for various levels of baseline drift. For all four levels of baseline drift, most of the measured data points are within the 95% confidence interval from the Eclipse calculated dose profile.

Table 4.8 reports the Gamma pass rates for ArcCheck dose measurements of gated deliveries of PTV2 using the breathing traces shown in Figure 4.8. It is evident that the beam interruptions involved in these radiation deliveries have not adversely affected the overall dose distribution delivered to ArcCheck diodes.

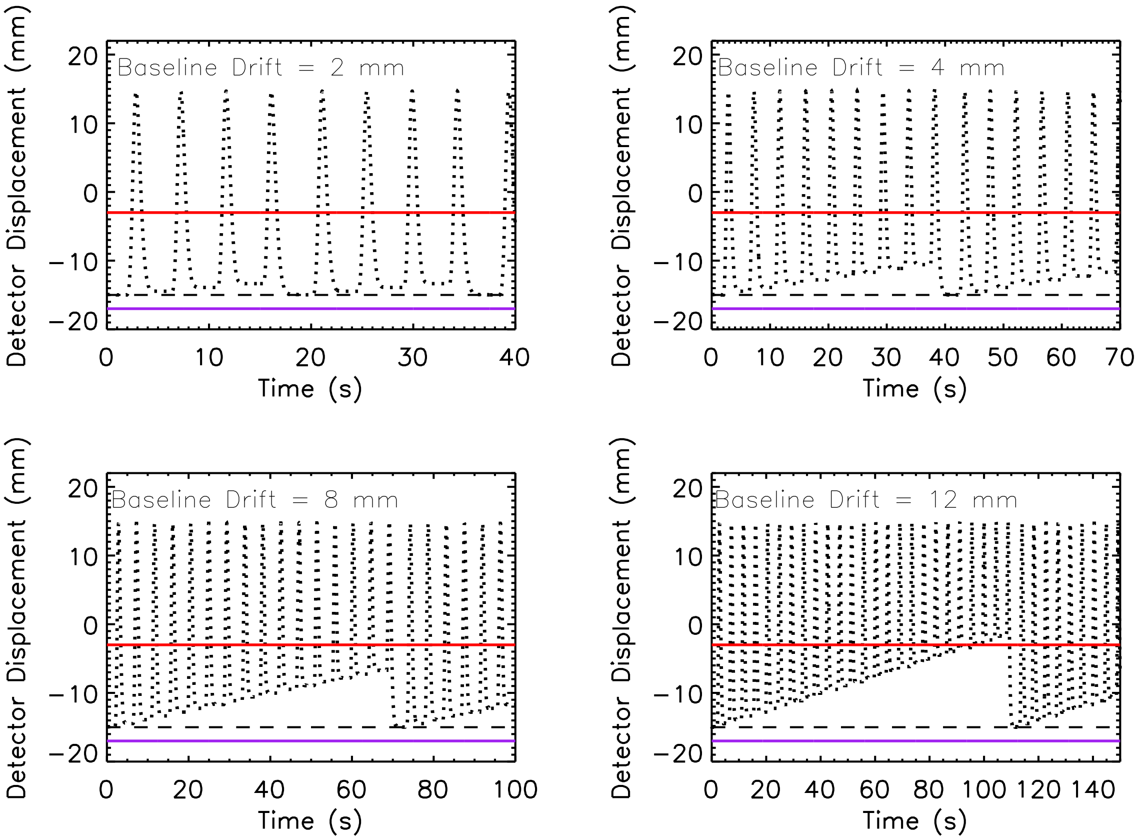

Figure 4.8: In each plot, the dotted curve shows the synthesized breathing trace that was used to obtain the measurements shown in Figure 4.9. The data points are in 10 ms increments. The lower and upper thresholds for amplitude gating are delineated with the purple and red solid lines, respectively.

Table 4.7: Duty cycle & ARDD for breathing traces with baseline drift.

Baseline Drift (mm)	Upper Threshold (mm)	ARDD (mm)	Duty Cycle
2	12	2.0145	78%
4	12	3.211	78%
8	12	4.7610	78%
12	12	6.2019	68%

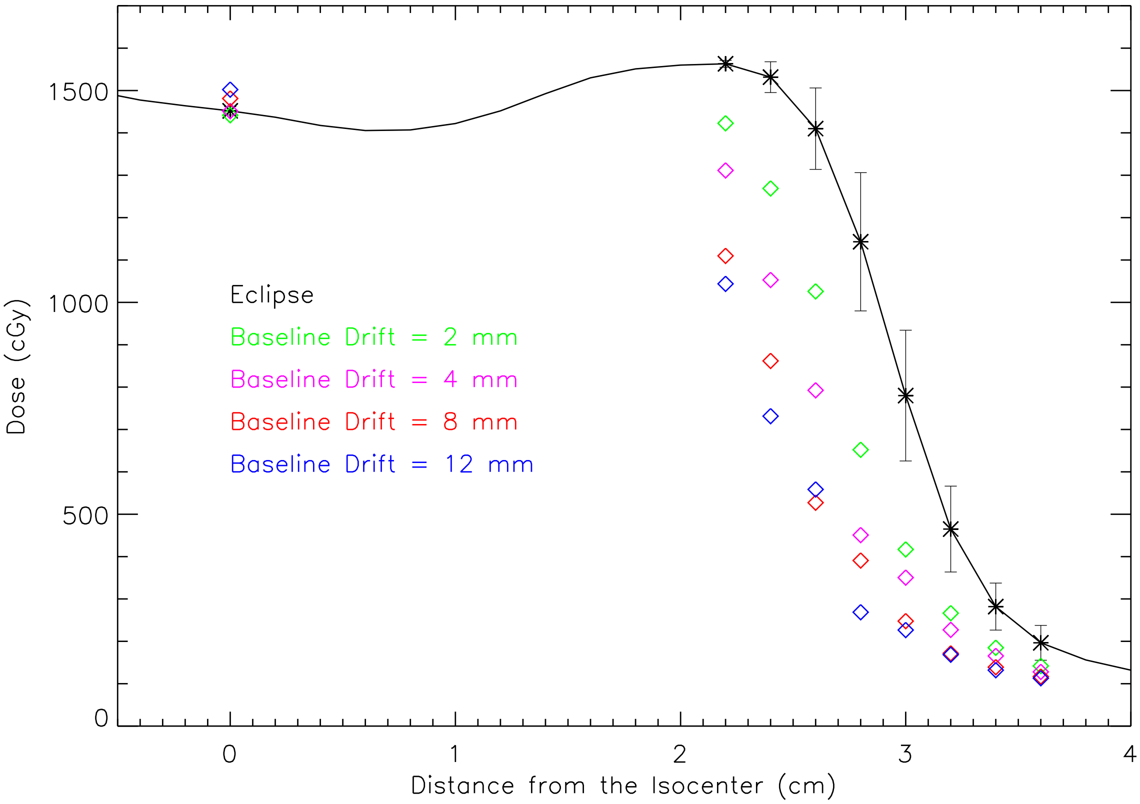

Figure 4.9: The black asterisks show Eclipse calculated doses at the locations where measurements were acquired (i.e., isocentre and penumbra) for PTV2. The black solid curve shows the interpolation of all of the Eclipse calculated doses. The coloured diamonds show the pinpoint ion chamber dose measurements using the breathing traces with various levels of baseline drift. The error bars correspond to 2σ setup uncertainty (see section 3.4.1).

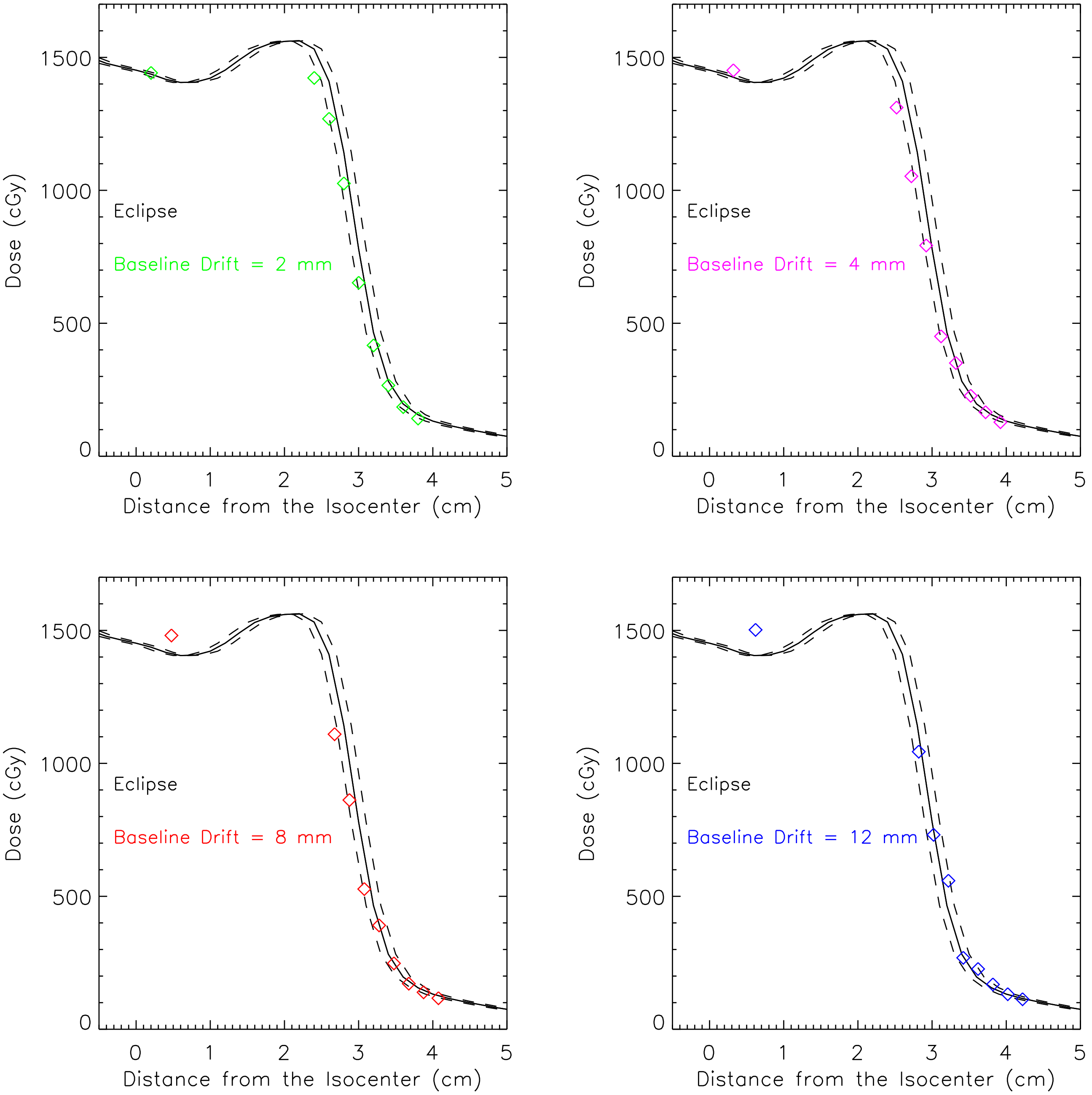

Figure 4.10: In each plot, the black solid curve shows the interpolation of all of the Eclipse calculated doses. The dashed curves show the 95% confidence interval. The coloured diamonds show the pinpoint ion chamber dose measurements using the breathing traces with various levels of baseline drift. Note that in this plot the dose measurements are shifted by the corresponding ARDD values.

Table 4.8: Gamma pass rates (2mm/2%) for ArcCheck measurements of PTV2 with gating at isocentre and in the middle of penumbra using various degrees of baseline drift.

	Isocentre		Penumbra	
Baseline Drift (mm)	10% Threshold	40% Threshold	10% Threshold	40% Threshold
2	99.2%	98.3%	97.1%	95.4%
4	99.2%	98.3%	97.9%	96.2%
8	99%	97.9%	97.3%	95%
12	99.8%	99.6%	99%	97.9%

4.5 Discussion & Conclusion

Previous studies performed on respiratory gating have mostly made use of either purely sinusoidal and higher order sinusoidal breathing patterns (see e.g., Jin and Yin 2005; Smith and Becker 2009) or real breathing traces (see e.g., Viel et al. 2015). These types of traces do not allow the user to introduce systematic changes to a certain feature in the breathing pattern, independent of other quantities. This study presents dosimetric results of gated treatments when systematic changes are introduced to the following key parameters individually: PTV size, exhale duration, gate width, and baseline drift.

Our results demonstrate that this setup can be used to take dosimetric measurements for PTV sizes up to 12 cm in diameter without the gantry blocking the RPM external marker. For all PTV sizes the dose measurement is within 2σ positional uncertainty from the Eclipse calculated dose, indicating that dosimetric accuracy of gated treatments are not affected by the size of the PTV.

Dosimetric measurements of the middle size PTV were taken using exhale durations between 2 s and 5 s. Our measurements show that as long as the baseline of the trace is kept at a constant level throughout the delivery, the duration of exhale does not have a significant effect on the final dose measurements and all dose measurements are within 2σ positional uncertainty from the Eclipse calculated doses. It is important to note that for amplitude gating at exhale, increasing the duration of exhale leads to higher duty cycles and more efficient treatment deliveries.

The intra-fraction target motion within the gating window is inevitable in gated treatments and leads to dose-blurring (due to the relative motion between a non-stationary target and the dose distribution meant to be delivered to a static target) and the interplay effect (due to the relative motion between MLC leaves and the non-static target). For an infinitely small gating window, the target residual motion is negligible. In this case the dose distribution delivered to a non-static target should match the dose distribution delivered to a stationary target in a non-gated delivery. As the width of the gating window increases, the amplitude of the residual target motion becomes greater, which results in higher levels of dose-blurring and interplay effect. In this study, we introduce the parameter ARDD, which is the average displacement of the detector from the baseline within the gate, and use this parameter to account for the dose-blurring effect. This method is successful for gate widths below 8 mm and baseline drift levels below 4 mm, meaning most of the dose measurements at the isocentre and along the penumbra are within the 95% confidence interval from the Eclipse calculated profile. As the size of the gate width and baseline drift level increase, the influence of the interplay effect on the dose delivered to the pinpoint ion chamber becomes more significant. In such cases, only correcting for dose-blurring using ARDD is not sufficient to explain the discrepancy between the dose measurements and the Eclipse calculations.

Furthermore, we monitored the effect of beam interruption on the overall accuracy of dose distribution in our measurements using the ArcCheck diode array using 2D Gamma analysis. The comparison between pass rates for gated and non-gated treatments strongly suggest that the occurrence of beam interruptions does not affect the accuracy of dose delivery of a gated treatment.

Chapter 5

Results and Discussion: Gated Dose Measurements Using Real Breathing Traces

This chapter presents the results of our dose measurements using the human breathing traces from six subjects. All six breathing patterns are shown in A.1. Features such as baseline drift and variation in exhale duration are always present in real breathing traces. Therefore, these measurements allow us to explore the effect of a combination of these features on gated treatments under various gate widths. Note that all measurements in this chapter are obtained using the treatment plan for PTV2. Similar to the measurements presented in the previous chapter, the dose measurements for the first three subjects are acquired at the isocentre and along the penumbra. The dose measurements for the last three subjects are obtained only at the isocentre and in the middle of the penumbra region. The results of these measurements are presented and discussed below.

5.1 Real Breathing Traces: Pinpoint Ion Chamber Dose Measurements

We recorded real breathing patterns of six subjects using the RPM system. The displacement between the overall peak and trough in a human chest wall is usually in the range of 15 mm to 20 mm. If we assume that there is a one to one relationship between the displacements of the human chest wall and a liver tumour, it would be ideal to maintain the same relationship between the motion of the Quasar phantom chest wall platform and its translation stage. This is, however, not easily achievable given the limitations inherent to the design and operation of the Quasar phantom. As described in section 3.1.1, the peak-to-peak amplitude of the chest wall platform of Quasar (and hence the RPM marker block) is always one-fourth of the peak-to-peak amplitude of the translation stage (and hence the pinpoint ion chamber). In order to import real breathing traces into the Quasar phantom, it is necessary to operate the phantom in the Oscillation mode, where the maximum peak-to-peak amplitudes of the platform and the translation stage are 7.5 mm and 30 mm, respectively. Although it is possible to use the thumbscrew on the translation stage to adjust the peak-to-peak amplitude of the translation stage to values lower than 30 mm, it is necessary to set the translation stage amplitude to its absolute maximum to ensure accurate positioning in the Position mode and programmable motion in the Oscillation mode (Quasar phantom user guide (January 2015, page 13) and private communications with the Quasar phantom engineering team at Modus Medical). These limitations forced us to scale the displacement between the overall peak and trough in the recorded human breathing patterns up to 30 mm, which is larger than the values observed (15 mm to 20 mm). Another option is to reduce the peak-to-peak amplitude of the breathing trace using the Quasar software. This, however, would result in the reduction of the peak-to-peak amplitude of the chest wall platform from 7.5 mm to 3 mm or less, which is much less than the actual displacement between the overall peak and trough in a human chest wall and reduces the ability of the RPM camera to detect the motion of the RPM block with high resolution. Therefore, we decided to scale the overall peak-to-peak amplitude of the recorded breathing traces to 30 mm to make use of the maximum range of motion achievable by the chest wall platform of the Quasar phantom.

The real breathing patterns from six subjects were used to acquire dosimetric measurements at the isocentre and along the penumbra for PTV2 using the pinpoint ion chamber. The choice of gate width is a compromise between the duty cycle and the residual motion. Based on the results presented in Chapter 4, we decided to use upper thresholds of 2 mm, 2.8 mm, and 4 mm for all six sets of measurements. Tables 5.1, 5.2, 5.3, 5.4, 5.5, and 5.6 list the duty cycles and ARDD values corresponding to each of the real breathing patterns. Figures 5.1, 5.2, 5.3, 5.4, 5.5, and 5.6 show the results of our dose measurements using the pinpoint ion chamber. Similar to Figures 4.7 and 4.10 shown in Chapter 4, each of the measured data points are shifted by their corresponding ARDD value to account for the dose-blurring effect. For all six breathing patterns, most (or all) of the measured data points are within the 95% confidence interval from the Eclipse calculated profile. Even after considering the positional error and correcting for the dose-blurring effect, it is evident that all measured data points either agree with the Eclipse profile or appear at a slightly lower dose. We used the test described in section 3.4.2 to rule out the occurrence of multiple beam interruptions during the radiation delivery as one of the sources of error. Therefore, this discrepancy between the measured and calculated doses could either be due to the interplay effect or the time delay in turning the beam on and off. Interplay effect has a randomized effect, meaning it can lead to both over-dosing and under-dosing of the detector, which is not applicable to the consistent slight under-dose effect that is evident in our results. We have explored the effect of leaf interplay on our measurements. The results are presented in section 5.2. The time delay in beam on/off, indeed, results in a decrease in the dose delivered to the pinpoint ion chamber and therefore can be the source of dose discrepancy between measured and calculated doses. The effect of time delay on dose measurements are discussed in section 5.3.

Table 5.1: Duty cycles & ARDD values for the breathing trace of Subject 1

Upper Threshold (mm)	Duty Cycle (%)	ARDD (mm)
2	13	1.300
2.8	20	1.705
4	28	2.146

Table 5.2: Duty cycles & ARDD values for the breathing trace of Subject 2

Upper Threshold (mm)	Duty Cycle (%)	ARDD (mm)
2	8	1.367
2.8	16	1.911
4	27	2.480

Table 5.3: Duty cycles & ARDD values for the breathing trace of Subject 3

Upper Threshold (mm)	Duty Cycle (%)	ARDD (mm)
2	5.5	1.305
2.8	9	1.737
4	15.5	2.451

Table 5.4: Duty cycles & ARDD values for the breathing trace of Subject 4

Upper Threshold (mm)	Duty Cycle (%)	ARDD (mm)
2	13	1.369
2.8	23.5	1.822
4	32.5	2.247

Table 5.5: Duty cycles & ARDD values for the breathing trace of Subject 5

Upper Threshold (mm)	Duty Cycle (%)	ARDD (mm)
2	4	1.348
2.8	10	1.995
4	20	2.703

Table 5.6: Duty cycles & ARDD values for the breathing trace of Subject 6

Upper Threshold (mm)	Duty Cycle (%)	ARDD (mm)
2	14	1.467
2.8	28	1.955
4	44	2.441

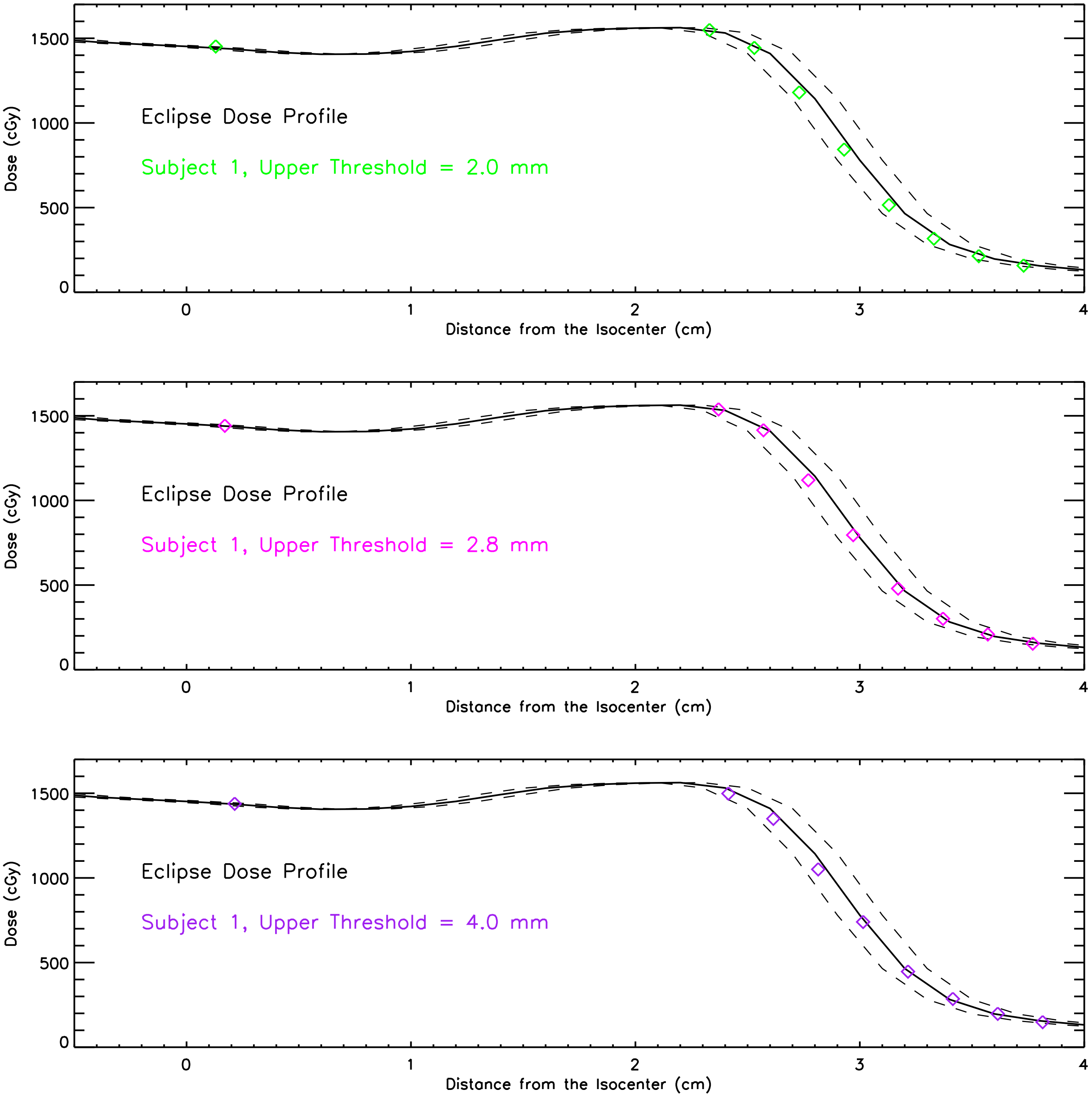

Figure 5.1: In each plot, the black solid curve shows the interpolation of all of the Eclipse calculated doses. The dashed curves show the 95% confidence interval. The coloured diamonds show the pinpoint ion chamber dose measurements using the breathing trace of Subject 1. Note that in these plots the dose measurements are shifted by the corresponding ARDD values.

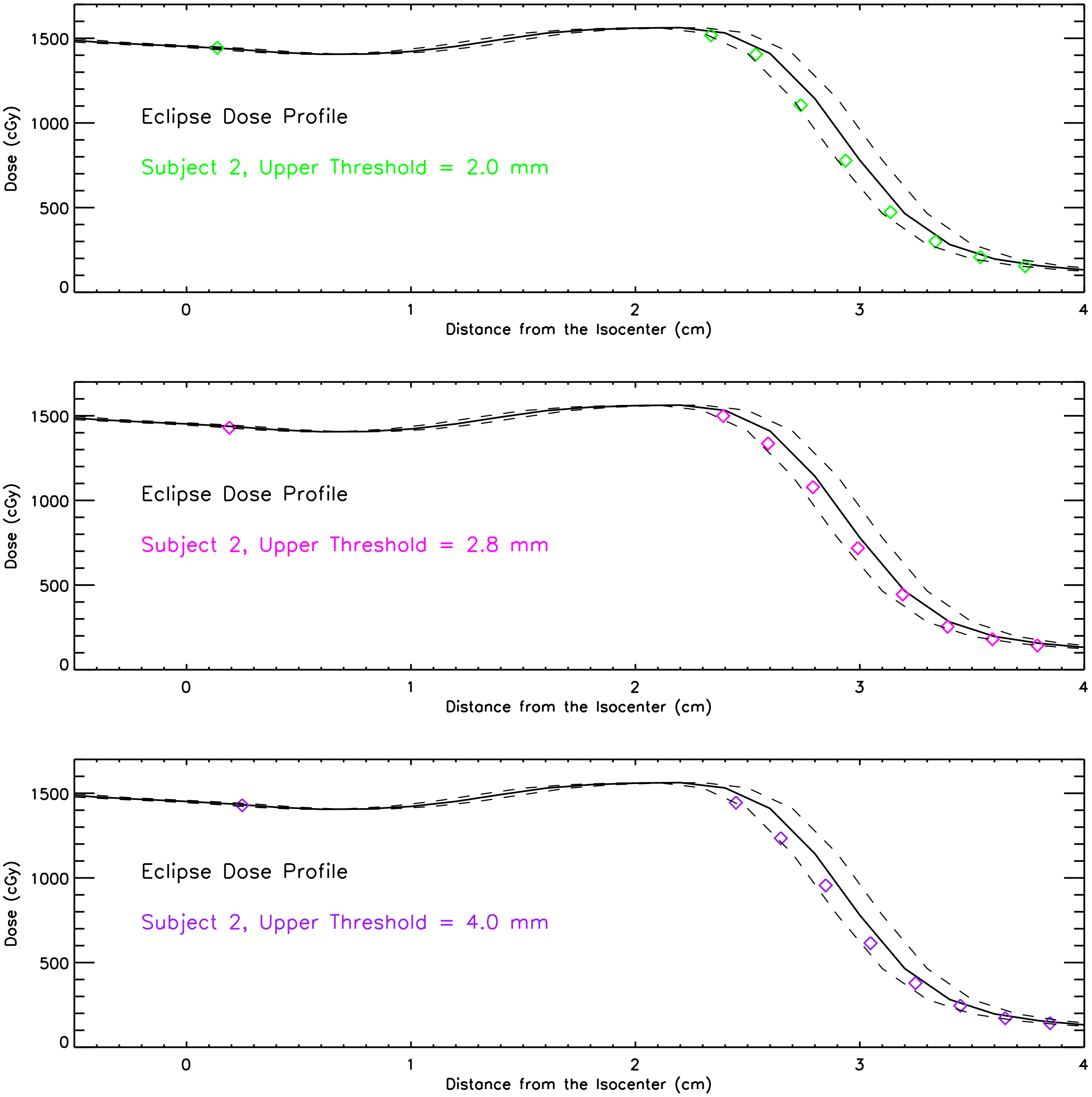

Figure 5.2: In each plot, the black solid curve shows the interpolation of all of the Eclipse calculated doses. The dashed curves show the 95% confidence interval. The coloured diamonds show the pinpoint ion chamber dose measurements using the breathing trace of Subject 2. Note that in these plots the dose measurements are shifted by the corresponding ARDD values.

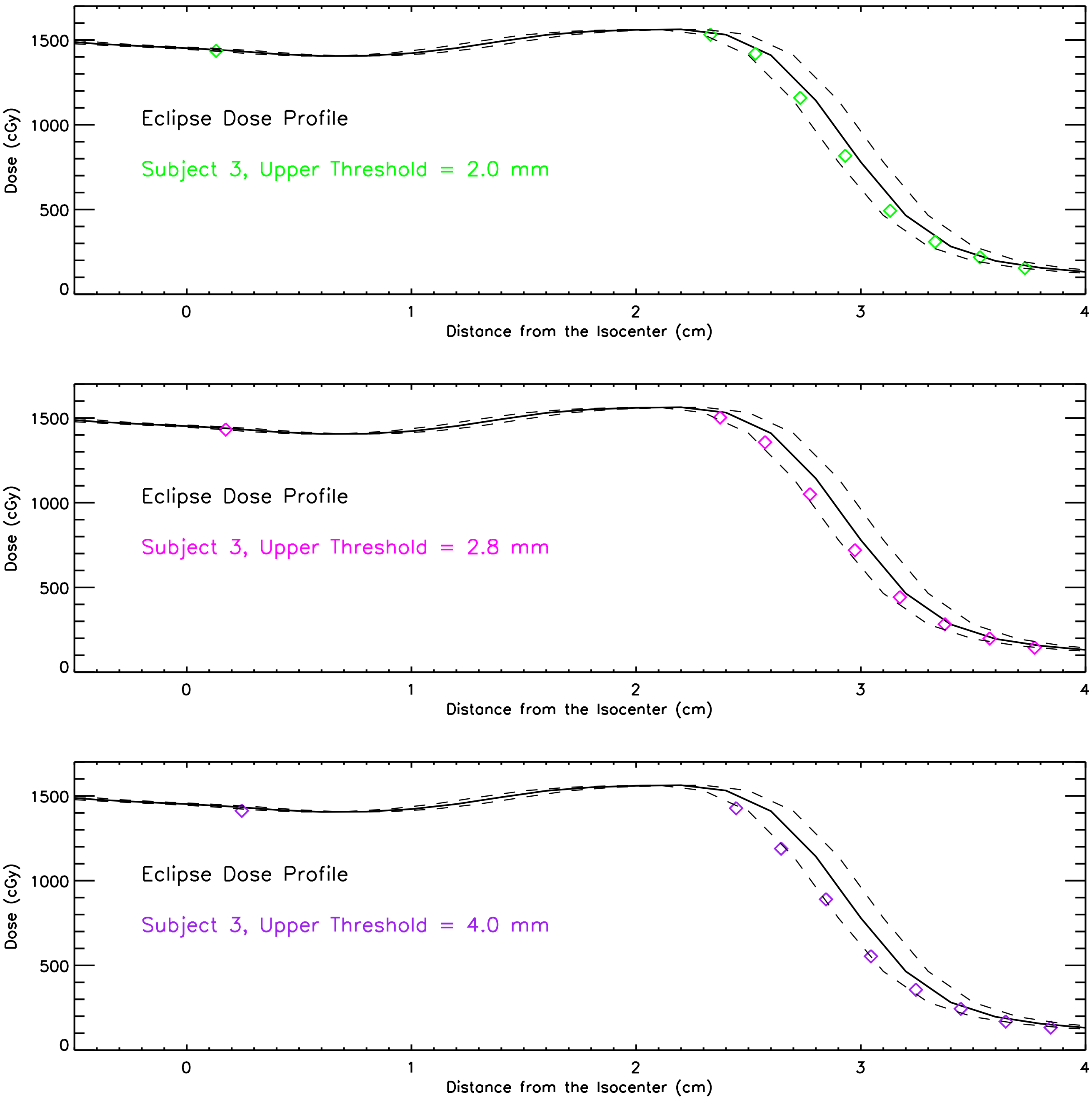

Figure 5.3: In each plot, the black solid curve shows the interpolation of all of the Eclipse calculated doses. The dashed curves show the 95% confidence interval. The coloured diamonds show the pinpoint ion chamber dose measurements using the breathing trace of Subject 3. Note that in these plots the dose measurements are shifted by the corresponding ARDD values.

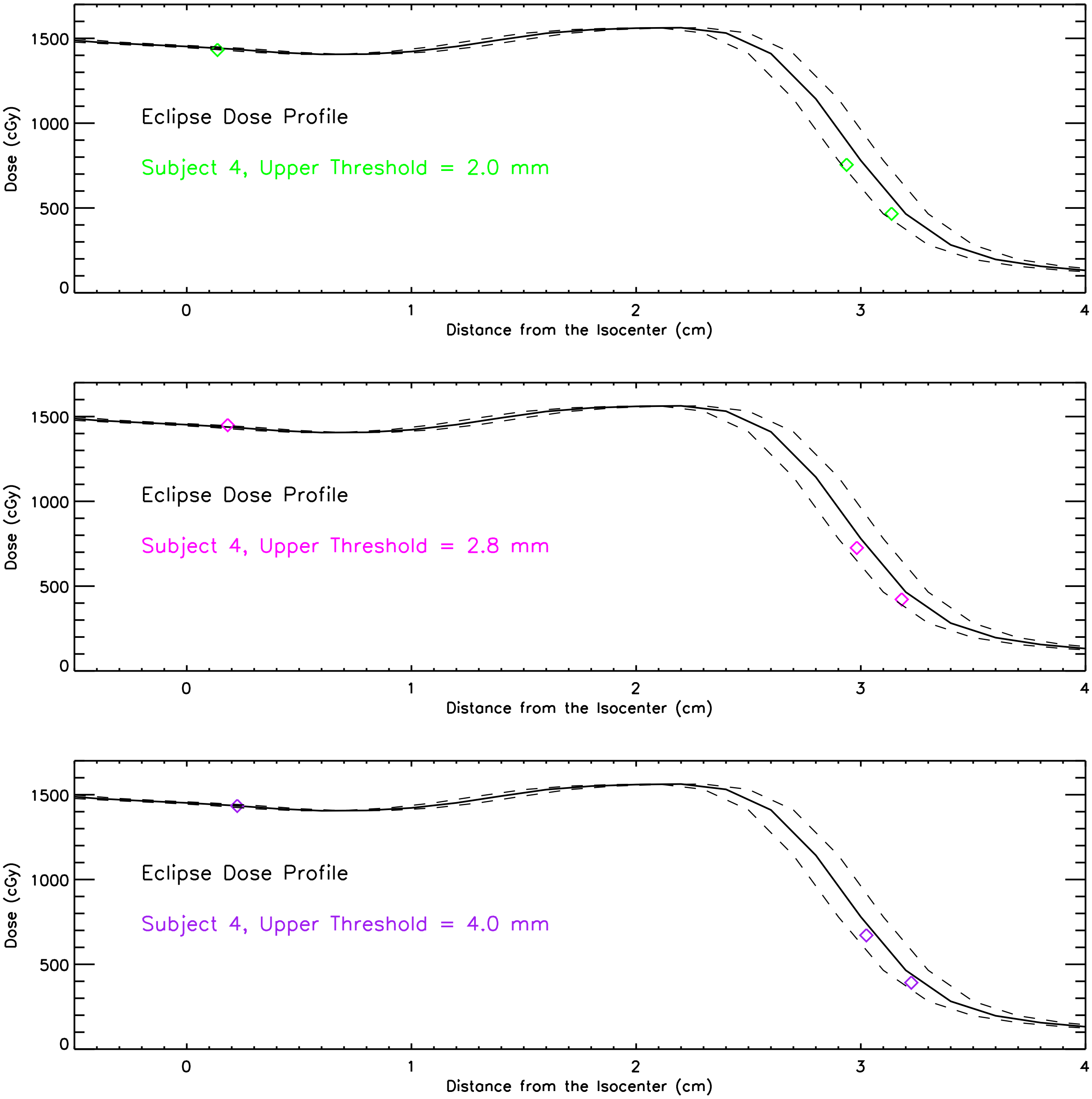

Figure 5.4: In each plot, the black solid curve shows the interpolation of all of the Eclipse calculated doses. The dashed curves show the 95% confidence interval. The coloured diamonds show the pinpoint ion chamber dose measurements using the breathing trace of Subject 4. Note that in these plots the dose measurements are shifted by the corresponding ARDD values.

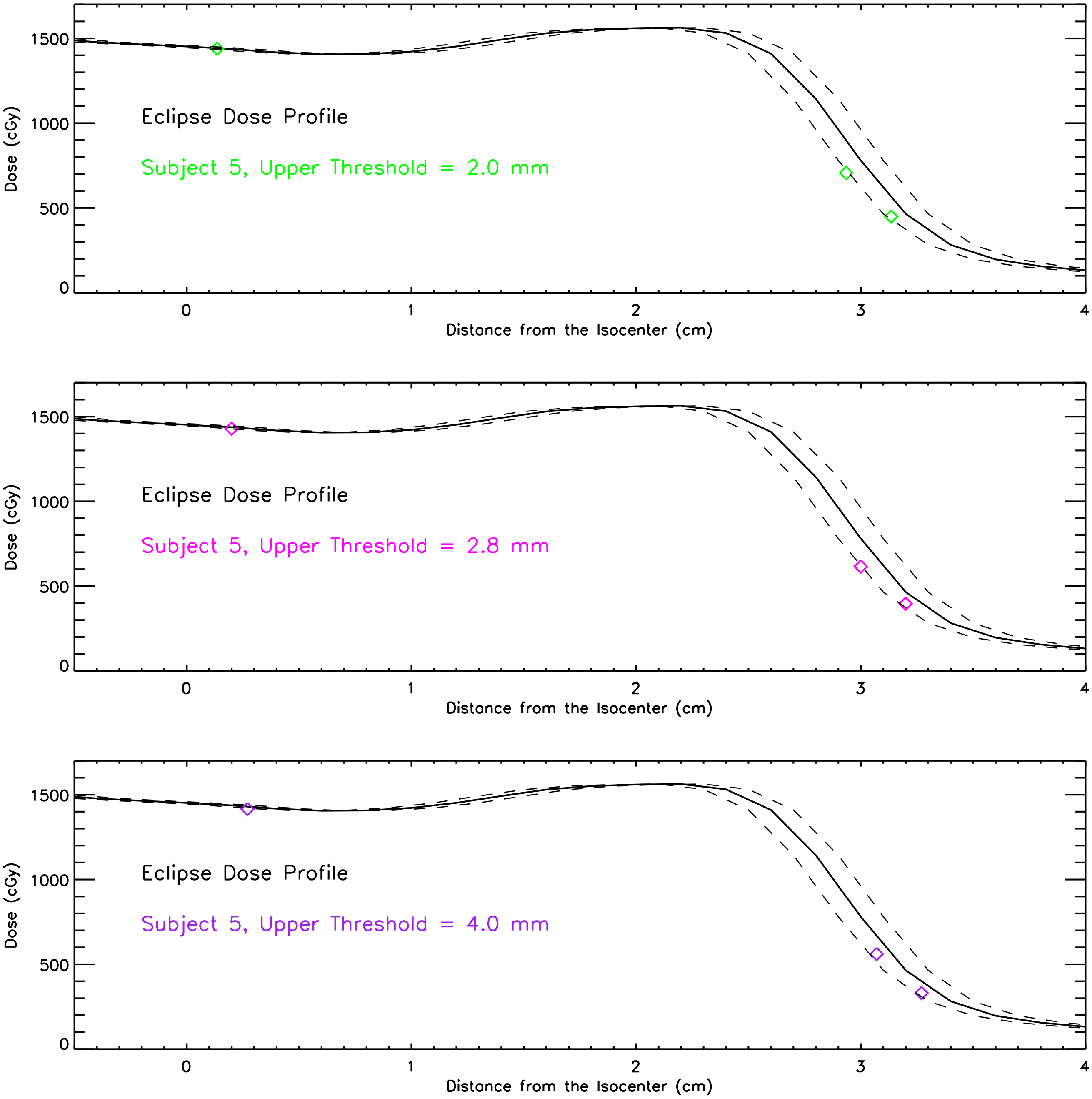

Figure 5.5: In each plot, the black solid curve shows the interpolation of all of the Eclipse calculated doses. The dashed curves show the 95% confidence interval. The coloured diamonds show the pinpoint ion chamber dose measurements using the breathing trace of Subject 5. Note that in these plots the dose measurements are shifted by the corresponding ARDD values.

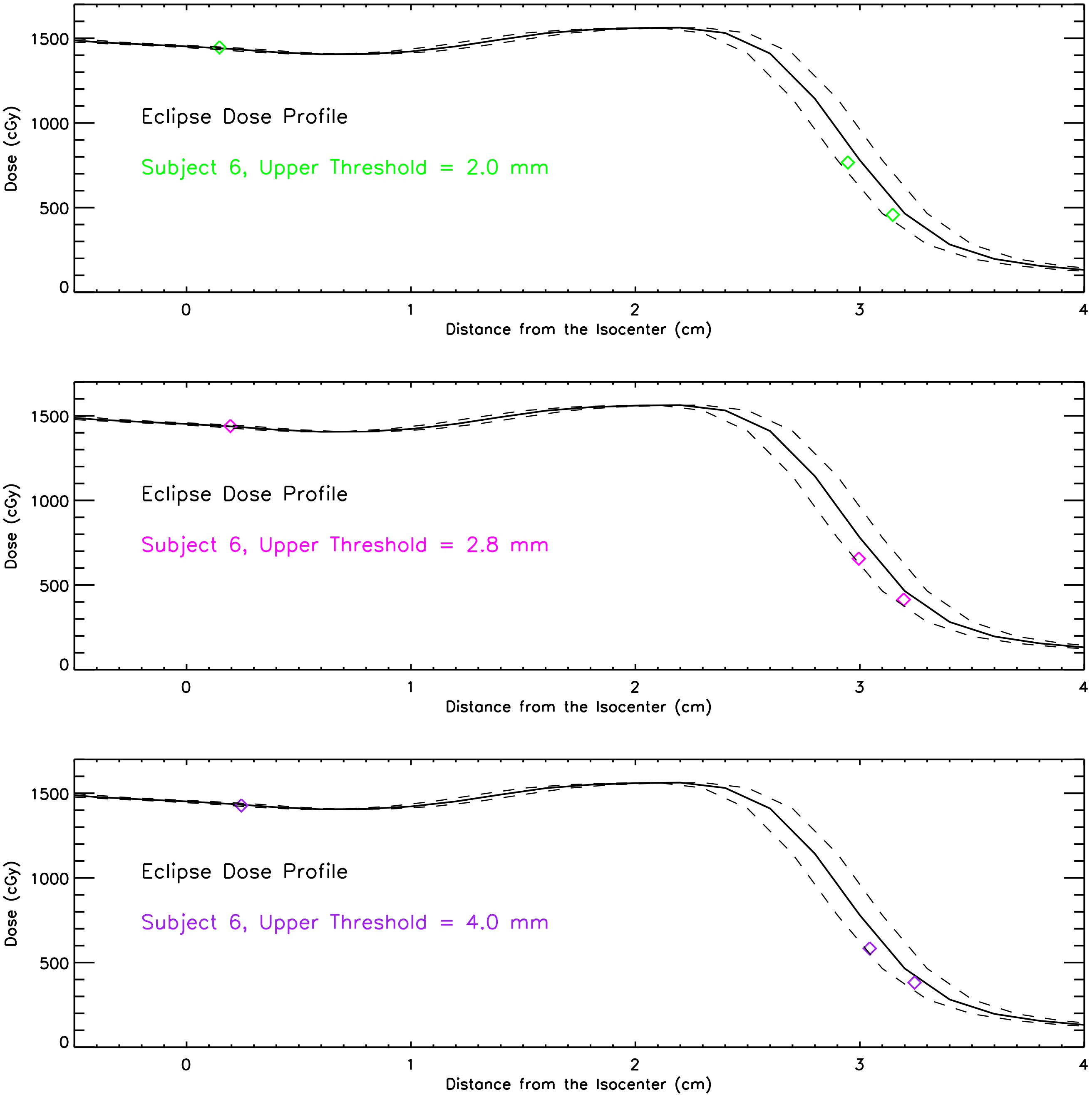

Figure 5.6: In each plot, the black solid curve shows the interpolation of all of the Eclipse calculated doses. The dashed curves show the 95% confidence interval. The coloured diamonds show the pinpoint ion chamber dose measurements using the breathing trace of Subject 6. Note that in these plots the dose measurements are shifted by the corresponding ARDD values.

5.2 Interplay Effect

As described in section 3.4.3, interplay effect occurs due to the relative motion between the MLC leaves and a non-stationary target and can lead to hot spots and cold spots inside or outside the target. To characterize the dosimetric effect of leaf interplay on our measurements, the breathing trace of Subject 2 was used to measure the dose in the middle of the penumbra of PTV2 (i.e., at 3.0 cm from the isocentre) using upper thresholds of 2.0 mm, 2.8 mm, and 4.0 mm. The measurement for each gate width was repeated five times and we ensured that for each measurement, the initial beam-on occurred at a different part of the breathing trace. The standard deviation of dose measurements were 3.7 cGy, 19.7 cGy, and 19.8 cGy for gate widths of 2.0 mm, 2.8 mm, and 4.0 mm, respectively (0.3%, 1.4%, and 1.4% relative to dose at isocentre). These results are in agreement with a previous study by Kang et al. (2010) and demonstrate that interplay effect becomes more significant as the gate width increases. The effect of leaf interplay is depicted in Figure 5.7. In each plot, the error bar shows 2σ uncertainty due to leaf interplay and is placed on the data point that corresponds to our measurements at 3.0 cm from the isocentre.

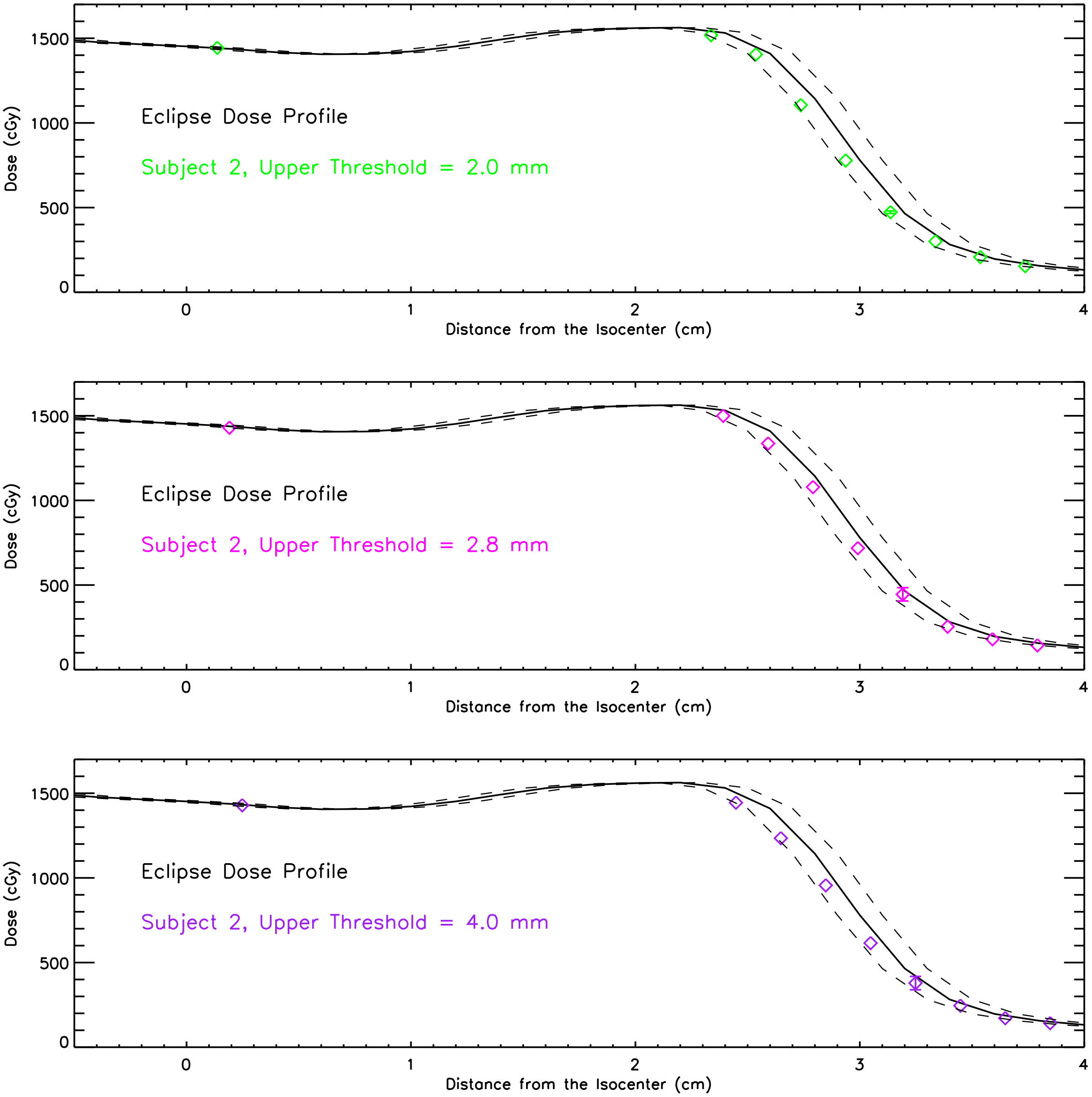

Figure 5.7: In each plot, the black solid curve shows the interpolation of all of the Eclipse calculated doses. The dashed curves show the 95% confidence interval. The coloured diamonds show the pinpoint ion chamber dose measurements using the breathing trace of Subject 2. Note that in these plots the dose measurements are shifted by the corresponding ARDD values. The error bars show 2σ uncertainty due to leaf interplay.

5.3 Time Delay in Beam On/Off

The recommended temporal accuracy for respiratory gating is 100 ms (TG142; Klein et al. 2009). To find out if such time delay would account for the slight under-dosing evident in Figures 5.1 to 5.6, we calculated updated ARDD values for each of the six real breathing traces for all three upper threshold values (2 mm, 2.8 mm, and 4 mm). For this calculation, we used the same method explained in section 3.3.2. To account for the beam on/off time delays for each beam-on interval, the group of data points that are included in the ARDD calculation start and finish with the data points that come 100 ms after the start and finish times of beam-on for that particular beam-on interval *if* the delay did not exist. As an example, Figure 5.8 shows the pinpoint ion chamber measurements for Subject 1 with the data points shifted by the updated ARDD values that account for 100 ms time delay in beam on/off. Accounting for the time delay in ARDD calculation shifts the measured data points further towards the lower dose region of the dose profile and leads to a better agreement between the Eclipse calculations and the measured data points. It is clear, however, that the shift in the location of data points in comparison to those in Figure 5.1 is very small and even difficult to notice.

We also calculated updated values of ARDD for each of the six real breathing traces for all three upper threshold values using time delays between 50 ms to 500 ms in 50 ms increments to find the range of time delay that would give the best visual agreement between the measurements and the Eclipse calculated doses. We found the beam on/off time delay in the range 150 ms to 400 ms would result in the best agreement, which is higher than the expected values for the RPM system in amplitude gating (see section 3.4.4 for a review on the previous studies on beam delay). Note that in this analysis we assumed that the beam-on and beam-off time delays are identical, which is not necessarily the case. Experiment designs that differentiate between the delays in beam-on and beam-off and taking advantage of more sophisticated optimization methods are indeed required to characterize the beam lag more accurately.

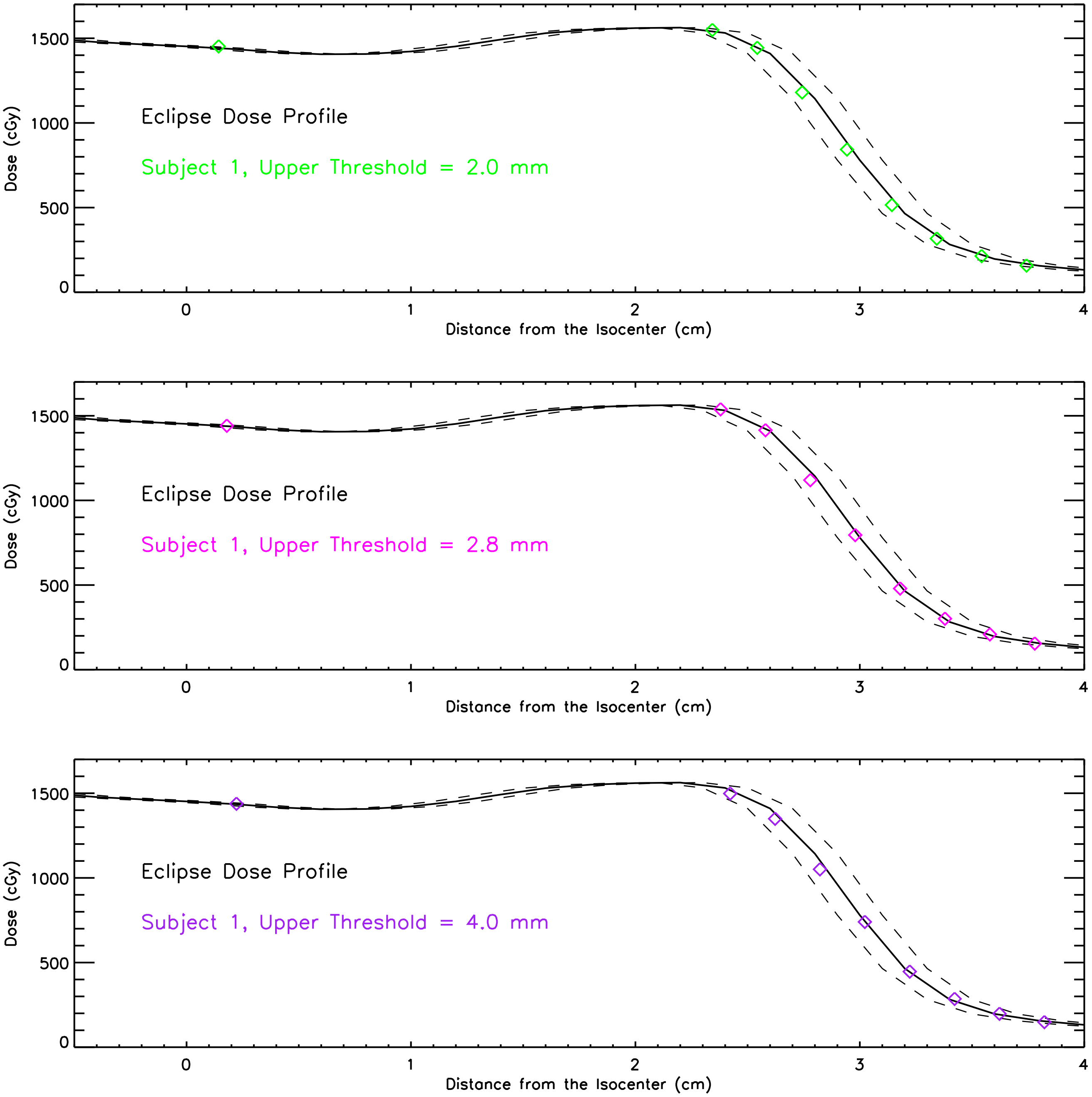

Figure 5.8: In each plot, the black crosses show Eclipse calculated doses at the locations, where measurements were acquired (i.e., isocentre and penumbra) for PTV2. The black solid curve shows the interpolation of all of the Eclipse calculated doses. The coloured diamonds show the pinpoint ion chamber dose measurements using the breathing trace of Subject 1. Note that in these plots the dose measurements are shifted by the corresponding ARDD values including 100 ms of beam delay.

5.4 Real Breathing Traces: ArcCheck Dose Measurements

For all six real breathing patterns and three upper threshold values, ArcCheck diode dose measurements were monitored. Tables 5.7 to 5.12 show the Gamma pass rates (2mm/2%) for the six subjects. The shape of a breathing trace and the size of the gate window determine the duty cycle and the number of beam interruptions during the gated treatment. It is, however, evident from the ArcCheck measurements that the accuracy of the overall dose distribution to a stationary phantom such as ArcCheck is not affected by the number of beam interruptions.

Table 5.7: Gamma pass rates (2mm/2%) for ArcCheck measurements of PTV2 with gating at isocentre and in the middle of penumbra for various gate widths and using the breathing trace of Subject 1.

	Isocentre		Penumbra	
Upper Threshold (mm)	10% Threshold	40% Threshold	10% Threshold	40% Threshold
2	99.8%	99.6%	98.3%	96.7%
2.8	99.2%	98.3%	97.9%	96.2%
4	99.2%	98.3%	97.9%	95.8%

Table 5.8: Gamma pass rates (2mm/2%) for ArcCheck measurements of PTV2 with gating at isocentre and in the middle of penumbra for various gate widths and using the breathing trace of Subject 2.

	Isocentre		Penumbra	
Upper Threshold (mm)	10% Threshold	40% Threshold	10% Threshold	40% Threshold
2	99.0%	97.9%	98.3%	96.6%
2.8	99.2%	98.3%	98.3%	96.6%
4	99.2%	98.3%	97.9%	95.8%

Table 5.9: Gamma pass rates (2mm/2%) for ArcCheck measurements of PTV2 with gating at isocentre and in the middle of penumbra for various gate widths and using the breathing trace of Subject 3.

	Isocentre		Penumbra	
Upper Threshold (mm)	10% Threshold	40% Threshold	10% Threshold	40% Threshold
2	99.2%	98.3%	98.1%	97.5%
2.8	99.2%	98.3%	97.7%	95.4%
4	98.3%	96.5%	97.9%	95.8%

Table 5.10: Gamma pass rates (2mm/2%) for ArcCheck measurements of PTV2 with gating at isocentre and in the middle of penumbra for various gate widths and using the breathing trace of Subject 4.

	Isocentre		Penumbra	
Upper Threshold (mm)	10% Threshold	40% Threshold	10% Threshold	40% Threshold
2	99.8%	99.6%	98.5%	97.1%
2.8	99.8%	99.6%	98.5%	97.1%
4	99.8%	99.6%	98.5%	97.1%

Table 5.11: Gamma pass rates (2mm/2%) for ArcCheck measurements of PTV2 with gating at isocentre and in the middle of penumbra for various gate widths and using the breathing trace of Subject 5.

	Isocentre		Penumbra	
Upper Threshold (mm)	10% Threshold	40% Threshold	10% Threshold	40% Threshold
2	99.4%	99.6%	99.2%	99.2%
2.8	99.8%	99.6%	99.2%	98.3%
4	99.8%	99.6%	99.2%	98.3%

Table 5.12: Gamma pass rates (2mm/2%) for ArcCheck measurements of PTV2 with gating at isocentre and in the middle of penumbra for various gate widths and using the breathing trace of Subject 6.

	Isocentre		Penumbra	
Upper Threshold (mm)	10% Threshold	40% Threshold	10% Threshold	40% Threshold
2	99.8%	99.6%	98.3%	96.6%
2.8	99.6%	99.2%	98.3%	96.6%
4	99.6%	99.2%	97.7%	95.4%

5.5 Discussion and Conclusion

The results in this chapter demonstrate the possibility of dosimetric measurements using our custom-made setup for human breathing patterns. The main source of discrepancy between Eclipse calculated dose and the dose delivered to a moving target is the dose-blurring effect. In this chapter, we used the quantity ARDD introduced in Chapter 3 to account for this discrepancy when real breathing patterns are used to gate the radiation delivery. Once the measured doses are corrected for the dose-blurring effect, it is clear that our measurements are within the 2σ positional uncertainty of the Eclipse calculated dose profile. We also explored the effects of time delay in beam on/off and leaf interplay on the dose measurements. Although, the influence of these effects are not significant (especially compared to that of dose-blurring), they can improve the agreement between the Eclipse calculated doses and the measurements.

Such excellent agreement between expected and measured doses allows us to use this setup to ensure that the gating system limits the radiation delivery to the correct part of the breathing cycle. To use this method as a QA procedure, the user records the patient's breathing trace prior to the first treatment fraction. The trace is then used to calculate the duty cycle of the treatment for various gate sizes and determine the size that gives the best balance between the treatment efficiency and target residual motion. Subsequently, the verification plan will be delivered to the setup described in this study in gated mode using the real breathing trace. The setup will be centred in the middle of the penumbra region. This configuration allows the user to verify the overall dose accuracy using the ArcCheck measurements and confirm the accuracy of the gating system to deliver the dose in the correct part of the breathing trace.

A disadvantage of this method is the labor-intensive and time consuming process of achieving the accurate setup (≈ 1 hr). This is mainly due to the use of two phantoms in this procedure (i.e., ArcCheck array and Quasar phantom) and the amount of time required for their proper alignment. Therefore, the current setup should be streamlined in the future or only used for the patient specific QA of some of the patients.

Chapter 6

Conclusions

Respiratory gating helps reduce the PTV size by restricting the radiation delivery to a specific part of the breathing cycle. A disadvantage of this method, however, is the increased treatment time due to multiple beam interruptions during the treatment. Combination of gating with fast delivery techniques such as, VMAT especially in the FFF mode, allows us to take advantage of the high dose rates to deliver high doses per fraction while maintaining reasonable treatment times. The combination of these treatment techniques are very well suited for SABR treatments which involve delivery of high dose per fraction.

QA is a crucial aspect of any radiotherapy treatment technique and becomes even more imperative when the treatment involves high dose rates and significant dose gradients of VMAT SABR treatments combined with the complexity of respiratory gating. This thesis describes a novel QA method for amplitude gating, which takes advantage of the high dose gradient region of SABR treatments to detect any inaccuracies in the performance of the Varian RPM gating system. This method is also unique because it involves the design and construction of an interface that connects the translation stage of the Quasar respiratory motion phantom to an ion chamber insert. This insert can hold and drive a pinpoint ion chamber inside the ArcCheck diode array based on the breathing pattern imported into the Quasar phantom. The experiment is setup such that the radiation beam is turned on during the exhale and the pinpoint chamber measures the dose in the middle of the penumbra region, where the dose gradient is at its maximum.

Using the setup described above, pinpoint ion chamber was used to measure the dose at the isocentre and along the penumbra using synthetic breathing traces. Systematic changes were introduced to the PTV size, exhale duration, baseline drift, and gate width to explore their effects on dose measurements. Our results show that the changes in PTV size and exhale duration do not influence the dose measured by the pinpoint ion chamber. Changes in gate width and baseline drift, however, affect the detector residual motion, which results in variation in the level of dose-blurring and interplay effects. A new parameter, Average Residual Detector Displacement (ARDD), is introduced in this thesis and is used to take into account the effect of dose-blurring, which is the main source of discrepancy between the Eclipse calculated dose profile and the measured doses by a non-stationary detector especially in the penumbra. For gate widths smaller than 8 mm and baseline drift levels smaller than 4 mm, once the effect of dose-blurring is taken into account, the pinpoint ion chamber dose measurements are mostly within 2σ positional uncertainty from the Eclipse dose profile. As the gate width and baseline drift increases, accounting for the dose-blurring effect is no longer sufficient to explain the discrepancy between measured and calculated doses. Indeed, previous studies (Kang et al. 2010) have suggested that dose interplay effect increases for larger amplitudes of residual motion.

This thesis also includes dose measurements for radiation deliveries that are gated using six real breathing traces with gate widths of 2 mm, 2.8 mm, and 4 mm. Again, once the parameter ARDD was used to account for dose-blurring, the dose measurements are mostly within 2σ positional uncertainty from Eclipse calculated doses. These results demonstrate that the reliability and accuracy of the RPM gating system at BCCA-VICC. Lastly, the overall dose distribution was monitored using the ArcCheck diode array measurements under various gating schemes and was compared to the Eclipse calculated dose map using a 2D Gamma analysis. The Gamma pass rates for 2mm/2% criteria show that the beam interruptions during the treatment do not degrade the fidelity of the radiation delivery in a gated treatment.

The future work to this thesis should include experiment designs to improve our measurements of the time delay in beam on/off as well as the leaf interplay effect. With better characterization of these effects, we will be better equipped to evaluate the sensitivity of our QA method to errors in the functionality in the gating system. Lastly, streamlining the setup (e.g., using indexed devices) is necessary to improve the efficiency and ease of use of this QA procedure.

Appendix A

Additional Information

A.1 Real Breathing Patterns

Figures A.1 to A.6 show the real breathing patterns used in this study. All six patterns were captured from healthy subjects using the RPM system. The overall peak-to-peak amplitudes of the patterns shown below are scaled to [-15 mm, +15 mm] by the Quasar software.

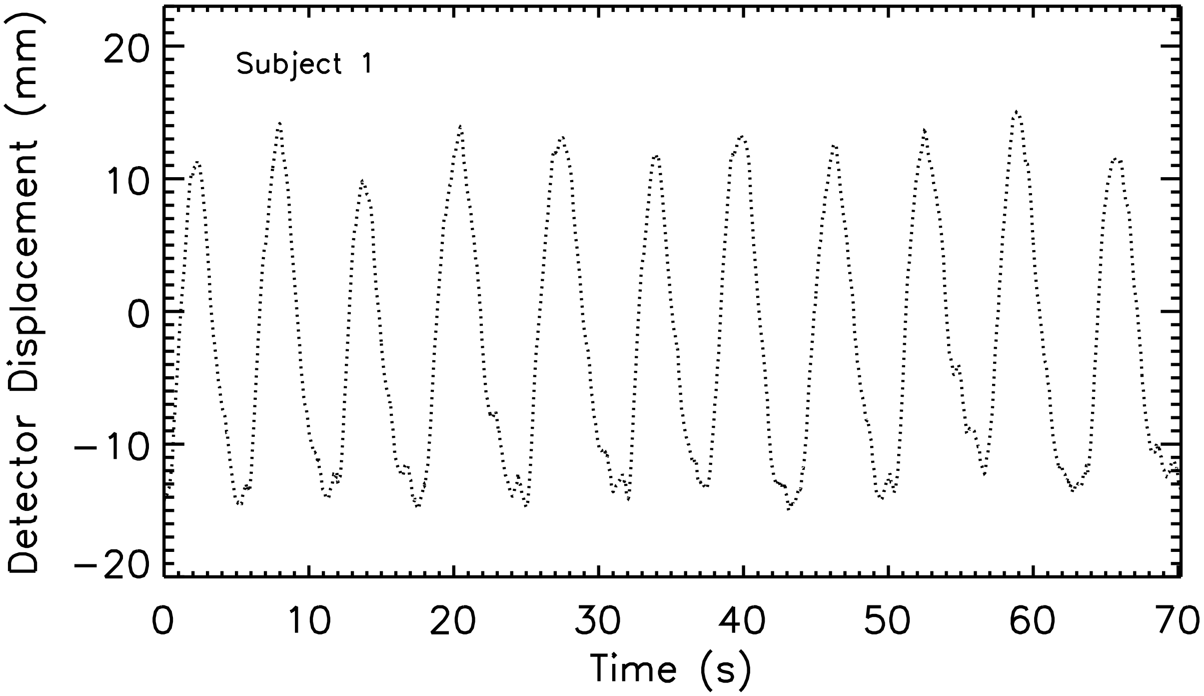

Figure A.1: Breathing pattern of Subject 1.

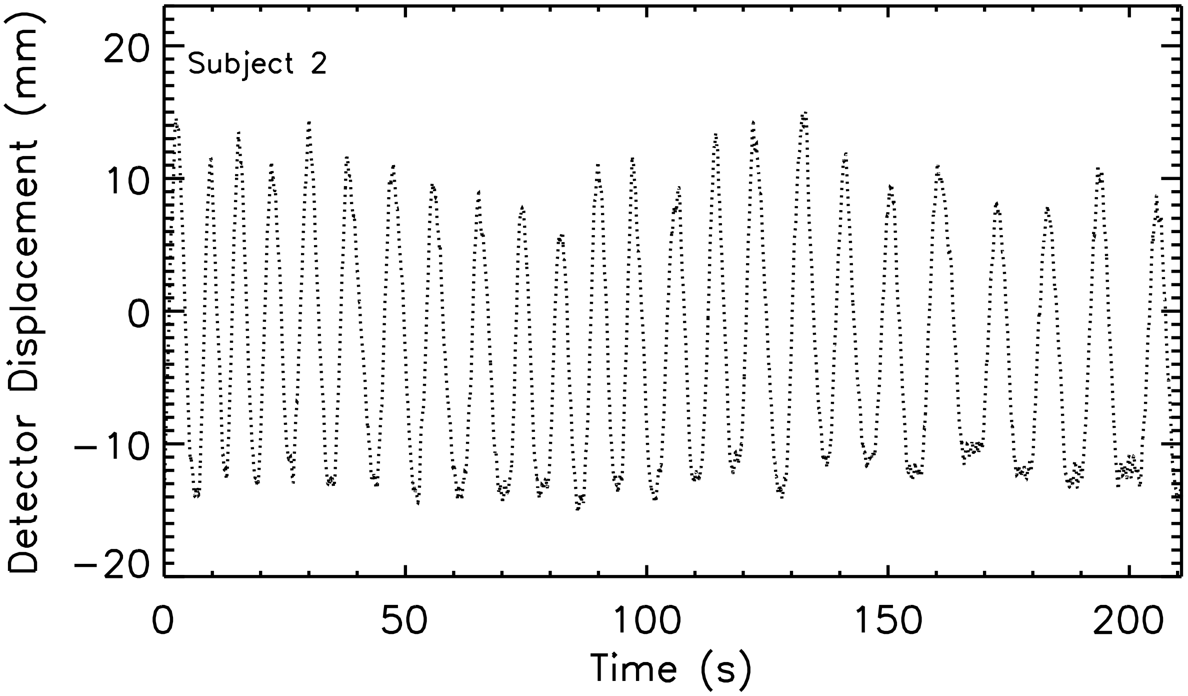

Figure A.2: Breathing pattern of Subject 2.

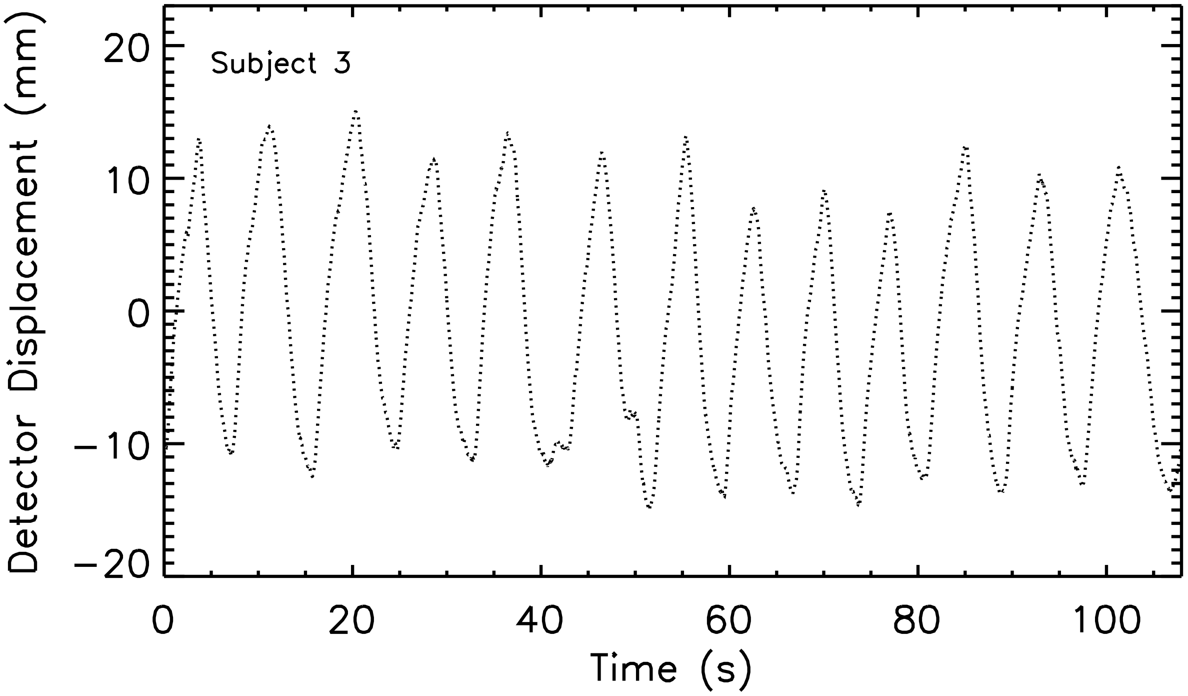

Figure A.3: Breathing pattern of Subject 3.

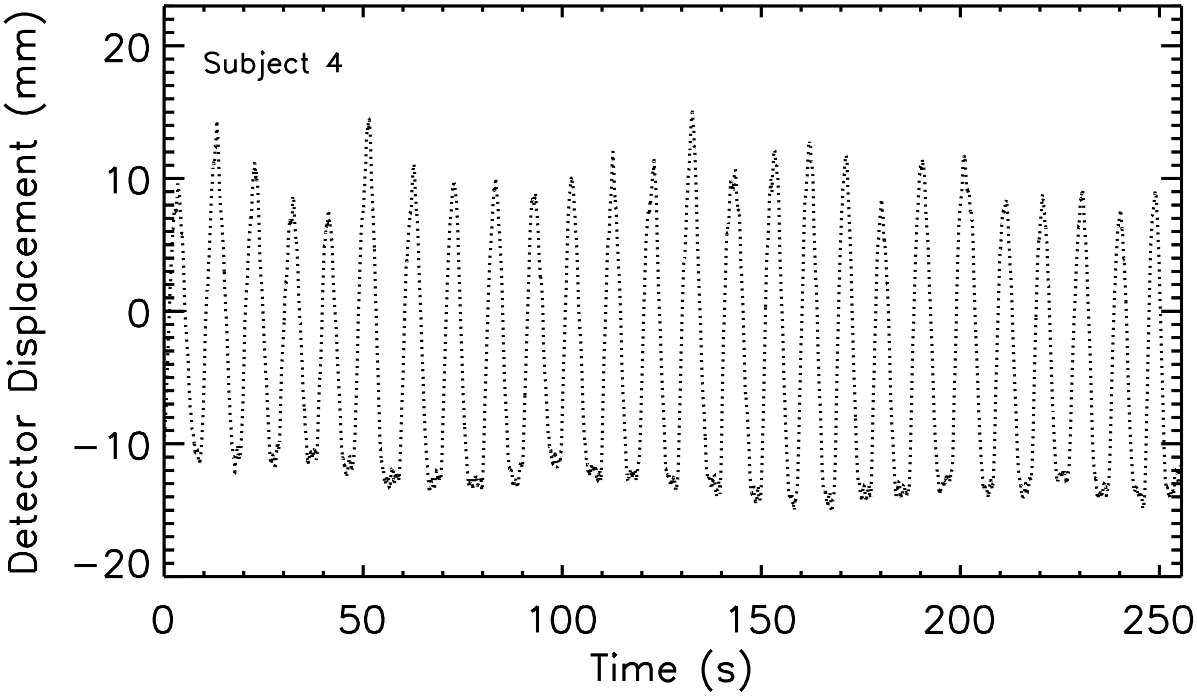

Figure A.4: Breathing pattern of Subject 4.

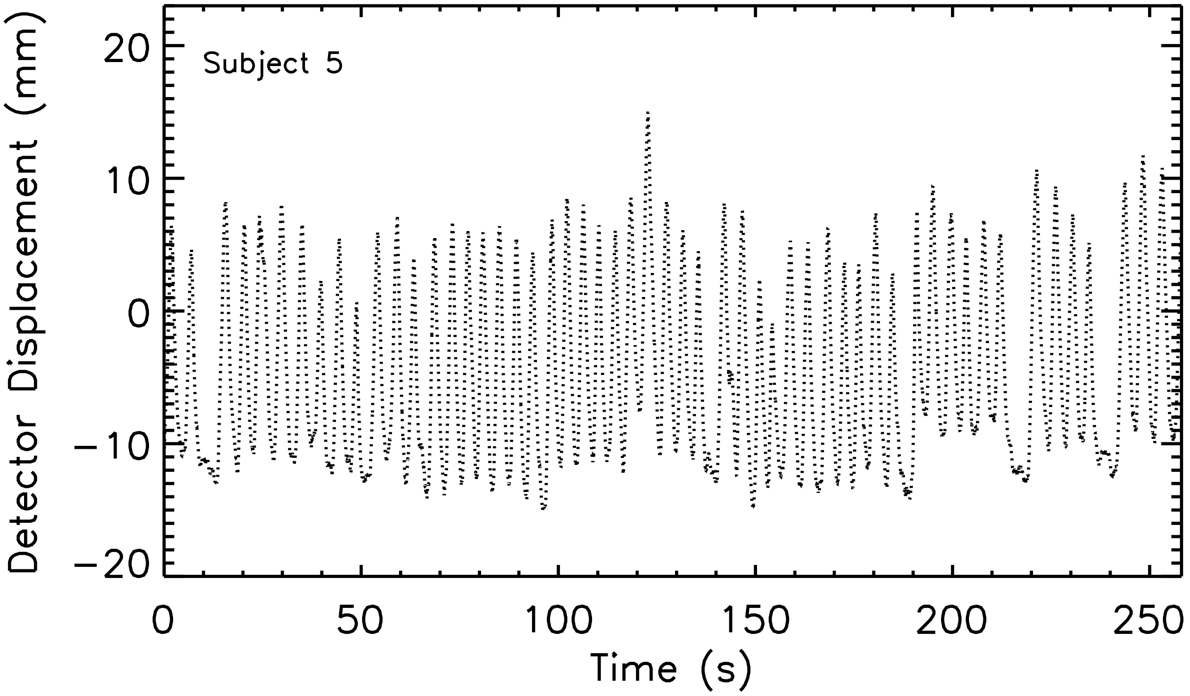

Figure A.5: Breathing pattern of Subject 5.

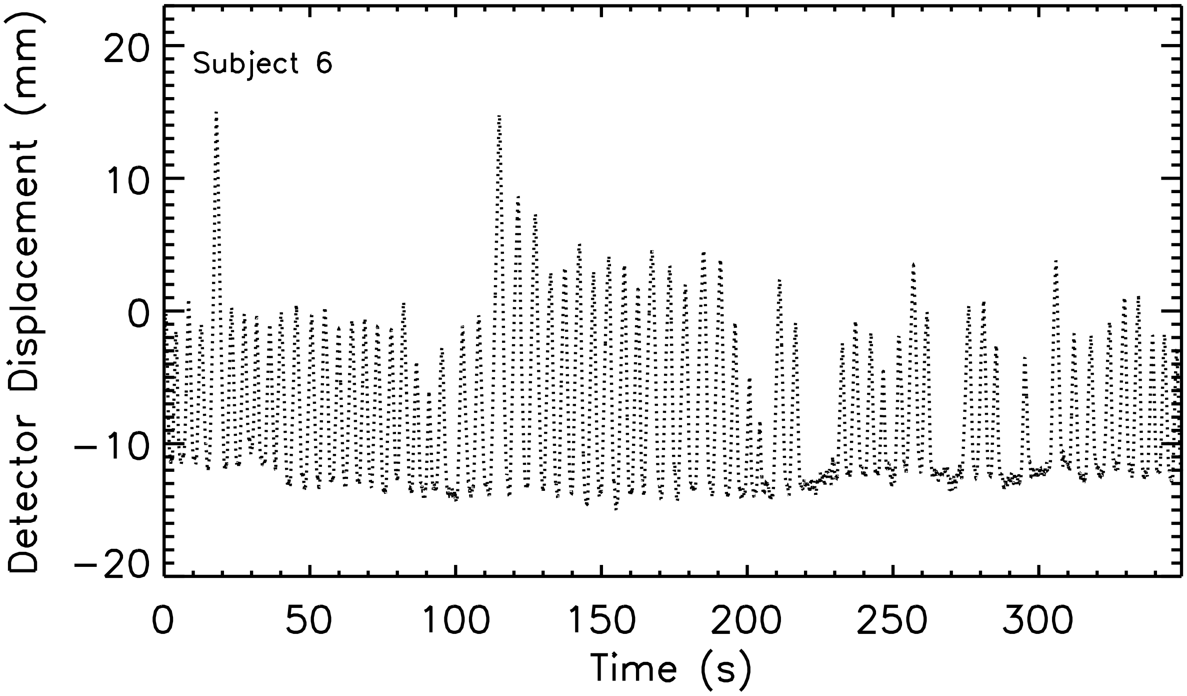

Figure A.6: Breathing pattern of Subject 6.

Bibliography

R. I. Berbeco, H. Mostafavi, G. C. Sharp, and S. B. Jiang. Towards fluoroscopic respiratory gating for lung tumours without radiopaque markers. *Phys Med Biol*, 50(19):4481–4490, Oct 2005.

R. I. Berbeco, C. J. Pope, and S. B. Jiang. Measurement of the interplay effect in lung IMRT treatment using EDR2 films. *J Appl Clin Med Phys*, 7(4):33–42, 2006.

N. Bhagat, N. Fidelman, J. C. Durack, J. Collins, R. L. Gordon, J. M. LaBerge, and R. K. Kerlan. Complications associated with the percutaneous insertion of fiducial markers in the thorax. *Cardiovasc Intervent Radiol*, 33(6):1186–1191, Dec 2010.

J. P. Bissonnette, K. N. Franks, T. G. Purdie, D. J. Moseley, J. J. Sonke, D. A. Jaffray, L. A. Dawson, and A. Bezjak. Quantifying interfraction and intrafraction tumor motion in lung stereotactic body radiotherapy using respiration-correlated cone beam computed tomography. *Int. J. Radiat. Oncol. Biol. Phys.*, 75(3):688–695, Nov 2009.

T. Bortfeld, K. Jokivarsi, M. Goitein, J. Kung, and S. B. Jiang. Effects of intra-fraction motion on IMRT dose delivery: statistical analysis and simulation. *Phys Med Biol*, 47(13):2203–2220, Jul 2002.

T. Bortfeld, R. Schmidt-Ullrich, W. De Neve, and D.E. Wazer. *Image-Guided IMRT*. Springer Berlin Heidelberg, 2005. ISBN 9783540205111. URL `https://books.google.ca/books?id=km3XREnMXgYC`.

J. Cashmore. The characterization of unflattened photon beams from a 6 MV linear accelerator. *Phys Med Biol*, 53(7):1933–1946, Apr 2008.

S Ceberg, C Ceberg, M Falk, P Munk af Rosenschld, and S J Bck. Evaluation of breathing interplay effects during vmat by using 3d gel measurements. *Journal of Physics: Conference Series*, 444(1):012098, 2013.

Q. S. Chen, M. S. Weinhous, F. C. Deibel, J. P. Ciezki, and R. M. Macklis. Fluoroscopic study of tumor motion due to breathing: facilitating precise radiation therapy for lung cancer patients. *Med Phys*, 28(9):1850–1856, Sep 2001.

B. P. Chugh, S. Quirk, L. Conroy, and W. L. Smith. Measurement of time delays in gated radiotherapy for realistic respiratory motions. *Med Phys*, 41(9):091702, Sep 2014.

C. S. Chui, E. Yorke, and L. Hong. The effects of intra-fraction organ motion on the delivery of intensity-modulated field with a multileaf collimator. *Med Phys*, 30(7): 1736–1746, Jul 2003.

M. Dalaryd, G. Kragl, C. Ceberg, D. Georg, B. McClean, S. af Wetterstedt, E. Wieslander, and T. Knoos. A Monte Carlo study of a flattening filter-free linear accelerator verified with measurements. *Phys Med Biol*, 55(23):7333–7344, Dec 2010.

S. C. Davies, A. L. Hill, R. B. Holmes, M. Halliwell, and P. C. Jackson. Ultrasound quantitation of respiratory organ motion in the upper abdomen. *Br J Radiol*, 67 (803):1096–1102, Nov 1994.

G. Delaney, S. Jacob, C. Featherstone, and M. Barton. The role of radiotherapy in cancer treatment: estimating optimal utilization from a review of evidence-based clinical guidelines. *Cancer*, 104(6):1129–1137, Sep 2005.

Alejandro Forner, Josep M Llovet, and Jordi Bruix. Hepatocellular carcinoma. *The Lancet*, 379(9822):1245 – 1255, 2012.

B. Gagel, C. Demirel, A. Kientopf, M. Pinkawa, M. Piroth, S. Stanzel, C. Breuer, B. Asadpour, T. Jansen, R. Holy, J. E. Wildberger, and M. J. Eble. Active breathing control (ABC): determination and reduction of breathing-induced organ motion in the chest. *Int. J. Radiat. Oncol. Biol. Phys.*, 67(3):742–749, Mar 2007.

P. Giraud and R. Garcia. [Respiratory gating for radiotherapy: main technical aspects and clinical benefits]. *Bull Cancer*, 97(7):847–856, Jul 2010.

M. Goharian and R. F. Khan. Measurement of time delay for a prospectively gated CT simulator. *J Med Phys*, 35(2):123–127, Apr 2010.

H. Guana. Time delay study of a CT simulator in respiratory gated CT scanning. *Med Phys*, 33(4):815–819, Apr 2006.

G. Harauz and M. J. Bronskill. Comparison of the liver's respiratory motion in the supine and upright positions: concise communication. *J. Nucl. Med.*, 20(7):733–735, Jul 1979.

A. J. Hayden, M. Rains, and K. Tiver. Deep inspiration breath hold technique reduces heart dose from radiotherapy for left-sided breast cancer. *J Med Imaging Radiat Oncol*, 56(4):464–472, Aug 2012.

J. H. Heinzerling, J. F. Anderson, L. Papiez, T. Boike, S. Chien, G. Zhang, R. Abdulrahman, and R. Timmerman. Four-dimensional computed tomography scan analysis of tumor and organ motion at varying levels of abdominal compression during stereotactic treatment of lung and liver. *Int. J. Radiat. Oncol. Biol. Phys.*, 70(5):1571–1578, Apr 2008.

A. Jemal, F. Bray, M. M. Center, J. Ferlay, E. Ward, and D. Forman. Global cancer statistics. *CA Cancer J Clin*, 61(2):69–90, 2011.

S. B. Jiang, C. Pope, K. M. Al Jarrah, J. H. Kung, T. Bortfeld, and G. T. Chen. An experimental investigation on intra-fractional organ motion effects in lung IMRT treatments. *Phys Med Biol*, 48(12):1773–1784, Jun 2003.

Jian-Yue Jin and Fang-Fang Yin. Time delay measurement for linac based treatment delivery in synchronized respiratory gating radiotherapy. *Medical Physics*, 32(5): 1293–1296, 2005.

M. Joiner and A. van der Kogel. *Basic Clinical Radiobiology Fourth Edition*. Hodder Education, 4 edition, 2009. ISBN 1444166689, 9781444166682.

H. Kang, E. D. Yorke, J. Yang, C. S. Chui, K. E. Rosenzweig, and H. I. Amols. Evaluation of tumor motion effects on dose distribution for hypofractionated intensity-modulated radiotherapy of non-small-cell lung cancer. *J Appl Clin Med Phys*, 11 (3):3182, 2010.

P. J. Keall, V. R. Kini, S. S. Vedam, and R. Mohan. Motion adaptive x-ray therapy: a feasibility study. *Phys Med Biol*, 46(1):1–10, Jan 2001.

P. J. Keall, S. Joshi, S. S. Vedam, J. V. Siebers, V. R. Kini, and R. Mohan. Four-dimensional radiotherapy planning for DMLC-based respiratory motion tracking. *Med Phys*, 32(4):942–951, Apr 2005.

P. J. Keall, G. S. Mageras, J. M. Balter, R. S. Emery, K. M. Forster, S. B. Jiang, J. M. Kapatoes, D. A. Low, M. J. Murphy, B. R. Murray, C. R. Ramsey, M. B. Van Herk, S. S. Vedam, J. W. Wong, and E. Yorke. The management of respiratory motion in radiation oncology report of AAPM Task Group 76. *Med Phys*, 33(10): 3874–3900, Oct 2006.

F. M. Khan. *The Physics of Radiation Therapy.* Lippincott Williams & Wilkins, 2010. ISBN 0781788560, 9780781788564.

K. Kitamura, H. Shirato, Y. Seppenwoolde, T. Shimizu, Y. Kodama, H. Endo, R. Onimaru, M. Oda, K. Fujita, S. Shimizu, and K. Miyasaka. Tumor location, cirrhosis, and surgical history contribute to tumor movement in the liver, as measured during stereotactic irradiation using a real-time tumor-tracking radiotherapy system. *Int. J. Radiat. Oncol. Biol. Phys.*, 56(1):221–228, May 2003.

E. E. Klein, J. Hanley, J. Bayouth, F. F. Yin, W. Simon, S. Dresser, C. Serago, F. Aguirre, L. Ma, B. Arjomandy, C. Liu, C. Sandin, and T. Holmes. Task Group 142 report: quality assurance of medical accelerators. *Med Phys*, 36(9):4197–4212, Sep 2009.

G. Kragl, S. af Wetterstedt, B. Knausl, M. Lind, P. McCavana, T. Knoos, B. McClean, and D. Georg. Dosimetric characteristics of 6 and 10MV unflattened photon beams. *Radiother Oncol*, 93(1):141–146, Oct 2009.

D. Latty, K. E. Stuart, W. Wang, and V. Ahern. Review of deep inspiration breath-hold techniques for the treatment of breast cancer. *J Med Radiat Sci*, 62(1):74–81, Mar 2015.

R. Li, E. Mok, B. Han, A. Koong, and L. Xing. Evaluation of the geometric accuracy of surrogate-based gated VMAT using intrafraction kilovoltage x-ray images. *Med Phys*, 39(5):2686–2693, May 2012.

X. Li, Y. Yang, T. Li, K. Fallon, D. E. Heron, and M. S. Huq. Dosimetric effect of respiratory motion on volumetric-modulated arc therapy-based lung SBRT treatment delivered by TrueBeam machine with flattening filter-free beam. *J Appl Clin Med Phys*, 14(6):4370, 2013.

C. C. Ling, C. Burman, C. S. Chui, G. J. Kutcher, S. A. Leibel, T. LoSasso, R. Mohan, T. Bortfeld, L. Reinstein, S. Spirou, X. H. Wang, Q. Wu, M. Zelefsky, and Z. Fuks.

Conformal radiation treatment of prostate cancer using inversely-planned intensity-modulated photon beams produced with dynamic multileaf collimation. *Int. J. Radiat. Oncol. Biol. Phys.*, 35(4):721–730, Jul 1996.

W. A. Mampuya, M. Nakamura, Y. Matsuo, N. Ueki, Y. Iizuka, T. Fujimoto, S. Yano, H. Monzen, T. Mizowaki, and M. Hiraoka. Interfraction variation in lung tumor position with abdominal compression during stereotactic body radiotherapy. *Med Phys*, 40(9):091718, Sep 2013.

T. P. Mate, D. Krag, J. N. Wright, and Dimmer S. A new system to perform continuous target tracking for radiation and surgery using non-ionizing alternating current electromagnetics. *International Congress Series*, 1268:425 – 430, 2004.

S. L. Meeks, J. M. Buatti, L. G. Bouchet, F. J. Bova, T. C. Ryken, E. C. Pennington, K. M. Anderson, and W. A. Friedman. Ultrasound-guided extracranial radiosurgery: technique and application. *Int. J. Radiat. Oncol. Biol. Phys.*, 55(4): 1092–1101, Mar 2003.

Ante Mestrovic, Alan Nichol, Brenda G Clark, and Karl Otto. Integration of on-line imaging, plan adaptation and radiation delivery: proof of concept using digital tomosynthesis. *Physics in Medicine and Biology*, 54(12):3803, 2009. URL `http://stacks.iop.org/0031-9155/54/i=12/a=013`.

M. J. Murphy. Tracking moving organs in real time. *Semin Radiat Oncol*, 14(1): 91–100, Jan 2004.

Y. Nagata, K. Takayama, Y. Matsuo, Y. Norihisa, T. Mizowaki, T. Sakamoto, M. Sakamoto, M. Mitsumori, K. Shibuya, N. Araki, S. Yano, and M. Hiraoka. Clinical outcomes of a phase I/II study of 48 Gy of stereotactic body radiotherapy in 4 fractions for primary lung cancer using a stereotactic body frame. *Int. J. Radiat. Oncol. Biol. Phys.*, 63(5):1427–1431, Dec 2005.

T. Neicu, H. Shirato, Y. Seppenwoolde, and S. B. Jiang. Synchronized moving aperture radiation therapy (SMART): average tumour trajectory for lung patients. *Phys Med Biol*, 48(5):587–598, Mar 2003.

G. Nicolini, S. Ghosh-Laskar, S. K. Shrivastava, S. Banerjee, S. Chaudhary, J. P. Agarwal, A. Munshi, A. Clivio, A. Fogliata, P. Mancosu, E. Vanetti, and L. Cozzi. Volumetric modulation arc radiotherapy with flattening filter-free beams compared with static gantry IMRT and 3D conformal radiotherapy for advanced esophageal cancer: a feasibility study. *Int. J. Radiat. Oncol. Biol. Phys.*, 84(2):553–560, Oct 2012.

Giorgia Nicolini, Eugenio Vanetti, Alessandro Clivio, Antonella Fogliata, and Luca Cozzi. Pre-clinical evaluation of respiratory-gated delivery of volumetric modulated arc therapy with rapidarc. *Physics in Medicine and Biology*, 55(12):N347, 2010. URL `http://stacks.iop.org/0031-9155/55/i=12/a=N01`.

K. Ohara, T. Okumura, M. Akisada, T. Inada, T. Mori, H. Yokota, and M. J. Calaguas. Irradiation synchronized with respiration gate. *Int. J. Radiat. Oncol. Biol. Phys.*, 17(4):853–857, Oct 1989.

K. Otto. Volumetric modulated arc therapy: IMRT in a single gantry arc. *Medical Physics*, 35(1):310–317, 2008.

L. Papiez, D. Rangaraj, and P. Keall. Real-time DMLC IMRT delivery for mobile and deforming targets. *Med Phys*, 32(9):3037–3048, Sep 2005.

Jianguo Qian, Lei Xing, Wu Liu, and Gary Luxton. Dose verification for respiratory-gated volumetric modulated arc therapy. *Physics in Medicine and Biology*, 56(15): 4827, 2011. URL `http://stacks.iop.org/0031-9155/56/i=15/a=013`.

N. Rochet, J. I. Drake, K. Harrington, J. A. Wolfgang, B. Napolitano, B. T. Sadek, M. N. Shenouda, A. R. Keruakous, A. Niemierko, and A. G. Taghian. Deep inspiration breath-hold technique in left-sided breast cancer radiation therapy: Evaluating cardiac contact distance as a predictor of cardiac exposure for patient selection. *Pract Radiat Oncol*, 5(3):e127–134, 2015.

K. E. Rusthoven, B. D. Kavanagh, S. H. Burri, C. Chen, H. Cardenes, M. A. Chidel, T. J. Pugh, M. Kane, L. E. Gaspar, and T. E. Schefter. Multi-institutional phase I/II trial of stereotactic body radiation therapy for lung metastases. *J. Clin. Oncol.*, 27(10):1579–1584, Apr 2009.

A. Schweikard, G. Glosser, M. Bodduluri, M. J. Murphy, and J. R. Adler. Robotic motion compensation for respiratory movement during radiosurgery. *Comput. Aided Surg.*, 5(4):263–277, 2000.

M. Scorsetti, F. Alongi, S. Castiglioni, A. Clivio, A. Fogliata, F. Lobefalo, P. Mancosu, P. Navarria, V. Palumbo, C. Pellegrini, S. Pentimalli, G. Reggiori, A. M. Ascolese, A. Roggio, S. Arcangeli, A. Tozzi, E. Vanetti, and L. Cozzi. Feasibility and early clinical assessment of flattening filter free (FFF) based stereotactic body radiotherapy (SBRT) treatments. *Radiat Oncol*, 6:113, 2011.

P. G. Seiler, H. Blattmann, S. Kirsch, R. K. Muench, and C. Schilling. A novel tracking technique for the continuous precise measurement of tumour positions in conformal radiotherapy. *Phys Med Biol*, 45(9):N103–110, Sep 2000.

H. Shirato, S. Shimizu, K. Kitamura, T. Nishioka, K. Kagei, S. Hashimoto, H. Aoyama, T. Kunieda, N. Shinohara, H. Dosaka-Akita, and K. Miyasaka. Four-dimensional treatment planning and fluoroscopic real-time tumor tracking radiotherapy for moving tumor. *Int. J. Radiat. Oncol. Biol. Phys.*, 48(2):435–442, Sep 2000.

R. L. Smith, K. Lechleiter, K. Malinowski, D. M. Shepard, D. J. Housley, M. Afghan, J. Newell, J. Petersen, B. Sargent, and P. Parikh. Evaluation of linear accelerator gating with real-time electromagnetic tracking. *Int. J. Radiat. Oncol. Biol. Phys.*, 74(3):920–927, Jul 2009.

Wendy Smith and Nathan Becker. Time delays in gated radiotherapy. *Journal of Applied Clinical Medical Physics*, 10(3), 2009.

I. Suramo, M. Paivansalo, and V. Myllyla. Cranio-caudal movements of the liver, pancreas and kidneys in respiration. *Acta Radiol Diagn (Stockh)*, 25(2):129–131, 1984.

S. E. Tenn, T. D. Solberg, and P. M. Medin. Targeting accuracy of an image guided gating system for stereotactic body radiotherapy. *Phys Med Biol*, 50(23):5443–5462, Dec 2005.

R. D. Timmerman, C. Park, and B. D. Kavanagh. The North American experience with stereotactic body radiation therapy in non-small cell lung cancer. *J Thorac Oncol*, 2(7 Suppl 3):S101–112, Jul 2007.

J. S. Tobias. The role of radiotherapy in the management of cancer–an overview. *Ann. Acad. Med. Singap.*, 25(3):371–379, May 1996.

O. N. Vassiliev, S. F. Kry, J. Y. Chang, P. A. Balter, U. Titt, and R. Mohan. Stereotactic radiotherapy for lung cancer using a flattening filter free Clinac. *J Appl Clin Med Phys*, 10(1):2880, 2009.

S. S. Vedam, P. J. Keall, V. R. Kini, and R. Mohan. Determining parameters for respiration-gated radiotherapy. *Med Phys*, 28(10):2139–2146, Oct 2001.

F. Viel, R. Lee, E. Gete, and C. Duzenli. Amplitude gating for a coached breathing approach in respiratory gated 10 MV flattening filter-free VMAT delivery. *J Appl Clin Med Phys*, 16(4):5350, 2015.

R. Wagman, E. Yorke, E. Ford, P. Giraud, G. Mageras, B. Minsky, and K. Rosenzweig. Respiratory gating for liver tumors: use in dose escalation. *Int. J. Radiat. Oncol. Biol. Phys.*, 55(3):659–668, Mar 2003.

P. H. Weiss, J. M. Baker, and E. J. Potchen. Assessment of hepatic respiratory excursion. *J. Nucl. Med.*, 13(10):758–759, Oct 1972.

J. W. Wong, M. B. Sharpe, D. A. Jaffray, V. R. Kini, J. M. Robertson, J. S. Stromberg, and A. A. Martinez. The use of active breathing control (ABC) to reduce margin for breathing motion. *Int. J. Radiat. Oncol. Biol. Phys.*, 44(4): 911–919, Jul 1999.

J. Yang, J. Cai, H. Wang, Z. Chang, B. G. Czito, M. R. Bashir, M. Palta, and F. F. Yin. Is diaphragm motion a good surrogate for liver tumor motion? *Int. J. Radiat. Oncol. Biol. Phys.*, 90(4):952–958, Nov 2014.